

E-ISSN 2980-3012

Physics and Astronomy Reports

VOLUME 1 • NUMBER 2 • DECEMBER 2023



İSTANBUL
UNIVERSITY
PRESS

Indexing and Abstracting

NASA/ADS



OWNER

Prof. Dr. Tansel AK

Istanbul University, Faculty of Science, Istanbul, Turkiye

RESPONSIBLE MANAGER

Prof. Dr. Elif AKALIN

Istanbul University, Faculty of Science,
Department of Physics, Istanbul, Turkiye

CORRESPONDENCE ADDRESS

Istanbul University Faculty of Science
PK 34134 Vezneciler, Fatih, Istanbul, Turkiye

Phone : +90 (212) 455 57 00

Fax : +90 (212) 512 21 40

E-mail: par@istanbul.edu.tr

<https://iupress.istanbul.edu.tr/en/journal/par/home>

<https://dergipark.org.tr/en/pub/par>

PUBLISHER

Istanbul University Press

Istanbul University Central Campus,
34452 Beyazit, Fatih, Istanbul, Turkiye

Phone: +90 (212) 440 00 00

Authors bear responsibility for the content of their published articles.

The publication language of the journal is English.

This is a scholarly, international, peer-reviewed and open-access journal published biannually in June and December.

Publication Type: Periodical

EDITORIAL MANAGEMENT BOARD

EDITOR-IN-CHIEF

Prof. Dr. Elif AKALIN – Istanbul University, Faculty of Science, Department of Physics, Istanbul, Türkiye – eakalin@istanbul.edu.tr

CO-EDITOR

Prof. Dr. Selçuk BİLİR – Istanbul University, Faculty of Science, Department of Astronomy and Space Sciences, Istanbul, Türkiye – sbilir@istanbul.edu.tr

STATISTICS EDITOR

Dr. Hikmet ÇAKMAK – Istanbul University, Faculty of Science, Department of Astronomy and Space Sciences, Istanbul, Türkiye – hcakmak@istanbul.edu.tr

PUBLICITY MANAGER

Assit. Prof. Dr. Talar YONTAN – Istanbul University, Faculty of Science, Department of Astronomy and Space Sciences, Istanbul, Türkiye – talar.yontan@istanbul.edu.tr

ETHICS EDITOR

Prof. Dr. İpek KANAT ÖZTÜRK – Istanbul University, Faculty of Science, Department of Physics, Istanbul, Türkiye – ikanat@istanbul.edu.tr

EDITORIAL ASSISTANT

Assit. Prof. Dr. Özgecan ÖNAL TAŞ – Istanbul University, Faculty of Science, Department of Astronomy and Space Sciences, Istanbul, Türkiye – ozgecan.onal@istanbul.edu.tr

LANGUAGE EDITORS

Elizabeth Mary EARL – Istanbul University, Istanbul, Türkiye – elizabeth.earl@istanbul.edu.tr

EDITORIAL BOARD

Volkan BAKIŞ – Akdeniz University, Antalya, Türkiye – volkanbakis@akdeniz.edu.tr

Timothy BANKS – Harper College, Chicago, United-States – tim.banks@nielsen.com

Gönül BAŞAR – Istanbul University, Istanbul, Türkiye – gbasar@istanbul.edu.tr

Helene CARRERE – University of Toulouse, Toulouse, France – carrere@insa-toulouse.fr

Ömür ÇAKIRLI – Ege University, Izmir, Türkiye – omur.cakirli@ege.edu.tr

Uğur ÇEVİK – Karadeniz Teknik University, Trabzon, Türkiye – ugurc@ktu.edu.tr

Ahmet DERVİŞOĞLU – Ataturk University, Erzurum, Türkiye – ahmet.dervisoglu@atauni.edu.tr

Goran DJORDJEVIC – University of Nis, Nis, Serbia – gorandj@junis.ni.ac.rs

Yavuz EKŞİ – Istanbul University, Istanbul, Türkiye – eksi@itu.edu.tr

Ayşe EROL – Akdeniz University, Antalya, Türkiye – ayseerol@istanbul.edu.tr

Muhsin HARAKEH – University of Groningen, Groningen, Netherlands – m.n.harakeh@rug.nl

Mohamed HENINI – University of Nottingham, Nottingham, United-Kingdom – Mohamed.Henini@nottingham.ac.uk

Ümit KAVAK – NASA Ames Research Center, Moffett-Field, United-States – ukavak@sofia.usra.edu

Mükremin KILIÇ – University of Oklahoma, Oklahoma, United-States – kilic@ou.edu

Sophie KRÖGER – Hochschule für Technik und Wirtschaft Berlin, Berlin, Germany – sophie.kroeger@hte-berlin.de

Yeşim ÖKTEM – Istanbul University, Istanbul, Türkiye – yesim.oktem@istanbul.edu.tr

Faruk SOYDUGAN – Canakkale Onsekiz Mart University, Canakkale, Türkiye – fsoydugan@comu.edu.tr

Horst STOECKER – Goethe University, Frankfurt, Germany – stoecker@fias.uni-frankfurt.de

Timur ŞAHİN – Akdeniz University, Antalya, Türkiye – timursahin@akdeniz.edu.tr

Hakan Volkan ŞENAVCI – Ankara University, Ankara, Türkiye – hvsenavci@ankara.edu.tr

Kadri YAKUT – Ege University, Izmir, Türkiye – kadri.yakut@ege.edu.tr

Özgür YAVUZÇETİN – University of Wisconsin-Whitewater, Whitewater, United-States – yavuzce@uww.edu

CONTENTS

RESEARCH ARTICLES

- 44** A New Approach to Calculate Coronal Electron Density: Simplified Van De Hulst's Method
Hikmet ÇAKMAK
- 54** An Updated Line List for Spectroscopic Investigation of G Stars- I: Redetermination of the Abundances in the Solar Photosphere
Timur ŞAHİN, Mahmut MARIŞMAK, Nur ÇINAR, Selçuk BİLİR
- 65** Comprehensive Analysis of the Open Cluster Collinder 74
Talar YONTAN, Remziye CANBAY
- 74** A Theoretical Study: DNA Binding and ADMET Profile of Some Hydroxycinnamic Acids
Bilge BIÇAK, Serda KECEL GÜNDÜZ
- 85** Verification of the Existence of Recently Published New Energy Levels of Atomic Holmium
Doğukan BİNGÖL, Gönül BAŞAR, Günay Başar, İpek Kanat ÖZTÜRK, Feyza GÜZELÇİMEN, Seda Kın BARKA, Sophie KRÖGER
- 93** Investigating Single Quantum Anharmonic Oscillator with Perturbation Theory
Büşra ADALI, Ferhat NUTKU

A New Approach to Calculate Coronal Electron Density: Simplified Van De Hulst's Method

H. Çakmak^{1*} 

¹Istanbul University, Faculty of Science, Department of Astronomy and Space Sciences, 34116, Beyazıt, Istanbul, Türkiye

ABSTRACT

Determining the electron density is a challenging task in solar corona studies, as it requires certain assumptions to be made, such as symmetric, homogeneous and radial distribution, thermal equilibrium, etc. In such studies, the observed K corona brightness is based on the coronal electron density. An important paper on the calculation of electron density was published in 1950 by van de Hulst in an article titled “The Electron Density of the Solar Corona”. The author developed a method with some assumptions to calculate the electron density from the observed K corona brightness. We presented here, a new simplified calculation method for the coronal electron density is presented. The integral equation solution given by van de Hulst is interpreted from a different perspective and the K coronal electron density is calculated using only observational data without making any additional adjustments such as successive approximations and multiple attempts.

Keywords: Sun: corona; scattering; polarization; Astrometry and celestial mechanics: eclipses

1. INTRODUCTION

Theoretical studies on the solar corona began with a published article by Schuster (1879). This work investigated the brightness and polarisation of the solar corona with regards to various particle distributions within the corona. The majority of the fundamental mathematical issues were resolved with the explanations provided here. According to this, the corona light is the composite of all the light scattered by the free electrons in the line of sight direction. The polarisation of the corona light results from this phenomenon. Minnaert (1930) further developed Schuster's theory by taking into account the limb darkening effect of the observed solar disc. Additionally, the equations for the relation between electron density and brightness were provided. Baumbach (1937, 1938) introduced the first general formula for the electron density of the solar corona from photometric observations as a function of the solar radius;

$$N(r) = 10^8 \left(\frac{0.036}{r^{1.5}} + \frac{1.55}{r^6} + \frac{2.99}{r^{16}} \right) \quad (1)$$

where N is the electron density in cm^3 , and r is the distance from the solar disc expressed in solar radius. Subsequently, corona light intensity was analysed by Allen (1946) and van de Hulst (1950) according to the minimum and maximum phases of the solar cycle. They provided two distinct corona models. The type of corona during cycle maximum exhibits nearly spherical brightness distribution, and most coronal structures show a symmetric arrangement across the solar disc (see Figure 1, right

panel). In contrast, the type of corona during cycle minimum exhibits a concentration of coronal structures in the equatorial and polar regions (Figure 1, left panel) and features with asymmetric brightness distribution. Furthermore, Saito et al. (1970) developed an empirical function of the electron density which also depends on the heliographic latitude as follows;

$$N_e(r, \phi) = \frac{3.09 \times 10^8}{r^{16}} (1 - 0.5 \sin \phi) + \frac{1.58 \times 10^8}{r^6} (1 - 0.95 \sin \phi) + \frac{0.0251 \times 10^8}{r^{2.5}} (1 - 1.0 \sin^{0.5} \phi) \quad (2)$$

where N_e is the electron density in cm^3 and ϕ is the heliographic latitude. The equation allows us to compute the electron density asymmetrically across the solar disc. It is thus possible to use this equation to represent changes in coronal brightness based on corona type during solar minimum or maximum by adjusting the $\sin \phi$ coefficients (see Appendix B for details).

A dataset of corona brightness from eclipse observations is typically necessary to develop the formulas presented above. In order to achieve the most accurate results, intricate computations and various approaches are necessary. For instance, the outcomes of the method, which are outlined in the following section, were obtained through successive approximations and extensive trials, each time improving the computations slightly. Similarly, another approach, which incorporates van de Hulst's

Corresponding Author: H. Çakmak **E-mail:** hcakmak@istanbul.edu.tr

Submitted: 01.06.2023 • **Revision Requested:** 19.06.2023 • **Last Revision Received:** 28.10.2023 • **Accepted:** 06.11.2023



This article is licensed under a Creative Commons Attribution-NonCommercial 4.0 International License (CC BY-NC 4.0)

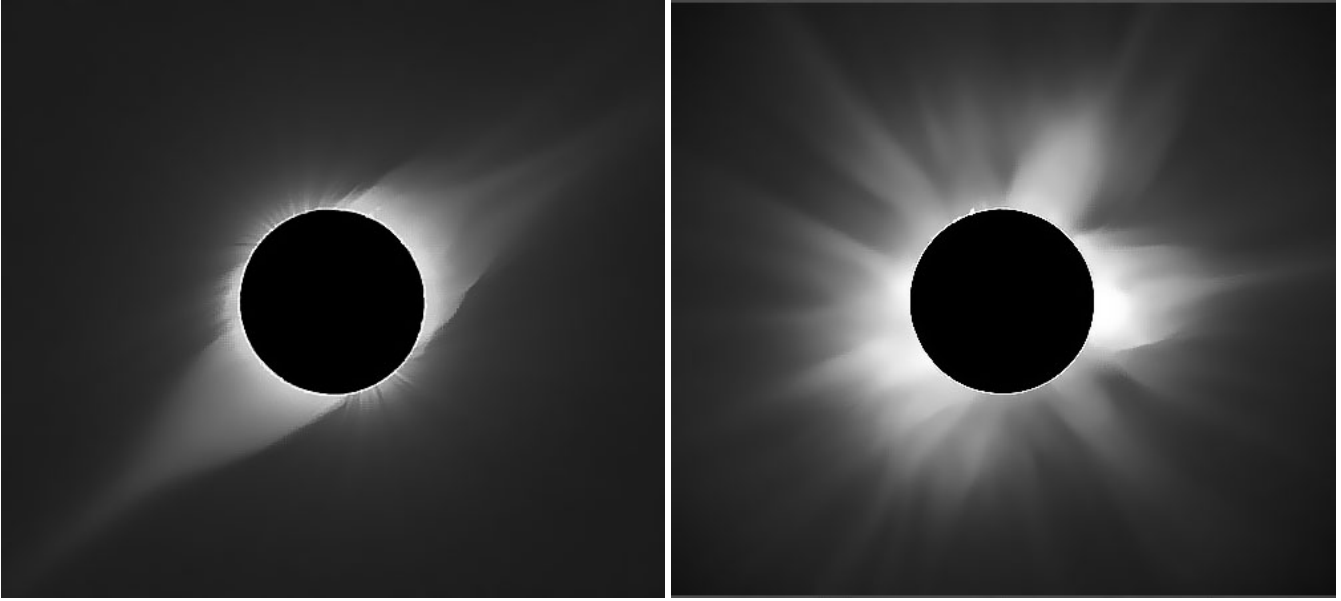


Figure 1. Appearance of the solar corona according to solar cycle phase. *Left:* minimum phase (on 4 October 1995), *Right:* maximum phase (on 21 June 2001).

model, was devised by [von Klüber \(1958\)](#). This article derives the K corona luminance and the corona electron density through the assumption that the polarization arises from K corona light and that F corona light is unpolarized. Consequently, the subsequent equation was formulated as

$$K P_K = P_{K+F}(K + F) = K_t - K_r \quad (3)$$

where $K + F$ represents the total corona brightness. P_K and P_{K+F} refer to the degree of polarisation of the K corona and the total corona, respectively. Furthermore, K_t and K_r represent the tangential and radial components of the K corona brightness, respectively. Similar complex computations, as in Van de Hulst's method, were carried out during this study. First, the electron density of the corona was determined for the $K_t - K_r$ component. Subsequently, the K_t component was calculated through a reverse calculation of Van de Hulst's equation. Using these values of the $K_t - K_r$ and K_t components, the observational corona brightness K was obtained (for detailed information, refer to article [von Klüber 1958](#)).

The new approach presented here has simpler steps compared to the methods mentioned above. The electron density of the corona is computed without time-consuming calculations, using only the luminosity K and the degree of polarization of the corona. As an approximation for the calculations, two new electron densities N_{t-r} and N_t are defined for the components $K_t - K_r$ and K_t , respectively.

Nowadays, as a result of the developing technological possibilities, different methods have been developed to calculate coronal electron densities ([Bemporad 2020](#); [Del Zanna et al. 2023](#)). However, these methods are quite different from the method described here, in terms of both observation type and electron density calculation technique. In addition, due to the lack of numerical results on the electron density for the equa-

torial and polar regions in these studies, it was not possible to make a comparison with the results given here.

The van de Hulst approach to determining electron density is concisely outlined in Section 2. A full explanation of about new approximation is given in Section 3. Subsequently, Section 4 presents the validation of the new method utilizing model values from Table 5A in van de Hulst's article. In Section 5, an instance of the new method's application is showcased, featuring the numerical values acquired during the full solar eclipse on the 29th of March, 2006. The Discussion section concludes the article by detailing the benefits and advantages of the novel methodology.

2. VAN DE HULST'S METHOD FOR CALCULATING THE ELECTRON DENSITY

The content of this section is a brief overview of the author's original article, providing only a basic outline of the method. For more comprehensive information, it is advisable to refer to [van de Hulst \(1950\)](#). Most of the explanations given here, such as formulae and figures, are also necessary for a better understanding of the new approach presented in the following section.

The observed brightness of the corona is assumed to be the light scattered by the free electrons ([Schuster 1879](#); [Baumbach 1937](#)). Therefore, this brightness should be directly proportional to the density of electrons in the corona. In order to visualise this scenario, consider a single ray of light hitting a vibrating electron (at point P) and reflecting in the direction of the observer (Figure 2). Here, r and x represent the actual distance and projected distance of the light from the centre of the disc, respectively, whilst θ denotes the angle separating the

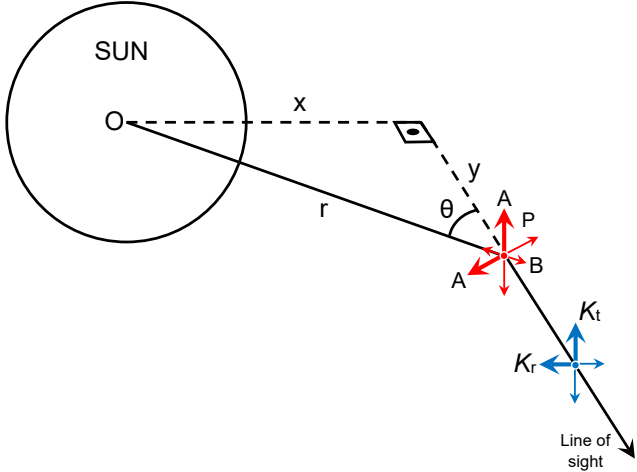


Figure 2. Geometrical representation of both the scattered light incident on a vibrating electron and its intensity components (reconstructed from van de Hulst 1950).

incoming light direction and the line of sight. Applying the formula presented by van de Hulst (1950), the total intensity of the light scattered per second per unit solid angle by a column with a cross-section of 1 cm^2 is determined using

$$K(x) = C \int_x^\infty N(r) \left\{ \left(2 - \frac{x^2}{r^2} \right) A(r) + \frac{x^2}{r^2} B(r) \right\} \frac{r dr}{\sqrt{r^2 - x^2}} \quad (4)$$

the equations below are expressed in terms of the tangential and radial components of this reflected light,

$$K_t(x) = C \int_x^\infty N(r) A(r) \frac{r dr}{\sqrt{r^2 - x^2}} \quad (5)$$

$$K_t(x) - K_r(x) = C \int_x^\infty N(r) \left\{ A(r) - B(r) \right\} \frac{x^2 dr}{r \sqrt{r^2 - x^2}}$$

where A and B represent the lengths of semi-major and semi-minor axis of the vibration ellipsoid, respectively. The constant C is equal to $3/4 R_\odot \sigma = 3.44 \times 10^{-14} \text{ cm}^3$, where R_\odot ($= 6.96 \times 10^{10} \text{ cm}$) represents the solar radius, and σ ($= 0.66 \times 10^{-24} \text{ cm}^2$) is the electron scattering cross-section. The primary issue here is to divide the known $K(x)$ intensity into two parts $K_t(x)$ and $K_r(x)$, and solve the integrals in such a way that both equations produce the same electron density $N(r)$. van de Hulst originally defined the coronal brightness components $K_t(r)$ and $K_t(r) - K_r(r)$ through the use of coronal intensity $K(x)$ and its model polarization degree $p(x)$ as

$$K_t(x) = 1/2[1 + p(x)]K(x) \quad (6)$$

$$K_t(x) - K_r(x) = p(x)K(x) \quad (7)$$

This can also be expressed as a power series in the form of

$$K_t(x) = \sum_s h_s x^{-s} \quad (8)$$

$$K_t(x) - K_r(x) = \sum_s k_s x^{-s} \quad (9)$$

where $\sum_s h_s x^{-s}$ represents with three elements, namely $A x^{-a} + B x^{-b} + C x^{-c}$. van de Hulst then made another approach and assumed that the solution of integrals given in Equation 5 was of the following form;

$$r C N(r) A(r) = \sum_s \frac{h_s}{a_{s-1}} r^{-s} = K_t(r) \quad (10)$$

$$r C N(r) \{A(r) - B(r)\} = \sum_s \frac{k_s}{a_{s+1}} r^{-s} = K_t(r) - K_r(r) \quad (11)$$

where

$$a_s = \int_0^{\pi/2} \sin^n \theta d\theta = \frac{\pi}{2^{n+1}} \frac{n!}{\{(n/2)!\}^2} \quad (12)$$

The electron densities can now be calculated from Equations 10 and 11. Firstly, the coefficients h_s , k_s and s of Equations 8 and 9 are obtained by making polynomial fit to the calculated values of Equations 6 and 7 separately. Then, the right-hand sides of Equations 10 and 11 are calculated respectively by using a new polynomial function formed with these coefficients. r , C , $A(r)$ and $B(r)$ are precomputable values in this approach (refer to van de Hulst (1950)'s article for calculation of these values). At this point, the calculated electron densities $N(r)$ in both Equations 10 and 11 must show the same value. If not, a method of successive approximations is used, replacing both $K_t(r)$ and $K_t(r) - K_r(r)$ by a reduction as small as

$$K_t(r) = \{1 + \epsilon p\} K_t' \quad (13)$$

$$K_t(r) - K_r(r) = \{1 + \epsilon(1 + p)\} (K_t' - K_r') \quad (14)$$

where ϵ is a value not exceeding ± 0.05 . K_t' and $K_t' - K_r'$ are pre-computed values of $K_t(r)$ and $K_t(r) - K_r(r)$. These computations are repeated, altering ϵ in each iteration, until both $K_t(r)$ and $K_t(r) - K_r(r)$ show the same electron density in Equations 10 and 11. Although van de Hulst has achieved satisfactory results for the electron densities of the model corona using this methodology, its practical application is rather challenging and requires multiple attempts of unspecified numbers.

3. NEW APPROACH FOR CORONAL ELECTRON DENSITY

The values of $K_t(x)$ and $K_t(x) - K_r(x)$ computed in Equations 6 and 7 are numerically different from each other. Thus, this difference should also be valid for Equations 10 and 11. Therefore, the electron density $N(r)$ in each equation must be different as

well. At this point, as a novel approach, the value of $N(r)$ in each equation is given a different nomenclature, defined as

$$N_t(r) = \frac{1}{rC} \frac{K_t(r)}{A(r)} \quad (15)$$

$$N_{t-r}(r) = \frac{1}{rC} \frac{K_t(r) - K_r(r)}{A(r) - B(r)} \quad (16)$$

where $N_t(r)$ represents the electron density for $K_t(r)$ and $N_{t-r}(r)$ represents $K_t(r) - K_r(r)$. On the other hand, by eliminating the $p(x)K(x)$ values in Equations 6 and 7, the corona intensity $K(x)$ can be expressed in terms of $K_t(x)$ and $K_t(x) - K_r(x)$ as

$$K_t + K_r = K = 2K_t - (K_t - K_r) \quad (17)$$

Considering Equation 4 or Equations 10 and 11, the corona intensity $K(r)$ is linearly proportional to the electron density $N(r)$. Therefore, any valid conclusion drawn between the components of the $K(r)$ corona (Equation 17) can also be drawn between the components of the electron density (Equations 15 and 16). Accordingly, the electron density N can be expressed in a similar manner as

$$N = 2N_t - N_{t-r} \quad (18)$$

With this newly derived equation, it is now possible to calculate the electron density for a known $K(x)$ intensity using only the values of the $K_t(r)$ and $K_t(r) - K_r(r)$ components.

4. VALIDATING THE NEW APPROACH

The newly developed method was tested using the K corona brightness and the polarization degree values of the van de Hulst model as an observational corona values. The model corona values such as $K_t + K_r$, K_t and $K_t - K_r$ are taken from Table 5A in van de Hulst (1950)'s article. First, the polynomial coefficients h_s , k_s and s in Equations 8 and 9 were obtained by fitting a separate curve to the brightness values K_t and $K_t - K_r$. Then, new polynomial functions are created using these new coefficients produced by h_s/a_{s-1} and k_s/a_{s+1} (shown in Equation 10 and 11). These new functions are referred to as "generated functions" (GFs), and are represented as

$$f(K_t - K_r) = \sum_s \frac{k_s}{a_{s+1}} r^{-s} \quad \text{and} \quad f(K_t) = \sum_s \frac{h_s}{a_{s-1}} r^{-s} \quad (19)$$

After calculating the electron densities N_t and N_{t-r} for the brightnesses K_t and $K_t - K_r$ using Equations 15 and 16, the total electron density is determined by combining these values with Equation 18. The results obtained for the equatorial region of van de Hulst model are shown in Table 1. The K corona brightness values of the minimum type model are shown on the left side of the table. Also, the coefficients (A, B, C, a, b and c) of the fitted function for each component are listed under its column at the left-bottom side. For the fitting process, a three-element polynomial is employed, given by $(A r^{-a} + B r^{-b} + C r^{-c})$. Furthermore, values for a_{s+1} and a_{s-1} , calculated

using Equation 12 with a , b and c coefficients, are listed at bottom of the left side. The computed values of GFs $f(K_t)$ and $f(K_t - K_r)$ are presented in the first two columns of the right side of Table 1 and the coefficients utilized to construct these functions are listed underneath these values. The calculated electron densities N_t and N_{t-r} , and the total electron density N are exhibited in their corresponding columns on the right side of Table 1.

The electron density calculations were repeated for the polar region of the van de Hulst model, resulting in the same level of agreement. Table 3 presents the electron density values attained by the new method for both the equatorial and polar regions of the minimum type corona, alongside the values obtained by van de Hulst (1950). From the table, it can be seen that the new method's values match closely with those of the van de Hulst model for both the equatorial and polar regions. A similar comparison was made using the K corona values and polarization degree values of the Allen (1973). The same agreement was also achieved for these values. The computed values of the new method for Allen (1973) values are shown in Table 2 and Table 4, respectively.

5. CALCULATED ELECTRON DENSITIES OF THE 2006 SOLAR ECLIPSE

The newly developed method was utilized to compute the electron density of the solar corona as observed during the total eclipse on March 29, 2006, in Türkiye. This eclipse observation was carried out with the 8-inch Meade telescope by the staff of the Astronomy and Space Sciences Department of Istanbul University in the Manavgat district of Antalya. During the eclipse event, observations of white light polarization were conducted, and eclipse photographs were taken at three different polarization angles, 0° , 60° , and 120° . A total of 15 photos were taken during totality with an interval of $3^m 30^s$ between $11^h 55^m 10^s$ and $11^h 58^m 40^s$ UT. Five different exposure times were used in these shoots; $1/2$, $1/4$, $1/30$, $1/60$, and $1/125$ second. In addition, images of the solar disc were taken at different diaphragm openings before the eclipse for brightness calibration and exposure times used here were the same as those used during the eclipse. After performing brightness calibration and computation of Stokes parameters using polarization images, the total corona brightness ($K + F$) and polarization degree (P_{K+F}) of the 2006 eclipse obtained by considering the sky with instrumental contribution and active chromospheric regions (see Appendix A for details). The isophote plots of total corona brightness and its polarization degree are shown separately in Figure 3. The numbers on the isophote lines are in units of $10^{-9} I_\odot$ for the total brightness, and in percent for the polarization degree. The values obtained for both parameters at specific distances from the solar disc are given in Table 5.

The K corona brightness values are obtained by subtracting F corona model values of van de Hulst (1950) from the observed

Table 1. Calculation results for the equatorial region of the minimum-type corona of [van de Hulst \(1950\)](#) computed using the new approach. Brightness is in units of $10^{-8}I_{\odot}$, and electron density is in units of 10^6 cm^{-3} .

r	K	P_K	$K_t - K_r$	K_t	$f(K_t - K_r)$	$f(K_t)$	N_{t-r}	N_t	N
1.0	300.40	0.18	54.40	177.40	104.03	470.10	239.66	226.68	213.7
1.03	202.80	0.24	48.00	125.40	111.69	328.27	171.88	176.05	180.2
1.06	141.30	0.28	39.10	90.20	94.66	230.57	128.04	130.48	132.9
1.1	91.10	0.32	29.30	60.20	70.99	148.07	87.24	88.68	90.1
1.2	37.10	0.41	15.14	26.12	35.53	58.50	39.40	39.18	38.9
1.3	18.50	0.46	8.56	13.53	19.72	28.63	21.28	21.02	20.8
1.5	6.20	0.54	3.34	4.77	7.46	9.69	8.24	8.29	8.3
1.7	2.57	0.59	1.51	2.04	3.33	4.06	3.90	3.96	4.0
2.0	0.85	0.62	0.53	0.69	1.19	1.35	1.55	1.55	1.5
2.6	0.16	0.66	0.11	0.13	0.23	0.23	0.37	0.34	0.3
3.0	0.07	0.65	0.05	0.06	0.09	0.09	0.17	0.15	0.1
4.0	0.02	0.61	0.01	0.02	0.02	0.01	0.04	0.03	0.02
			k_s	h_s	k_s/a_{s+1}	h_s/a_{s-1}			
		A	40.50	71.98	90.03	143.68			
		B	26.66	121.28	83.22	398.10			
		C	-12.77	-15.86	-69.22	-71.68			
		a	6.25	6.74	6.25	6.74			
		b	13.80	17.42	13.80	17.42			
		c	44.63	32.58	44.63	32.58			
			a_{s+1}	a_{s-1}					
		for a	0.4499	0.5010					
		for b	0.3203	0.3046					
		for c	0.1845	0.2213					

Table 2. Calculation results for the equatorial region of the minimum-type corona of [Allen \(1973\)](#) computed using the new approach. Brightness is in units of $10^{-8}I_{\odot}$, and electron density is in units of 10^6 cm^{-3} .

r	K	P_K	$K_t - K_r$	K_t	$f(K_t - K_r)$	$f(K_t)$	N_{t-r}	N_t	N
1.01	269.15	0.22	58.41	163.78	175.31	532.27	317.89	271.40	224.9
1.03	199.53	0.23	46.09	122.81	115.52	333.43	177.77	178.82	179.9
1.06	144.54	0.25	36.28	90.41	86.75	226.47	117.34	128.16	139.0
1.1	102.33	0.28	28.24	65.29	65.84	157.67	80.91	94.43	107.9
1.2	44.67	0.33	14.74	29.70	35.16	71.74	39.00	48.05	57.1
1.4	12.02	0.40	4.85	8.43	11.59	18.79	12.55	14.95	17.3
1.6	4.68	0.42	1.97	3.33	4.43	6.43	5.03	5.89	6.7
1.8	2.00	0.39	0.77	1.38	1.90	2.77	2.30	2.86	3.4
2.0	1.00	0.34	0.34	0.67	0.89	1.43	1.16	1.64	2.1
2.2	0.60	0.30	0.18	0.39	0.45	0.85	0.62	1.07	1.5
2.5	0.27	0.26	0.07	0.17	0.18	0.46	0.28	0.66	1.0
3.0	0.10	0.20	0.02	0.06	0.05	0.21	0.09	0.37	0.7
4.0	0.03	0.13	0.004	0.02	0.01	0.07	0.01	0.17	0.3

$K + F$ total brightness values. This process has been carried out with the assumption that F corona does not change much from one solar cycle to another ([Kulijanishvili & Kapanadze 2005](#); [Morgan & Habbal 2007](#)). Also, the polarization degree P_K of the K corona is determined using the equation of [von Klüber \(1958\)](#), which is given by

$$P_K = P_{K+F} \left(\frac{K + F}{K} \right). \quad (20)$$

For this eclipse, the electron densities in the equatorial and polar regions were calculated using the K corona brightness and its polarization degree. The obtained results are shown in

Table 6A for the equatorial region and Table 6B for the polar region. The calculated electron densities of the equatorial (black circle) and polar (black triangle) regions are shown in Figure 4 in comparison with the observational values of [Newkirk \(1967\)](#) and [Allen \(1973\)](#) and model electron density values of [van de Hulst \(1950\)](#) and [Saito et al. \(1970\)](#). It is clear from the figure that the electron density values observed in the 2006 eclipse are in good agreement with comparison values given. Any discrepancies between the observed and model values may be due to the asymmetric brightness distribution caused by the asymmetric distribution of the solar material. This is clearly

illustrated in Figure 3a, where the equatorial and polar intensity distributions are compared.

Table 3. Comparison of electron densities obtained using the new method with those from the van de Hulst (1950) values. Electron density is in units of 10^6 cm^{-3} .

r	van de Hulst N		This study N	
	Equator	Polar	Equator	Polar
1.0	227.0	174.0	213.7	170.3
1.03	178.0	127.0	180.2	127.0
1.06	132.0	87.2	132.9	86.9
1.1	90.0	53.2	90.1	52.9
1.2	39.8	16.3	39.0	15.8
1.3	21.2	5.98	20.8	5.8
1.5	8.3	1.4	8.3	1.5
1.7	4.0	0.542	4.0	0.620
2.0	1.580	0.196	1.544	0.199
2.6	0.374	0.040	0.317	0.030
3.0	0.176	0.017	0.131	0.010
4.0	0.050	0.004	0.021	0.001

Table 4. Comparison of electron densities obtained using the new method with those from the Allen (1973) values. Electron density is in units of 10^6 cm^{-3} .

r	Allen N		This study N	
	Equator	Polar	Equator	Polar
1.01	251.2	199.5	224.9	215.4
1.03	177.8	131.8	179.9	150.1
1.06	125.9	95.5	139.0	87.7
1.1	91.2	64.6	107.9	57.6
1.2	46.8	19.9	57.1	26.2
1.4	15.1	4.4	17.3	3.4
1.6	6.8	1.3	6.7	0.5
1.8	3.6	0.6	3.4	0.1
2.0	2.0	0.3	2.1	0.06
2.2	1.3	0.2	1.5	0.04
2.5	0.6	0.1	1.0	0.02
3.0	0.3	0.05	0.7	0.01
4.0	0.1	0.02	0.3	0.001

Table 5. Observed total corona brightness $K + F$ and polarization degree P_{K+F} values of 29 March 2006 eclipse.

r	$K + F$ corona ($\times 10^{-9} I_{\odot}$)		P_{K+F} (%)	
	Equa.	Polar	Equa.	Polar
1.10	1311	648	19.0	32.4
1.15	1046	364	26.7	36.3
1.20	782	201	36.4	33.2
1.25	513	128	44.7	25.9
1.30	293	90	46.1	19.6
1.35	180	70	39.8	15.0
1.40	125	57	32.4	13.9
1.45	94	48	26.8	12.3
1.50	74	42	22.5	11.6
1.55	61	38	19.4	10.7
1.60	52	–	17.1	–
1.65	45	–	15.8	–
1.70	40	–	14.6	–

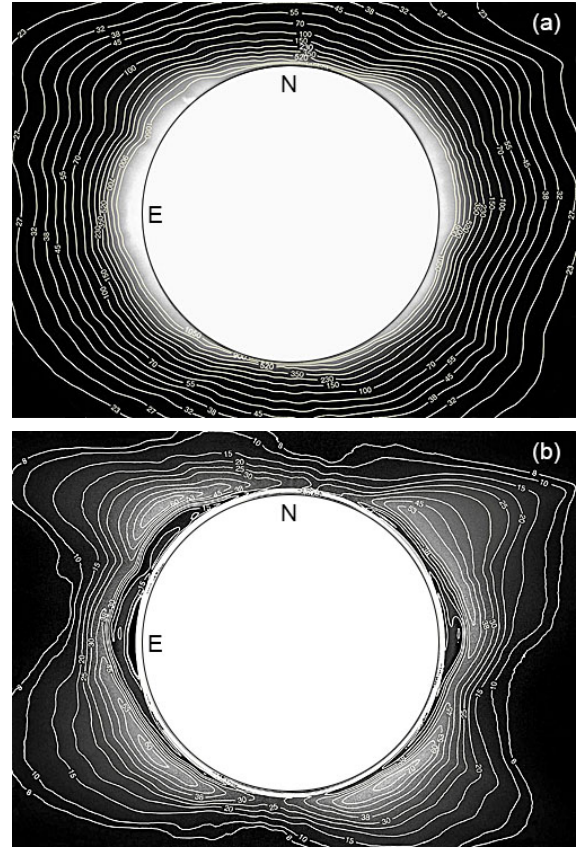


Figure 3. (a) Isophotes of total corona brightness (values are in units of $10^{-9} I_{\odot}$) and (b) isolines of polarization degree (values are in percent) of the 29 March 2006 solar eclipse.

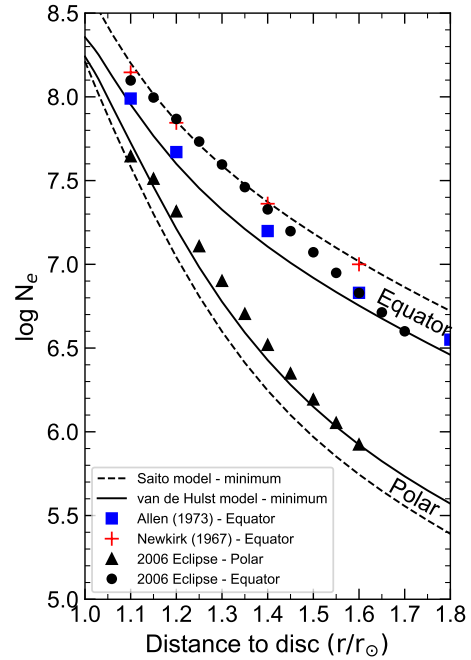


Figure 4. Comparison of electron densities in the equatorial and polar regions during the solar eclipse on 29 March 2006 with selected observational data and model values of van de Hulst (1950) and Saito et al. (1970)

Table 6. Values used for electron density calculation (left side), and results from Eclipse 2006 (right side). K values are in units of $10^{-9}I_{\odot}$, and P is in percent.

A – equatorial region										
r	K	P_K	$K_t - K_r$	K_t	$f(K_t - K_r)$	$f(K_t)$	N_{t-r}	N_t	N_{equ}	
1.10	158.6	0.196	31.1	94.8	160.5	269.3	197.2	161.3	125.4	
1.15	96.6	0.285	27.5	62.0	103.4	171.5	118.9	109.0	99.0	
1.20	72.6	0.403	28.9	50.2	68.0	111.4	75.4	74.6	73.9	
1.25	46.0	0.517	23.8	34.9	45.5	73.7	49.5	51.8	54.1	
1.30	24.9	0.558	13.9	19.4	30.9	49.6	33.4	36.4	39.5	
1.35	14.4	0.506	7.3	10.8	21.3	33.9	23.0	26.0	28.9	
1.40	9.4	0.433	4.1	6.7	14.9	23.6	16.2	18.7	21.3	
1.45	6.6	0.376	2.5	4.6	10.6	16.6	11.6	13.7	15.8	
1.50	5.0	0.330	1.6	3.3	7.6	11.8	8.4	10.1	11.8	
1.55	3.9	0.298	1.2	2.6	5.5	8.5	6.2	7.5	8.9	
1.60	3.2	0.274	0.9	2.1	4.0	6.2	4.6	5.7	6.8	
1.65	2.4	0.263	0.6	1.5	3.0	4.6	3.5	4.3	5.2	
1.70	1.9	0.249	0.5	1.2	2.2	3.4	2.6	3.3	4.0	

B – polar region										
r	K	P_K	$K_t - K_r$	K_t	$f(K_t - K_r)$	$f(K_t)$	N_{t-r}	N_t	N_{pol}	
1.10	54.8	0.395	21.6	38.2	76.5	115.4	94.0	69.1	44.2	
1.15	28.5	0.425	12.1	20.3	36.0	58.0	41.4	36.9	32.4	
1.20	13.7	0.382	5.2	9.4	18.3	30.6	20.3	20.5	20.7	
1.25	7.6	0.316	2.4	5.0	10.0	16.9	10.9	11.9	12.8	
1.30	4.7	0.275	1.3	3.0	5.9	9.8	6.4	7.2	8.0	
1.35	3.3	0.252	0.8	2.1	3.7	5.9	4.0	4.5	5.1	
1.40	2.5	0.240	0.6	1.6	2.4	3.7	2.6	3.0	3.3	
1.45	2.1	0.258	0.5	1.3	1.7	2.5	1.8	2.0	2.2	
1.50	1.0	0.287	0.3	0.7	1.2	1.7	1.3	1.4	1.6	
1.55	0.5	0.266	0.1	0.3	0.9	1.2	1.0	1.0	1.1	
1.60	0.3	0.264	0.1	0.2	0.6	0.9	0.7	0.8	0.8	

6. DISCUSSION

The main challenge of the newly developed method is to determine the optimal coefficients (h_s, k_s, s) of the power function in transition from Equations 8–9 to Equations 10–11. This involves a demanding phase of performing numerous fitting curve tests to determine the appropriate coefficients of the three- or two-element power function. Using these coefficients, the observational values of $K_t(x)$ and $K_t(x) - K_r(x)$, which depend on the projection distance, are converted into the values of $K_t(r)$ and $K_t(r) - K_r(r)$, which depend on the true distance.

During the fitting process, it is crucial to ensure that the fitted curve passes through the overall distribution of the observation points. Attempting to fit the curve close to every observation point is generally ineffective (see Figure 5a) due to inevitable observational errors that cause scattering in the values. Thus, a solution should be devised for the general trend of these observation points (see Figure 5b). There are two possible techniques to accomplish this task. The first option involves fitting a two-element power function curve to the values of a curve obtained by fitting a polynomial equation with one element or six or more elements. The second option involves fitting a power function curve with restricted parameters where each coefficient has a boundary between specified values (refer to Figure

5c). The second method, which is preferred in this study, provides a straightforward and fulfilling solution without requiring additional experimentation. However, it can be challenging to adjust the limits for limiting coefficients in a consistent manner across different eclipse data. Nevertheless, this is a common occurrence, as each eclipse typically has a unique distribution with its own distinct characteristics. Once the coefficients for the power function are determined for the observational values, generating GFs and obtaining the electron density become straightforward steps in this method.

When examining the test results of the electron density for [van de Hulst \(1950\)](#) obtained by the newly introduced method shown in Table 3, it is evident that the compared values are in very good agreement. This fact is more apparent in Figure 6a, which confirms the accuracy level of the new method. The similar agreement is also seen for the values of [Allen \(1973\)](#) given in Tables 2 and 4, respectively. As highlighted in Figure 6, the electron density values of both the model and the novel method are mainly distributed along the line. When checked for compatibility in individual regions, the coefficient of determination R^2 is 0.9974 for the equatorial region and 0.9996 for the polar region of [van de Hulst \(1950\)](#), while 0.9845 for

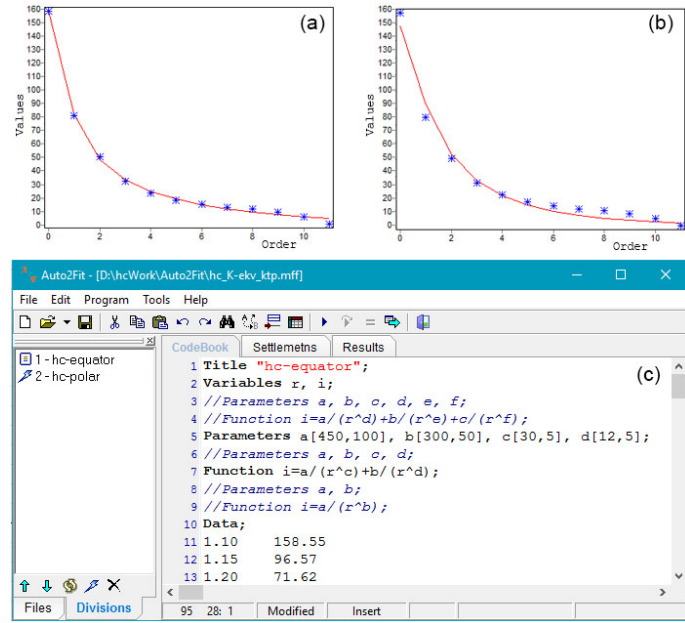


Figure 5. (a) Power function curve fitted without any constraints, (b) power function curve fitted with delimited coefficients, (c) screenshot of a program showing parameters utilized to fit the power function curve under different configurations.

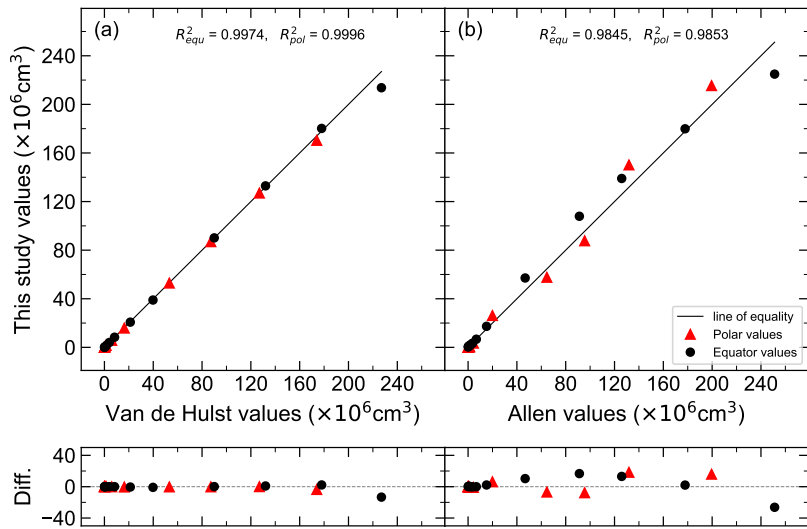


Figure 6. Comparison of electron density values from (a) van de Hulst’s model and (b) Allen’s values with those derived from this study. The plots below illustrate the numerical disparity between these two approaches.

the equatorial region and 0.9853 for the polar region of Allen (1973).

Although the results from Eclipse 2006 are quite satisfactory, It would be better to retest this new method with the data from other eclipse observations, especially with the other eclipse results from other researchers who have their own observational electron density data. Thus, the accuracy of the new method will be confirmed by finding similar or conclusive results for these data. For example, when the new method was tested with van de Hulst model values in Section 4, satisfactory electron density results were obtained. Thus, the probability of finding similar consistent results with other observational data is quite high.

This should be examined, particularly by other researchers who have measured electron densities using their methods. In order to check the new approach with different observational values, it is intended to contact more than one researcher investigating this topic in the future.

Peer Review: Externally peer-reviewed.

Conflict of Interest: Author declared no conflict of interest.

Financial Disclosure: This work was supported by the Istanbul University Scientific Research Projects Commission with project numbers 24242 and 470/27122005.

Acknowledgements: Thanks to especially every staff who took part in the 2006 solar eclipse observation. Thanks also to the

anonymous referees for their valuable suggestions and comments that improved the manuscript.

Note: The Statistics Editor was not involved in the evaluation, peer-review and decision processes of the article. These processes were carried out by the Editor-in-Chief and the member editors of the editorial management board.

LIST OF AUTHOR ORCIDS

H. Çakmak <https://orcid.org/0000-0002-1959-6049>

REFERENCES

- Allen C. W., 1946, *MNRAS*, **106**, 137
 Allen C., 1973, *Astrophysical Quantities* 3rd ed.. Athlone Press, London
 Baumbach S., 1937, *Astronomische Nachrichten*, **263**, 121
 Baumbach S., 1938, *Astronomische Nachrichten*, **267**, 273
 Bemporad A., 2020, *ApJ*, **904**, 178
 Çakmak H., 2017, *Sol. Phys.*, **292**, 186
 Del Zanna G., et al., 2023, *ApJS*, **265**, 11
 Kulijanishvili V. I., Kapanadze N. G., 2005, *Sol. Phys.*, **229**, 45
 Minnaert M., 1930, *Z. Astrophys.*, **1**, 209
 Morgan H., Habbal S. R., 2007, *A&A*, **471**, L47
 Newkirk Gordon J., 1967, *ARA&A*, **5**, 213
 Saito K., Makita M., Nishi K., Hata S., 1970, *Annals of the Tokyo Astronomical Observatory*, **12**, 51
 Schuster A., 1879, *MNRAS*, **40**, 35
 von Klüber H., 1958, *MNRAS*, **118**, 201
 van de Hulst H. C., 1950, *Bull. Astron. Inst. Netherlands*, **11**, 135

APPENDIX A: CALCULATION PROCEDURES OF THE K CORONA BRIGHTNESS

First of all, as a reminder, all procedures relevant to this section are given comprehensively in Çakmak (2017)'s article. Please review this article for more information. A very brief summary of the general steps of this procedure is given verbally here. In order to determine the brightness of the K corona, a brightness calibration must first be performed. This requires taking images at different diaphragm openings with the same exposure times as used for polarized images. Once the intensity calibration function (defined in Çakmak 2017) has been obtained by using these solar disc images, the brightness of the corona in all polarized images is calculated by normalizing their intensity. Then, the average corona brightness values are determined for the polar region between latitudes 0° – 30° and for the equatorial region between latitudes 40° – 90° , separately (Figure A1).

At this stage, regions with chromospheric structure were excluded from the calculation, taking into account their distance range from the Sun's surface, to avoid erroneous increases in brightness.

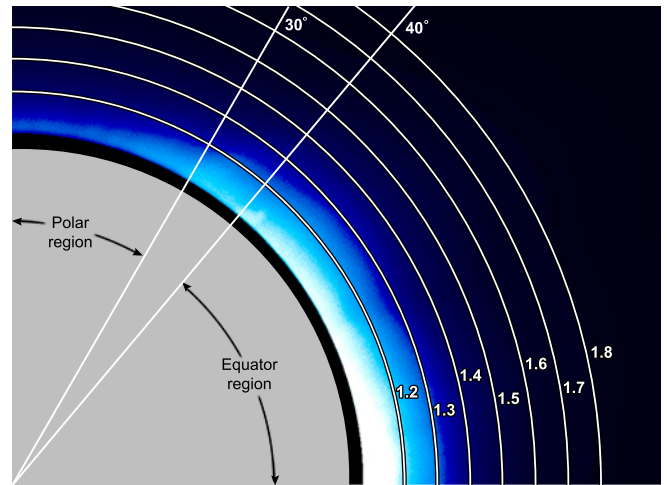


Figure A1. The latitude ranges for the polar and equatorial regions used in a single quadrant. Distances to the solar disc are given in units of solar radius.

APPENDIX B: EXPLANATIONS ABOUT LATITUDE-DEPENDENT CORONAL BRIGHTNESS CALCULATION

A very brief summary of the explanations on this subject from the article of Saito et al. (1970) is given here. Please refer to that article for more information. To describe the brightness of an arbitrary point in the solar corona, the graphical situation shown in Figure B1 is considered. In this figure, P is the point in question, P' is the projection of P on the celestial plane, ϕ is the heliographic latitude of P , ϕ_0 is the projected angle of on the celestial plane, θ is angle OPP' and z is the line-of-sight length.

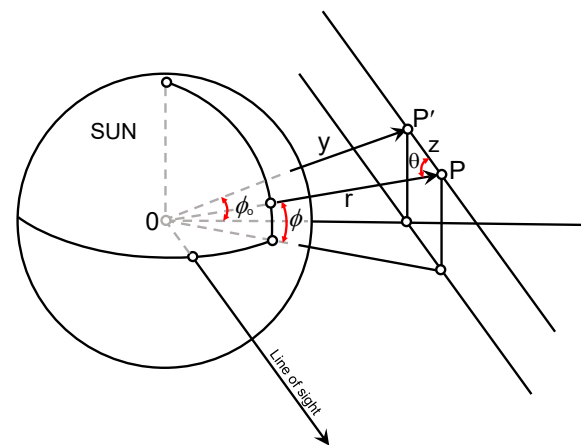


Figure B1. Latitude-dependent diagram of an arbitrary point in the solar corona (reconstructed from Saito et al. 1970).

In that paper, the author obtained the following equations from Equation 5

$$I_t - I_r = C 2y \int_0^{\pi/2} N(r, \phi)(A - B)d\theta \quad (\text{B1})$$

$$I_t = C 2y \int_0^{\pi/2} N(r, \phi)(A) \frac{d\theta}{\sin^2 \theta}$$

under certain assumptions with

$$\sin \phi = \sin \phi_0 \sin \theta, \quad r \sin \theta = y$$

$$N = \frac{N_0}{R^n} = N_0 k^n \sin^n \theta, \quad N(r, \phi) = \sum N_{0,i} \frac{1 - f_i \sin^{s_i} \phi}{r^{n_i}}$$

where k is the modulus of the integrals and a number between 0 and 1, n is a real number, f_i and s_i are positive real number. As a result of arranging the Equation B1, the following formula is obtained for latitude-dependent K corona brightness.

$$(I_t \pm I_r)_{\phi_0} = (I_t \pm I_r)_{\text{equ}} - \frac{\sin \phi_0}{k} 0.5 \times 5.365 \times 10^{-6} (I_t \pm I_r)_{17}$$

$$+ \frac{\sin \phi_0}{k} 0.95 \times 2.752 \times 10^{-6} (I_t \pm I_r)_7$$

$$+ \frac{\sin^{0.5} \phi_0}{k^{0.5}} 1.0 \times 0.0436 \times 10^{-6} (I_t \pm I_r)_3 \quad (\text{B2})$$

This equation can be expressed as

$$N_e(r, \phi) = \frac{3.09 \times 10^8}{r^{16}} (1 - 0.5 \sin \phi)$$

$$+ \frac{1.58 \times 10^8}{r^6} (1 - 0.95 \sin \phi) \quad (\text{B3})$$

$$+ \frac{0.0251 \times 10^8}{r^{2.5}} (1 - 1.0 \sin^{0.5} \phi)$$

Using this last equation, the coronal electron density can be visualized as shown Figure B2. As can be seen from Equation B3, different profiles for the coronal electron density can be produced by changing the coefficients of $\sin \phi$'s shown in red.

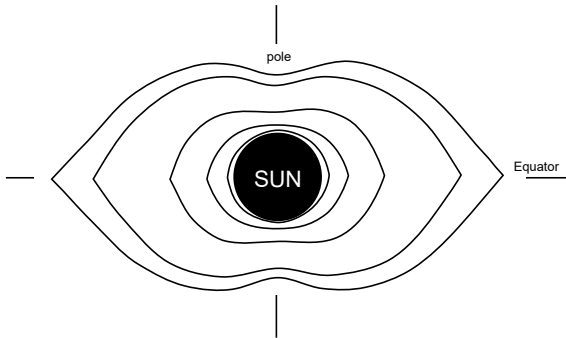


Figure B2. Iso-density curves of electrons in the K corona computed with the Equation B3 (reconstructed from Saito et al. 1970).

An Updated Line List for Spectroscopic Investigation of G Stars- I: Redetermination of the Abundances in the Solar Photosphere

T. Şahin^{1*} , M. Marişmak¹ , N. Çınar¹ , and S. Bilir² 

¹ Akdeniz University, Faculty of Science, Department of Space Sciences and Technologies, 07058, Antalya, Türkiye

² Istanbul University, Faculty of Science, Department of Astronomy and Space Sciences, 34119, Beyazıt, Istanbul, Türkiye

ABSTRACT

We propose a line list that may be useful for the abundance analysis of G-type stars in the wavelength range 4080 – 6780 Å. It is expected that the line list will be useful for surveys/libraries with overlapping spectral regions (e.g. ELODIE/SOPHIE libraries, UVES-580 setting of *Gaia*-ESO), and in particular for the analysis of F- and G-type stars in general. The atomic data are supplemented by detailed references to the sources. We estimated the Solar abundances using stellar lines and the high-resolution Kitt Peak National Observatory (KPNO) spectra of the Sun to determine the uncertainty in the $\log gf$ values. By undertaking a systematic search that makes use of the lower excitation potential and gf -values and using revised multiplet table as an initial guide, we identified 363 lines of 24 species that have accurate gf -values and are free of blends in the spectra of the Sun and a Solar analogue star, HD 218209 (G6V), for which accurate and up-to-date abundances were obtained from both ELODIE and POLARBASE spectra of the star. For the common lines with the *Gaia*-ESO line list v.6 provided by the *Gaia*-ESO collaboration, we discovered significant inconsistencies in the gf -values for certain lines of varying species.

Keywords: Line: identification; Sun: abundances; Sun: fundamental parameters; Stars: individual (HD 218209)

1. INTRODUCTION

Mid-spectral type main-sequence stars (F and G-type stars) play a significant role in understanding the Galactic chemical evolution and history of Galactic structure. These stars formed in the early Milky Way or are currently forming, have main-sequence lifetimes comparable to the age of the Galaxy. F and G-type main-sequence stars have an internal structure consisting of a radiative core surrounded by a large envelope. Such structural configuration prevents heavy elements produced in the core from mixing into the stellar atmosphere. Consequently, mid-spectral type stars carry the chemical composition of the molecular cloud in which they were born. The study of the abundances of heavy elements detected in the atmospheres of F and G-type stars provides valuable insights into the Galactic chemical evolution and the history of Galactic structure, as noted by [Pagel & Patchett \(1975\)](#).

Moreover, these stars offer crucial information about the formation of different populations within the Galaxy, including the halo, thick disc, and thin disc. By analyzing the kinematics and orbital dynamics of stars that have been spectroscopically studied, one can distinguish between these different population groups in the Milky Way. In addition to providing insights into Galactic chemical evolution and the formation of the Galaxy, considering the case for pure spectroscopic analysis, for in-

stance, the α -element abundances determined through spectroscopic analysis of stars play a crucial role in testing the population membership of host galaxies.

The abundance of elements in a stellar spectrum, such as metallicity ($[Fe/H]$), can also be used to estimate the age of the star. This is because the youngest stars have relatively higher metal abundances and metallicity compared to the oldest stars ([Placco et al. 2021](#)). Therefore, pure spectroscopic analysis alone provides crucial information about the nature of host galaxies, in addition to insights into the age and chemical composition of individual stars.

The kinematics, orbital dynamics, and chemical properties of stars are not only the key in understanding the chemical structure of our Galaxy and its accompanying formation scenarios but also in determining the origins of (metal-poor) young and old G-spectral type stars. In this context, the author's research team is currently engaged in a thorough investigation encompassing more than 90 G-type metal-poor stars residing within the Solar neighbourhood. This study aims to investigate the origins of these stars by analyzing their kinematics, orbital dynamics, and chemical properties. This research will shed light on the formation processes and evolutionary pathways of metal-poor G spectral-type stars in our Galaxy.

Furthermore, the author's group has previously conducted a

Corresponding Author: Timur Şahin E-mail: timursahin@akdeniz.edu.tr

Submitted: 16.08.2023 • Revision Requested: 15.09.2023 • Last Revision Received: 10.10.2023 • Accepted: 13.10.2023



This article is licensed under a Creative Commons Attribution-NonCommercial 4.0 International License (CC BY-NC 4.0)

thorough investigation of six metal-poor F-type dwarf stars in the Solar neighbourhood, with $[\text{Fe}/\text{H}]$ values ranging from -2.4 to -1 dex. It is worth noting that the studied metal-poor F-type dwarf stars exhibited significant changes in model atmosphere parameters (effective temperature, T_{eff} ; surface gravity, $\log g$; metallicity, $[\text{Fe}/\text{H}]$; microturbulence, ξ), as reported in the literature. This research, as published in Şahin & Bilir (2020), employed state-of-the-art analysis methods, including classical spectroscopy with the help of ELODIE spectra. By combining these analysis techniques, the authors were able to determine the Galactic origin of these F-type dwarf stars in the Solar neighbourhood.

The determination of accurate metal abundances depends on the accurate determination of model parameters. Current spectroscopic sky survey programs for metal-poor late spectral stars, for example, indicate the need to determine precisely calibrated model parameters for them. These current sky survey programs include *Gaia*-ESO Public Spectroscopic Survey (GES; Gilmore et al. 2012), GALactic Archaeology with HERMES (GALAH; Heijmans et al. 2012; De Silva et al. 2015; Martell et al. 2017), the Large Sky Area Multi-Object Fiber Spectroscopic Telescope (LAMOST; Zhao et al. 2012), the Sloan Extension for Galactic Understanding and Exploration (SEGUE; Yanny et al. 2009), the Apache Point Observatory Galactic Evolution Experiment (APOGEE; Allende Prieto et al. 2008), and the Radial Velocity Experiment (RAVE; Steinmetz et al. 2006), and demonstrate that precisely determined and calibrated model atmosphere parameters are required in different regions of the electromagnetic spectrum due to differences in adopted observational methods and techniques in these surveys, for which reliable line lists and atomic data are required.

In this study, we present an up-to-date line list for planned spectral analyses in the framework of the comprehensive study mentioned above. HD 218209 of G6V, the most metal-rich star among 90 G spectral-type program stars ($-2.5 < [\text{Fe}/\text{H}] (\text{dex}) < -0.5$), was selected for the preparation of the line list which is expected to be useful for the surveys/libraries with overlapping spectral regions (e.g. ELODIE library; Subirana et al. 2003) and for the analysis of F and G-type stars in general.

This paper is organized as follows. Section 2 provides information concerning the observations. Section 3 explains the procedures used to measure and identify lines, as well as the techniques employed to determine the model parameters and conduct chemical abundance analyses of both HD 218209 and the Sun. Section 4 is dedicated to discussing findings and their potential implications.

2. OBSERVATIONS

For the creation of the line list in this study, high resolution ($R \approx 42\,000$) and high signal to noise ($S/N = 165$ at 550 nm) ELODIE spectrum (HJD 2451184.23521; $R \approx 42\,000$; expo-

sure time 1800 s) of HD 218209 was selected. The ELODIE cross-dispersed echelle spectrograph provided spectral coverage from 3900 to 6800 Å. The spectrum was continuum normalized and wavelength calibrated, and the radial velocity (RV) was corrected by the data reduction pipeline at the telescope. Since some problems were encountered in the continuum normalization of the spectra from the library, the spectrum was renormalized.

Since high resolution ($R \approx 76\,000$) and high signal to noise ($S/N = 140$ at 550 nm) POLARBASE¹ (Petit et al. 2014) Narval² spectrum (HJD 2456232.48238; exposure time 400 s) of the star was also available, it was used to test model parameters for the star. Prior to the line measurement process, the POLARBASE spectrum was also renormalized and corrected for the radial velocity (RV). For RV correction, we used a Python interface and the NARVAL atomic line library containing atomic transitions from 4000 to 6800 Å. For renormalization, we used an in-house developed interactive normalization code LIME (Şahin 2017) in Interactive Data Language (IDL) prior to the abundance analysis.

The Solar spectrum is certainly a primary reference for stellar astrophysics and for interpreting physical processes in stars (Molaro & Monai 2012). The high-resolution ($R \approx 400\,000$) spectrum of the Sun used in this study was obtained with the Kitt Peak Fourier Transform Spectrometer (FTS; Kurucz et al. 1984). The character of the spectra of HD 218209 and the Sun is displayed in Figure 1.

3. THE ABUNDANCE ANALYSIS

We employed ATLAS9 model atmospheres (Castelli & Kurucz 2003) computed in local thermodynamic equilibrium (LTE) with NEWODF opacities for the abundance study of HD 218209 and the Solar spectrum. Elemental abundances were computed by using the LTE line analysis code MOOG (Snedden 1973)³. The details of the abundance analysis and the source of the atomic data are the same as in Şahin & Lambert (2009), Şahin et al. (2011, 2016) and Şahin & Bilir (2020). The line list, atomic data, and model parameter derivation are covered in the following subsections.

3.1. Line List: Line Measurement, Identification and Atomic Data

An essential prerequisite for abundance analysis of a star is a set of identified lines with reliable atomic data. Our line lists were created by a systematic search for unblended lines (useful for equivalent width–EW– analysis technique). For line measurement from the ELODIE spectrum of HD 218209, a systematic

¹ <http://polarbase.irap.omp.eu>

² Narval spectropolarimeter is adapted to the 2m Bernard Lyot telescope and provides high-resolution spectral and polarimetric data.

³ The MOOG source code is available at <http://www.as.utexas.edu/chris/moog.html>

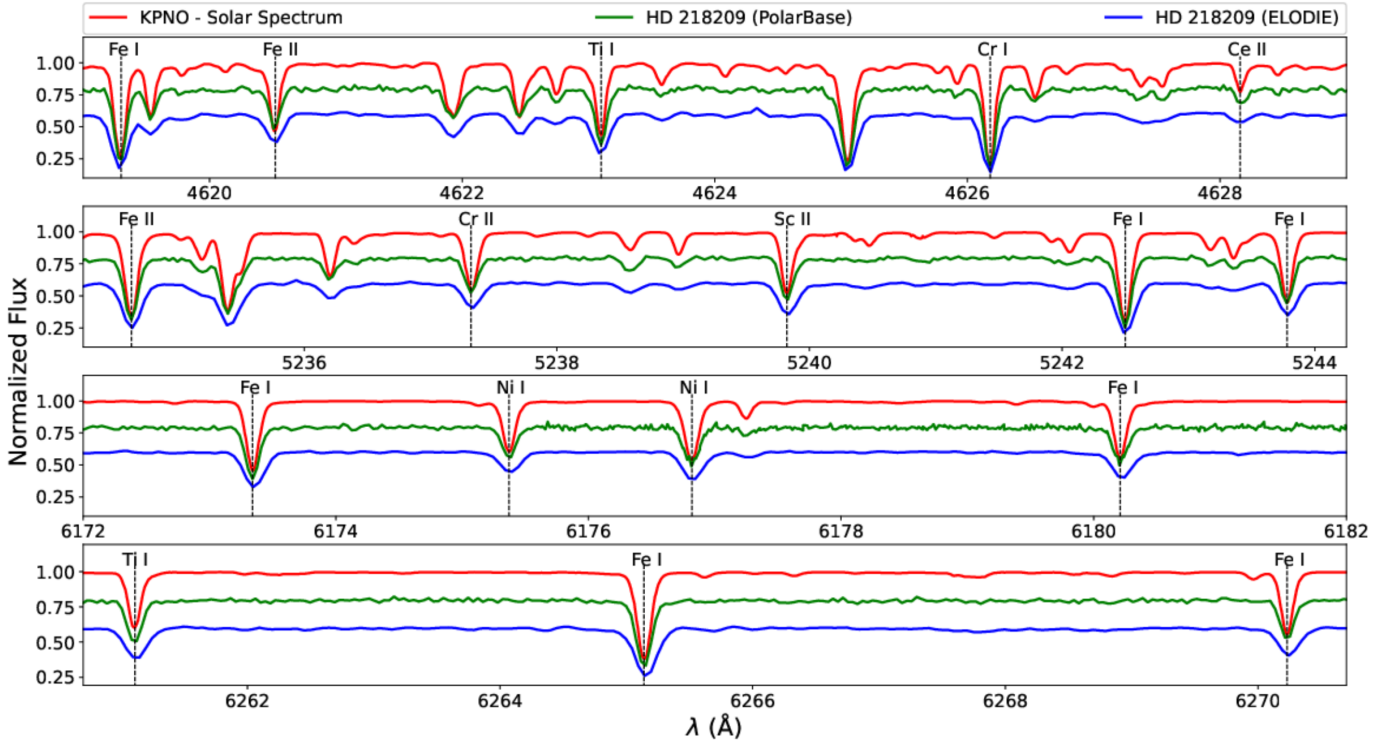


Figure 1. A small region of the KPNO, POLARBASE, and ELODIE spectra of HD 218209 and the Sun. Identified lines are also indicated.

search for unblended lines was performed. The line centre positions were measured in several segments, each containing a portion of the spectra of 20 Å. For this, the LIME (Şahin 2017) code was employed. The code provides a list of possible transitions in the close neighbourhood of the measured line together with recent atomic data (e.g. Rowland Multiplet Number-RMT, $\log gf$, and lower Level Excitation Potential-LEP) that are compiled from the literature (e.g. from NIST database). The MOORE catalogue (Moore et al. 1966) was configured as one of the reference atomic line libraries in the LIME code. Following the line identification step, a multiplet analysis technique was performed to assess whether the detected lines belong to the candidate element indicated by the code. Our final list covers 24 species and 363 lines over the spectrum range from about 4100 – 6800 Å. The identified lines have accurate gf -values and are free of blends in the spectra of the Sun and HD 218209. The number of identified lines in the respective wavelength regions of the KPNO Solar spectrum is presented in Figure 2. Our selection of iron lines included 132 Fe I lines with excitation potentials (LEPs) ranging from 0.05 to ≈ 5 eV and 17 Fe II lines. Chosen lines of Fe I and Fe II are exhibited in Table 1. In Table 2, we provide the list of identified lines other than iron with the atomic data, their measured equivalent widths (obtained using the LIME code) and computed logarithmic abundances in the Solar spectrum and in the spectrum of HD 218209.

3.2. Model Parameters and Abundances

We used neutral and ionised Fe lines to determine model atmospheric parameters such as effective temperature, surface gravity, microturbulence, and metallicity (Table 5). First, the effective temperature was calculated by requiring that the resulting abundance be independent of the lower LEP.

If all lines have the same LEP and a similar wavelength, the microturbulence (ξ) is determined by requiring that the calculated abundance be independent of the reduced equivalent width (EW). The precision in the determination of the microturbulent velocity is ± 0.5 km s⁻¹. We determined the surface gravity ($\log g$) by ensuring ionization equilibrium, which requires that the Fe I and Fe II lines yield the same iron abundance. (Figures 3 and 4). Due to the interdependence of model parameters, an iterative procedure is required. Between each of the above steps, minor adjustments are made to the model parameters. We also confirmed that there is no substantial trend in iron abundances (see Figures 3 and 4 for the Sun and HD 218209, respectively).

The model parameters obtained for the Sun as a result of the Solar analysis were determined as $T_{\text{eff}} = 5790$ K, $\log g = 4.4$ cgs, $[\text{Fe}/\text{H}] = 0$ dex and $\xi = 0.66$ km s⁻¹. These values are similar to those recommended by Heiter et al. (2015) as $(T_{\text{eff}}, \log g) = (5771, 4.438)$. Element abundances for the Sun were calculated with these model parameters. For HD 218209, the model parameters were obtained from ELODIE and POLARBASE spectrum of the star.

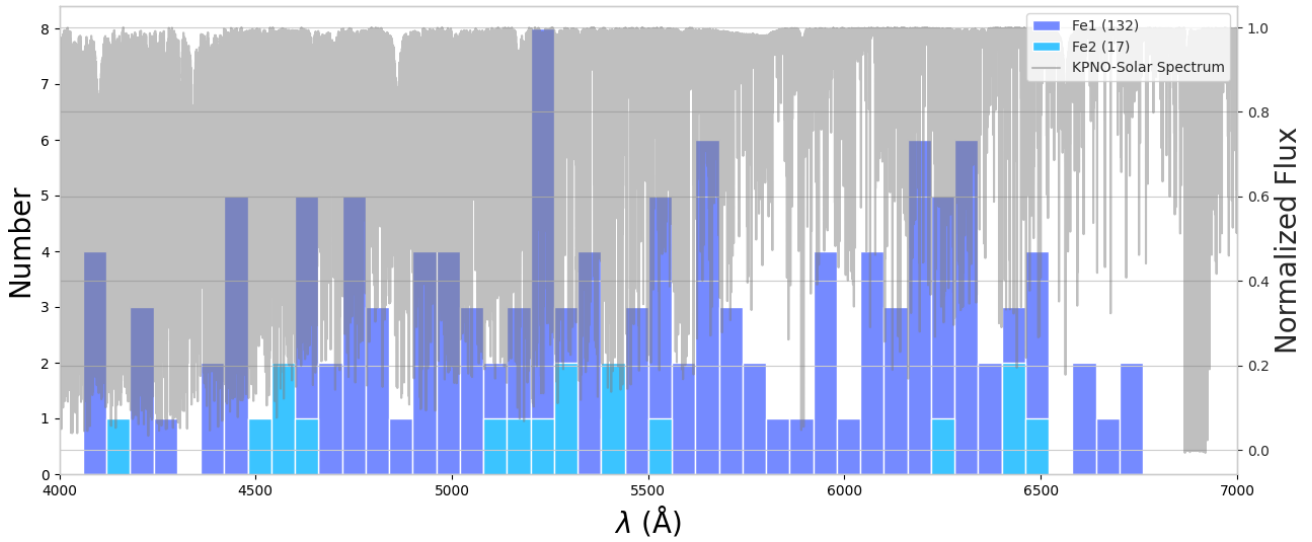


Figure 2. The KPNO Solar spectrum and the number of identified lines in the respective wavelength regions (each bar indicates 50 Å region of the spectrum).

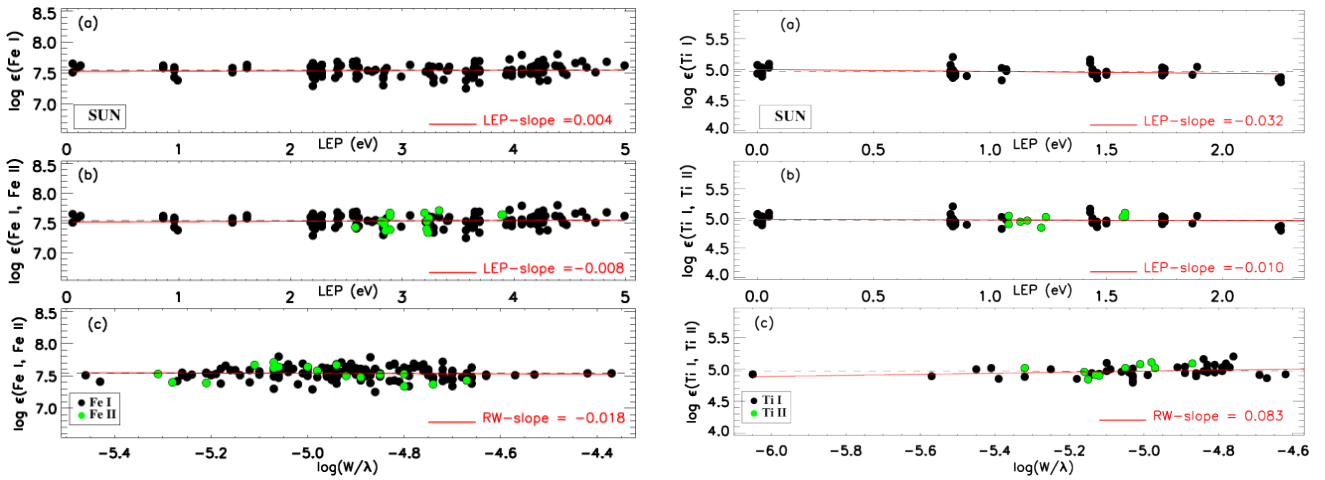


Figure 3. An example for the determination of the atmospheric parameters T_{eff} and ξ using abundance ($\log \epsilon$) as a function of both lower LEP (panels a and b for Fe and Ti, respectively) and reduced EW (REW; $\log (EW/\lambda)$), panels c for Fe and Ti, respectively) for the Sun. In all panels, the solid red line represents the least-squares fit to the data.

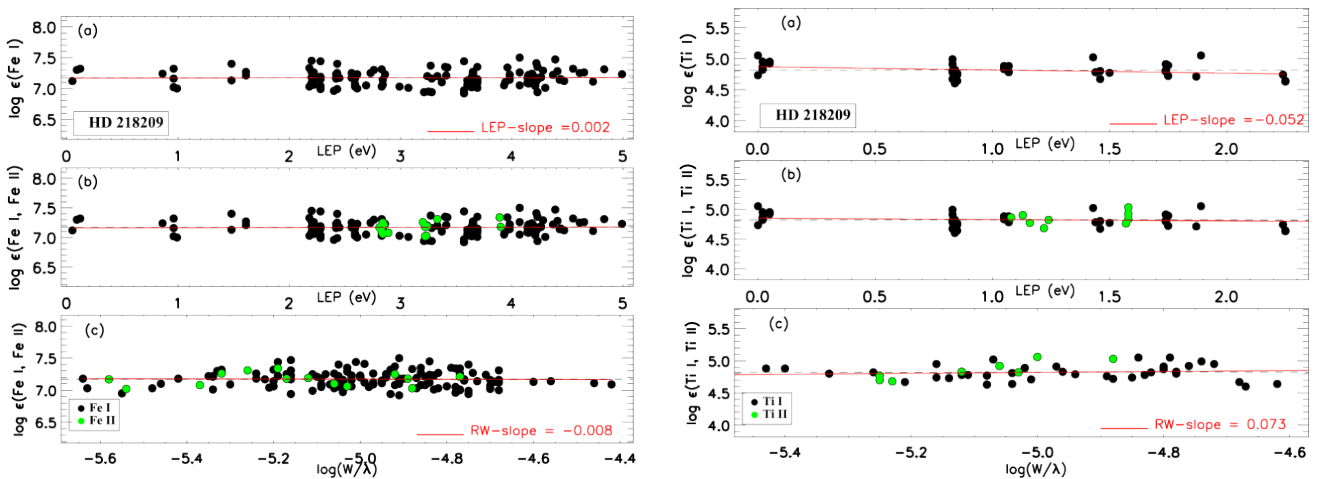


Figure 4. An example for the determination of the atmospheric parameters T_{eff} and ξ using abundance ($\log \epsilon$) as a function of both lower LEP (panels a and b for Fe and Ti, respectively) and reduced EW (REW; $\log (EW/\lambda)$), panels c for Fe and Ti, respectively) for HD 218209 and the ELODIE spectrum. In all panels, the solid red line represents the least-squares fit to the data.

Table 1. Fe I and Fe II lines. The abundances are obtained for a model of $T_{\text{eff}} = 5790$ K, $\log g = 4.4$ cgs, and $\xi = 0.66$ km s⁻¹.

Spec.	Sun				HD 218209				Spec.	Sun				HD 218209			
	λ (Å)	LEP (eV)	$\log(gf)$ (dex)	EW (mÅ)	$\log \epsilon(X)$ (dex)	EW (mÅ)	$\log \epsilon(X)$ (dex)	RMT		λ (Å)	LEP (eV)	$\log(gf)$ (dex)	EW (mÅ)	$\log \epsilon(X)$ (dex)	EW (mÅ)	$\log \epsilon(X)$ (dex)	RMT
Fe I	4080.22	3.28	-1.23	80.9	7.34	85.1	7.16	558	Fe I	5618.64	4.21	-1.28	49.3	7.47	34.3	7.04	1107
Fe I	4082.11	3.42	-1.51	72.7	7.60	69.8	7.34	698	Fe I	5624.03	4.39	-1.20*	49.2	7.55	38.9	7.22	1160
Fe I	4088.56	3.64	-1.50	52.4	7.43	43.9	7.09	906	Fe I	5633.95	4.99	-0.32	67.3	7.62	53.2	7.23	1314
Fe I	4090.96	3.37	-1.73	55.5	7.39	49.9	7.10	700	Fe I	5636.71	3.64	-2.56	19.6	7.51	13.0	7.18	868
Fe I	4204.00	2.84	-1.01	125.1	7.52	115.9	7.14	355	Fe I	5638.27	4.22	-0.84	75.4	7.54	61.1	7.12	1087
Fe I	4207.13	2.83	-1.41	83.5	7.44	88.1	7.31	352	Fe I	5641.45	4.26	-1.15	66.0	7.71	45.4	7.18	1087
Fe I	4220.35	3.07	-1.31	91.4	7.63	70.9	7.01	482	Fe I	5662.52	4.18	-0.57	92.4	7.61	81.1	7.24	1087
Fe I	4291.47	0.05	-4.08	92.3	7.51	87.1	7.12	3	Fe I	5701.56	2.56	-2.22	87.1	7.68	70.6	7.17	209
Fe I	4365.90	2.99	-2.25	49.2	7.44	38.1	7.03	415	Fe I	5705.47	4.30	-1.36	37.5	7.38	25.8	7.01	1087
Fe I	4389.25	0.05	-4.58	75.4	7.65	63.9	7.12	2	Fe I	5717.84	4.28	-1.10	63.3	7.62	53.8	7.29	1107
Fe I	4432.58	3.57	-1.56	51.4	7.38	40.2	6.97	797	Fe I	5741.86	4.26	-1.67	31.5	7.51	21.8	7.18	1086
Fe I	4439.89	2.28	-3.00	48.4	7.49	34.4	6.99	116	Fe I	5778.46	2.59	-3.43	21.5	7.41	13.6	7.03	209
Fe I	4442.35	2.20	-1.25	187.7	7.54	167.6	7.09	68	Fe I	5806.73	4.61	-1.03	56.4	7.69	39.7	7.25	1180
Fe I	4447.14	2.20	-2.73	66.2	7.66	64.1	7.45	69	Fe I	5916.26	2.45	-2.99	54.5	7.62	40.7	7.17	170
Fe I	4447.73	2.22	-1.34	171.0	7.54	155.7	7.11	68	Fe I	5929.68	4.55	-1.38	39.7	7.66	28.6	7.32	1176
Fe I	4502.60	3.57	-2.31	28.9	7.53	29.1	7.44	796	Fe I	5934.67	3.93	-1.12	76.6	7.47	61.7	7.05	982
Fe I	4556.93	3.25	-2.66	25.9	7.48	12.7	6.95	638	Fe I	5952.73	3.98	-1.39	59.6	7.50	53.0	7.22	959
Fe I	4593.53	3.94	-2.03	28.3	7.54	16.1	7.10	971	Fe I	5956.71	0.86	-4.61	52.8	7.62	-	-	14
Fe I	4602.01	1.61	-3.15	72.0	7.58	64.8	7.21	39	Fe I	6027.06	4.07	-1.09	62.7	7.48	48.8	7.05	1018
Fe I	4602.95	1.48	-2.22	122.5	7.51	116.3	7.13	39	Fe I	6065.49	2.61	-1.53	118.5	7.45	102.9	7.00	207
Fe I	4619.30	3.60	-1.08	84.1	7.45	73.7	7.06	821	Fe I	6079.02	4.65	-1.10	45.6	7.59	34.8	7.26	1176
Fe I	4630.13	2.28	-2.59	72.7	7.63	61.9	7.19	115	Fe I	6082.72	2.22	-3.57	35.2	7.52	28.1	7.21	64
Fe I	4635.85	2.84	-2.36	54.9	7.54	41.2	7.06	349	Fe I	6096.67	3.98	-1.88	37.5	7.55	27.2	7.22	959
Fe I	4678.85	3.60	-0.83	102.5	7.47	95.2	7.13	821	Fe I	6127.91	4.14	-1.40	48.3	7.52	37.3	7.17	1017
Fe I	4704.95	3.69	-1.53	61.5	7.55	48.6	7.12	821	Fe I	6137.70	2.59	-1.40	135.6	7.48	122.8	7.07	207
Fe I	4728.55	3.65	-1.17	81.3	7.65	69.3	7.23	822	Fe I	6157.73	4.07	-1.22	61.0	7.56	53.2	7.26	1015
Fe I	4733.60	1.48	-2.99	82.9	7.58	84.8	7.40	38	Fe I	6165.36	4.14	-1.47	44.6	7.51	30.7	7.09	1018
Fe I	4735.85	4.07	-1.32	64.1	7.79	57.6	7.50	1042	Fe I	6173.34	2.22	-2.88	68.9	7.61	58.6	7.22	62
Fe I	4741.53	2.83	-1.76	72.6	7.41	63.5	7.03	346	Fe I	6180.21	2.73	-2.65	53.4	7.52	47.6	7.25	269
Fe I	4745.81	3.65	-1.27	78.2	7.69	66.2	7.27	821	Fe I	6200.32	2.61	-2.44	71.5	7.59	62.6	7.23	207
Fe I	4788.77	3.24	-1.76	65.6	7.61	55.0	7.20	588	Fe I	6213.44	2.22	-2.48	82.5	7.50	75.6	7.18	62
Fe I	4802.89	3.64	-1.51	60.0	7.52	44.3	7.02	888	Fe I	6219.29	2.20	-2.43	87.9	7.54	79.1	7.18	62
Fe I	4839.55	3.27	-1.82	62.2	7.60	58.3	7.37	588	Fe I	6232.65	3.65	-1.22	81.5	7.60	71.9	7.25	816
Fe I	4875.88	3.33	-1.97	61.0	7.60	49.2	7.20	687	Fe I	6240.65	2.22	-3.17	47.6	7.40	39.1	7.06	64
Fe I	4917.23	4.19	-1.16	62.7	7.61	49.4	7.21	1066	Fe I	6252.56	2.40	-1.69	119.6	7.42	103.2	6.96	169
Fe I	4918.02	4.23	-1.34	53.0	7.63	45.5	7.35	1070	Fe I	6265.14	2.18	-2.55	86.2	7.60	82.5	7.33	62
Fe I	4924.78	2.28	-2.11	92.8	7.52	85.2	7.15	114	Fe I	6270.23	2.86	-2.61	53.0	7.58	43.1	7.23	342
Fe I	4939.69	0.86	-3.34	99.7	7.58	95.8	7.24	16	Fe I	6297.80	2.22	-2.74	73.6	7.56	67.1	7.26	62
Fe I	4961.92	3.63	-2.25	26.5	7.42	16.4	7.03	845	Fe I	6301.51	3.65	-0.72	112.7	7.57	106.2	7.26	816
Fe I	4962.58	4.18	-1.18	54.0	7.51	40.3	7.09	66	Fe I	6315.81	4.07	-1.66	39.8	7.51	-	-	1014
Fe I	4973.10	3.96	-0.92	93.8	7.72	82.4	7.34	173	Fe I	6322.69	2.59	-2.43	78.6	7.69	61	7.16	207
Fe I	5002.80	3.40	-1.53	78.8	7.54	81.2	7.35	687	Fe I	6335.34	2.20	-2.18	96.3	7.43	88.6	7.08	62
Fe I	5022.24	3.98	-0.56	99.5	7.45	93.9	7.14	965	Fe I	6336.83	3.69	-0.86	102.4	7.34	94.8	7.01	816
Fe I	5029.62	3.41	-2.00	48.7	7.54	40.0	7.21	718	Fe I	6344.15	2.43	-2.92	59.2	7.61	56.4	7.40	169
Fe I	5074.75	4.22	-0.23	118.8	7.50	105.8	7.12	1094	Fe I	6393.61	2.43	-1.58	134.6	7.48	113.4	6.99	168
Fe I	5083.35	0.96	-2.96	109.9	7.43	101.8	7.02	16	Fe I	6408.03	3.69	-1.02	97.3	7.69	88.1	7.35	816
Fe I	5088.16	4.15	-1.75	34.8	7.59	23.5	7.22	1066	Fe I	6419.96	4.73	-0.27	86.8	7.51	71.3	7.11	1258
Fe I	5141.75	2.42	-2.24	89.3	7.68	76.5	7.23	114	Fe I	6430.86	2.18	-2.01	115.3	7.51	97.9	7.03	62
Fe I	5145.10	2.20	-3.08*	52.5	7.49	49.0	7.26	66	Fe I	6469.19	4.83	-0.81	58.6	7.68	44.5	7.31	1258
Fe I	5198.72	2.22	-2.13	94.9	7.48	91.1	7.17	66	Fe I	6481.88	2.28	-2.98	64.7	7.63	62.9	7.44	109
Fe I	5217.40	3.21	-1.16	121.7	7.52	93.8	6.94	553	Fe I	6498.94	0.96	-4.69	45.7	7.59	40.9	7.32	13
Fe I	5228.38	4.22	-1.26	60.0	7.68	53.5	7.41	1091	Fe I	6518.37	2.83	-2.46†	56.0	7.46	-	-	342
Fe I	5242.50	3.63	-0.97	85.7	7.50	73.2	7.08	843	Fe I	6593.88	2.43	-2.42	83.7	7.60	75.0	7.25	168
Fe I	5243.78	4.26	-1.12	63.0	7.64	46.6	7.18	1089	Fe I	6609.12	2.56	-2.69	65.6	7.62	55.1	7.25	206
Fe I	5247.06	0.09	-4.95	65.3	7.58	61.3	7.30	1	Fe I	6678.00	2.69	-1.42	133.5	7.54	112.1	7.05	268
Fe I	5250.22	0.12	-4.94	65.9	7.62	61.5	7.32	1	Fe I	6703.58	2.76	-3.06	37.2	7.55	31.7	7.30	268
Fe I	5250.65	2.20	-2.18	100.6	7.60	95.7	7.27	66	Fe I	6750.16	2.42	-2.62	73.3	7.56	61.8	7.16	111
Fe I	5253.47	3.28	-1.57	77.9	7.42	62.2	6.94	553	Fe II	4178.86	2.58	-2.51*	89.7	7.50	77.2	7.19	28
Fe I	5288.53	3.69	-1.51	58.6	7.52	48.4	7.15	929	Fe II	4508.29	2.85	-2.44*	82.1	7.46	76.6	7.30	38
Fe I	5298.78	3.64	-2.02	42.2	7.57	30.3	7.18	875	Fe II	4576.34	2.84	-2.92	65.3	7.52	54.8	7.25	38
Fe I	5307.37	1.61	-2.99	87.6	7.63	80.3	7.27	36	Fe II	4582.83	2.84	-3.06	58.6	7.48	42.8	7.06	37
Fe I	5322.05	2.28	-2.80	59.4	7.44	48.9	7.04	112	Fe II	4620.52	2.83	-3.19	55.3	7.50	39.8	7.10	38
Fe I	5365.41	3.57	-1.22*	74.4	7.45	66.3	7.12	786	Fe II	5132.67	2.81	-4.09	25.1	7.53	13.6	7.17	35
Fe I	5373.71	4.47	-0.84	61.1	7.47	49.5	7.12	1166	Fe II	5197.58	3.23	-2.22*	81.6	7.51	68.3	7.20	49
Fe I	5379.58	3.69	-1.51	59.7	7.53	46.1	7.09	928	Fe II	5234.63	3.22	-2.21	83.8	7.53	68.2	7.18	49
Fe I	5398.29	4.44	-0.71	71.1	7.50	60.3	7.15	553	Fe II	5264.81	3.33	-3.13*	45.2	7.61	29.0	7.21	48
Fe I	5473.91	4.15	-0.79	78.2	7.49	65.1	7.08	1062	Fe II	5284.11	2.89	-3.11*	61.1	7.58	-	-	41
Fe I	5483.11	4.15	-1.41	46.2	7.49	-	-	1061	Fe II	5414.07	3.22	-3.58*	28.6	7.50	15.5	7.12	48
Fe I	5487.15	4.41	-1.51	36.5	7.61	26.3	7.28	1143	Fe II	5425.26	3.20	-3.22*	42.5	7.50	26.2	7.09	49
Fe I	5501.48	0.96	-3.05	116.6	7.54	109.8	7.16	15	Fe II	5534.85	3.24	-2.75*	58.3	7.48	41.7	7.08	55
Fe I	5506.79	0.99	-2.80	121.6	7.38	115.1	7.00	15	Fe II	6247.56	3.89	-2.30*	54.1	7.51	40.6	7.21	74
Fe I	5525.55	4.23</															

Table 2 continued

Spec.	Sun					HD 218209					Spec.	Sun					HD 218209				
	λ (Å)	LEP (eV)	$\log(gf)$ (dex)	EW (mÅ)	$\log \epsilon(X)$ (dex)	EW (mÅ)	$\log \epsilon(X)$ (dex)	RMT	Ref.	λ (Å)		LEP (eV)	$\log(gf)$ (dex)	EW (mÅ)	$\log \epsilon(X)$ (dex)	EW (mÅ)	$\log \epsilon(X)$ (dex)	RMT	Ref.		
Ni I	4410.52	3.31	-1.08	57.8	6.39	43.1	5.94	88	4	Ni I	5748.36	1.68	-3.26	28.8	6.26	19.3	5.87	45	4		
Ni I	4470.48	3.40	-0.40	79.5	6.24	76.2	5.98	86	4	Ni I	5805.23	4.17	-0.64	40.5	6.30	28.2	5.93	234	4		
Ni I	4606.23	3.60	-1.02	48.0	6.37	38.8	6.05	100	4	Ni I	6007.32	1.68	-3.34	25.4	6.24	22.5	6.04	42	4		
Ni I	4686.22	3.60	-0.64	62.3	6.30	58.9	6.08	98	4	Ni I	6086.29	4.26	-0.51	43.5	6.30	28.2	5.88	249	4		
Ni I	4731.80	3.83	-0.85	45.4	6.35	26.6	5.82	163	4	Ni I	6108.12	1.68	-2.44	65.6	6.30	55.3	5.92	45	4		
Ni I	4732.47	4.10	-0.55	44.3	6.29	30.6	5.89	235	4	Ni I	6128.98	1.68	-3.32	25.3	6.21	20.1	5.94	42	4		
Ni I	4752.43	3.66	-0.69	59.1	6.33	43.1	5.86	132	4	Ni I	6130.14	4.26	-0.96	21.6	6.24	11.5	5.82	248	4		
Ni I	4756.52	3.48	-0.34	77.5	6.19	76.1	5.96	98	4	Ni I	6175.37	4.09	-0.54	50.7	6.32	36.4	5.92	217	4		
Ni I	4806.99	3.68	-0.64	61.4	6.35	54.7	6.07	163	4	Ni I	6176.82	4.09	-0.53	63.0	6.54	48.0	6.13	228	4		
Ni I	4829.03	3.54	-0.33	80.1	6.24	68.7	5.85	131	4	Ni I	6204.61	4.09	-1.14	21.7	6.26	18.2	6.08	226	4		
Ni I	4852.56	3.54	-1.07	44.7	6.28	42.3	6.10	130	4	Ni I	6322.17	4.15	-1.17	18.3	6.24	—	—	249	4		
Ni I	4904.42	3.54	-0.17	87.1	6.19	78.1	5.84	129	4	Ni I	6327.60	1.68	-3.15	37.9	6.34	27.8	5.97	44	4		
Ni I	4913.98	3.74	-0.62	55.3	6.24	42.3	5.84	132	4	Ni I	6378.26	4.15	-0.90	31.5	6.32	23.5	6.04	247	4		
Ni I	4935.83	3.94	-0.36	62.9	6.30	48.5	5.88	177	4	Ni I	6414.59	4.15	-1.21	16.8	6.23	—	—	244	4		
Ni I	4946.03	3.80	-1.29	28.0	6.35	17.0	5.96	148	4	Ni I	6482.81	1.93	-2.63	40.8	6.12	31.8	5.79	66	4		
Ni I	4953.21	3.74	-0.66	56.2	6.30	40.9	5.85	111	4	Ni I	6598.61	4.23	-0.98	24.7	6.30	—	—	249	4		
Ni I	4998.23	3.61	-0.78	57.5	6.33	43.2	5.90	111	4	Ni I	6635.14	4.42	-0.83	24.0	6.31	15.2	5.97	264	4		
Ni I	5010.94	3.63	-0.87	48.4	6.23	33.4	5.79	144	4	Ni I	6767.78	1.83	-2.17	79.6	6.47	67.4	6.06	57	4		
Ni I	5032.73	3.90	-1.27	23.8	6.31	16.2	6.00	207	4	Ni I	6772.32	3.66	-0.99	48.4	6.27	35.3	5.89	127	4		
Ni I	5035.37	3.63	0.29	107.0	6.05	91.5	5.63	143	4	Zn I	4722.16	4.03	-0.39	66.1	4.70	65.0	4.58	2	12		
Ni I	5042.19	3.64	-0.57	61.8	6.21	52.6	5.88	131	4	Zn I	4810.54	4.08	-0.17	72.3	4.66	73.6	4.58	2	12		
Ni I	5048.85	3.85	-0.37	66.1	6.29	51.5	5.86	195	4	Sr I	4607.34	0.00	0.28	45.4	2.91	32.0	2.28	2	13		
Ni I	5082.35	3.66	-0.54	62.5	6.22	55.2	5.92	130	4	Y II	4883.69	1.08	0.07	57.6	2.33	53.4	2.15	22	14		
Ni I	5084.10	3.68	0.03	91.1	6.14	78.2	5.75	162	4	Y II	5087.43	1.08	-0.17	48.3	2.25	31.1	1.69	20	14		
Ni I	5088.54	3.85	-0.91	31.9	6.12	23.9	5.83	190	4	Zr II	4208.98	0.71	-0.46	44.7	2.68	39.3	2.45	41	15		
Ni I	5102.97	1.68	-2.62	48.1	6.16	36.7	5.74	49	4	Ba II	4554.04	0.00	0.14	174.6	2.17	154.7	1.78	1	16		
Ni I	5115.40	3.83	-0.11	75.2	6.19	68.9	5.90	177	4	Ba II	5853.69	0.60	-0.91	62.8	2.28	51.2	1.87	2	16		
Ni I	5155.13	3.90	-0.66	49.2	6.28	34.5	5.86	206	4	Ba II	6141.71	0.70	-0.03	112.2	2.23	98.9	1.87	2	16		
Ni I	5435.87	1.99	-2.60	52.0	6.52	40.0	6.09	70	4	Ba II	6496.91	0.60	-0.41	97.5	2.30	90.6	2.01	2	16		
Ni I	5587.87	1.93	-2.14	55.8	6.08	39.7	5.56	70	4	Ce II	4562.37	0.48	0.21	21.9	1.65	18.6	1.47	1	17		
Ni I	5593.75	3.90	-0.84	45.4	6.35	28.3	5.88	206	4	Ce II	4628.16	0.52	0.14	18.4	1.63	12.9	1.34	1	17		
Ni I	5625.33	4.09	-0.70	38.1	6.24	28.8	5.94	221	4	Nd II	4446.40	0.20	-0.35	12.7	1.41	8.0	1.08	49	18		
Ni I	5637.12	4.09	-0.80	33.3	6.23	—	—	218	4	Nd II	5092.80	0.38	-0.61	7.0	1.48	—	—	48	18		
Ni I	5641.89	4.10	-1.08	24.6	6.31	13.1	5.87	234	4	Nd II	5293.17	0.82	0.10	10.3	1.39	—	—	75	18		
Ni I	5682.21	4.10	-0.47	51.9	6.30	33.9	5.83	232	4	Sm II	4577.69	0.25	-0.65	5.2	0.96	—	—	23	19		

References for the adopted gf -values: (1) Takeda et al. (2003), (2) Pehlivan Rhodin et al. (2017), (3) Shi et al. (2011), (4) NIST Atomic Spectra Database (<http://physics.nist.gov/PhysRefData/ASD>), (5) Den Hartog et al. (2021), (6) Lawler et al. (2019), (7) Lawler et al. (2013), (8) Lawler et al. (2014), (9) Lawler et al. (2017), (10) Den Hartog et al. (2011), (11) Lawler et al. (2015), (12) Biemont & Godefroid (1980), (13) Hansen et al. (2013), (14) Hannaford et al. (1982), (15) Biemont et al. (1981), (16) Klose et al. (2002), (17) Lawler et al. (2009), (18) Den Hartog et al. (2003), (19) Lawler et al. (2006), (†) Bard & Kock (1994), (*) Meléndez & Barbuy (2009)

During the calculation of the model atmosphere, the effect of convection on the reported abundances is also taken into consideration. In one-dimensional (1D) atmosphere modeling, it is currently common practice to assume a universal value of 1.5 for the mixing length parameter (α). However, in order to test the impact of convection on final abundances in this study, the ATLAS models were produced using two different methods for calculating α . Two well known references in the literature, Ludwig et al. (1999) and Magic et al. (2015), for the calculation of α , yields two different values (1.59 and 1.98) even when the same set of model parameters is employed. The logarithmic abundance of ionized iron showed a 0.01 dex increase for the model atmosphere computed with the α parameter set to 1.59 and the model parameters from the ELODIE spectrum. For $\alpha = 1.98$, it is +0.02 dex. With regards to the FGK dwarf field stars, it is expected that the influence of the mixing length parameter, for instance, on the determination of metallicity would be minimal, amounting to less than 0.02 dex over eight dwarf stars (Song et al. 2020). Thus, our results for HD 218209 confirm those of Song et al. (2020). Regarding the model parameters of HD 218209 from the POLARBASE spec-

trum, the logarithmic abundance of ionized iron remained the same for the model atmosphere computed with $\alpha = 1.59$. The difference in logarithmic abundance is 0.02 dex for $\alpha = 1.98$.

The resulting stellar model parameters for HD 218209 along with our determination of model parameters of the Sun are listed in Table 5. Table 4 lists the model parameters reported for the star in the literature. Rebolo et al. (1988), Abia et al. (1988), and Kim et al. (2016) show the largest variations compared to our $\log g$. The abundances obtained for the Solar photosphere as a result of the Solar analysis are given in Table 3. The Solar abundances from Asplund et al. (2009) are also included for comparison. In Table 3, we provide a summary of element abundances based on LTE-based model parameters. $\log \epsilon$ is the logarithm of the abundances. The errors reported in $\log \epsilon$ abundances are the 1σ line-to-line scatter in abundances. $[X/H]$ is the logarithmic abundance ratio of hydrogen to the corresponding Solar value, and $[X/Fe]$ is the logarithmic abundance considering the Fe I abundance. The error in $[X/Fe]$ is the square root of the sum of the quadratures of the errors in $[X/H]$ and $[Fe/H]$. Table 3 also presents the abundances obtained using the PolarBase spectrum of the star as $[X/Fe]$ ratio.

Table 3. Solar abundances obtained by employing the Solar model atmosphere from [Castelli & Kurucz \(2003\)](#) compared to the photospheric abundances from [Asplund et al. \(2009\)](#). The abundances were calculated using the line EWs.

Species	HD 218209				Sun [†]		Asplund et al. (2009)		$\Delta \log \epsilon_{\odot}(X)$
	$\log \epsilon(X)^1$ (dex)	$[X/Fe]^1$ (dex)	$[X/Fe]^2$ (dex)	N^1	$\log \epsilon_{\odot}(X)$	N	$\log \epsilon_{\odot}(X)$ (dex)		
Na I	5.79±0.09	-0.02±0.14	0.00±0.18	2	6.16±0.07	2	6.24±0.04	0.08	
Mg I	7.48±0.06	0.23±0.13	0.09±0.20	2	7.60±0.08	2	7.60±0.04	0.00	
Si I	7.28±0.09	0.13±0.14	0.13±0.19	11	7.50±0.07	12	7.51±0.03	0.01	
Ca I	6.09±0.10	0.10±0.15	0.10±0.19	18	6.34±0.08	18	6.34±0.04	0.00	
Sc I	2.78±0.00	0.01±0.08	-0.33±0.14	1	3.12±0.00	1	3.15±0.04	0.03	
Sc II	3.05±0.06	0.17±0.13	0.18±0.20	7	3.23±0.08	7	3.15±0.04	0.08	
Ti I	4.82±0.12	0.21±0.17	0.21±0.21	39	4.96±0.09	43	4.95±0.05	0.01	
Ti II	4.86±0.13	0.22±0.17	0.18±0.19	12	4.99±0.08	12	4.95±0.05	0.04	
V I	3.81±0.07	0.17±0.12	0.05±0.15	4	3.99±0.05	5	3.93±0.08	0.06	
Cr I	5.30±0.11	-0.06±0.15	-0.01±0.18	19	5.71±0.07	19	5.64±0.04	0.07	
Cr II	5.32±0.16	0.03±0.23	-0.01±0.20	3	5.64±0.14	3	5.64±0.04	0.00	
Mn I	5.06±0.15	-0.21±0.21	-0.23±0.23	12	5.62±0.13	13	5.43±0.05	0.19	
Fe I	7.17±0.12	-0.02±0.17	-0.01±0.20	128	7.54±0.09	132	7.50±0.04	0.04	
Fe II	7.16±0.07	0.00±0.11	0.00±0.19	15	7.51±0.04	17	7.50±0.04	0.01	
Co I	4.62±0.15	0.00±0.23	0.03±0.26	6	4.97±0.15	7	4.99±0.07	0.02	
Ni I	5.91±0.12	-0.02±0.17	-0.03±0.21	50	6.28±0.09	54	6.22±0.04	0.06	
Zn I	4.58±0.01	0.25±0.09	0.26±0.17	2	4.68±0.03	2	4.56±0.05	0.12	
Sr I	2.28±0.00	-0.28±0.08	-0.16±0.14	1	2.91±0.00	1	2.87±0.07	0.04	
Y II	1.92±0.32	-0.02±0.33	-0.15±0.22	2	2.29±0.05	2	2.21±0.05	0.08	
Zr II	2.45±0.00	0.12±0.08	0.27±0.14	1	2.68±0.00	1	2.58±0.04	0.10	
Ba II	1.88±0.09	-0.01±0.13	0.06±0.20	4	2.24±0.06	4	2.18±0.09	0.06	
Ce II	1.40±0.09	0.11±0.12	0.25±0.21	2	1.64±0.02	2	1.58±0.04	0.06	
Nd II	1.08±0.00	0.01±0.09	0.19±0.14	1	1.42±0.05	3	1.42±0.04	0.00	
Sm II	-	-	-	-	0.96±0.00	1	0.96±0.04	0.00	

(1) The abundances are obtained using the ELODIE spectrum. (2) The abundances are obtained using the POLARBASE spectrum.

(*) $\Delta \log \epsilon_{\odot}(X) = \log \epsilon_{\odot}(X)_{\text{This study}} - \log \epsilon_{\odot}(X)_{\text{Asplund}}$. (†) The Solar abundances calculated in this study.**Table 4.** Atmospheric parameters of HD 218209 from this study.

T_{eff} (K)	$\log g$ (cgs)	[Fe/H] (dex)	Notes
5650	4.55	-0.37	This study (ELODIE)
5630	4.43	-0.32	This study (POLARBASE)
5506	4.38	-0.46	Takeda (2023)
5636	4.56	-0.47	Rice & Brewer (2020)
5518	4.39	-0.49	Aguilera-Gómez et al. (2018)
5623	4.46	-0.40	Luck (2017)
5555	4.26	-0.49	Boeche & Grebel (2016)
5565	4.29	-0.49	Boeche & Grebel (2016)
5669	4.24	-0.39	Kim et al. (2016)
5575	4.11	-0.46	Kim et al. (2016)
5607	4.07	-0.58	Kim et al. (2016)
5536	4.37	-0.46	Da Silva et al. (2015)
5705	4.50	-0.43	Mishenina et al. (2015)
5705	4.50	-0.43	Mishenina et al. (2013)
5592	4.25	-0.51	Lee et al. (2011)
5592	4.33	-0.61	Lee et al. (2011)
5592	4.31	-0.65	Lee et al. (2011)
5705	4.50	-0.43	Mishenina et al. (2011)
5539	4.37	-0.50	Da Silva et al. (2011)
5600	-	-	Casagrande et al. (2011)
5473	4.57	-0.64	Sozzetti et al. (2009)
5506	4.38	-0.46	Takeda et al. (2007)
5693	-	-	Masana et al. (2006)
5585	4.60	-0.46	Valenti & Fischer (2005)
5684	-	-	Kovtyukh et al. (2004)
5705	4.50	-0.43	Mishenina et al. (2004)
5665	4.40	-0.60	Gehren et al. (2004)
5478	4.00	-0.60	Rebolo et al. (1988)
5478	4.00	-0.60	Abia et al. (1988)

Table 5. Model atmosphere parameters for HD 218209 and the Sun.

Star	T_{eff} (K)	$\log g$ (cgs)	[Fe/H] (dex)	ξ (km s ⁻¹)
HD 218209 [†]	5650 ⁺⁸⁵ ₋₈₅	4.55 ^{+0.13} _{-0.13}	-0.35 ^{+0.07} _{-0.07}	0.60 ^{+0.50} _{-0.50}
HD 218209 [*]	5630 ⁺¹⁴⁵ ₋₁₄₅	4.43 ^{+0.24} _{-0.24}	-0.31 ^{+0.13} _{-0.13}	0.35 ^{+0.50} _{-0.50}
Sun	5790 ⁺⁴⁵ ₋₄₅	4.40 ^{+0.09} _{-0.09}	0.00 ^{+0.04} _{-0.04}	0.66 ^{+0.50} _{-0.50}

(†) The ELODIE spectrum was used.

(*) The PolarBase spectrum was used.

4. SUMMARY AND CONCLUSION

We present a line list that can be useful for abundance analysis of G-type stars over 4080 – 6780 Å wavelength region (i.e. for spectra from the ELODIE/SOPHIE library). The line list is expected to be useful for the surveys/libraries with overlapping spectral regions (e.g. ELODIE library, UVES-580 setting of *Gaia*-ESO, and, especially, for the analysis of F- and G-type stars in general). We identified 363 lines of 24 species that have accurate gf -values and are free of blends in the spectra of the Sun and a Solar analogue star, HD 218209. It should be noted that the GES line list does not contain any atomic transitions below 4200 Å and unlike the GES line list, the line list created in this study contains additional four Fe I, one Fe II, 1 Sc I, 2 Ti I and 1 Co I line below this limit. To assess the uncertainty in $\log gf$ -values and to minimise systematic errors, we calculated Solar abundances using stellar lines and the high-resolution

KPNO spectrum of the Sun. For the creation of the line list in this study, high resolution and high signal to noise ELODIE spectrum of HD 218209 was used. During the comparison with the GES line list, discrepancies in the $\log gf$ values of some ions were detected. For example, the average difference in $\log gf$ values for 5 V I lines was 0.325 ± 0.328 dex. Similarly, for 11 Mn I lines, the difference was 0.288 ± 0.283 dex. The largest difference detected was 0.585 ± 0.161 dex over 6 Co I lines. For the other elements reported in the new line list presented in this study, the $\log gf$ difference was less than 0.1 dex.

To verify the accuracy of the model parameters obtained for HD 218209 from the ELODIE spectrum, we analyzed the POLARBASE spectrum of the same star. The model parameters from both spectra matched quite well, taking into account the error margins. The element abundances obtained from both spectra also matched quite well, except for Sc I which was represented by a single line at 4023.69 \AA in both spectra. The logarithmic abundance from this line in the ELODIE spectrum showed a 0.3 dex increase. Additionally, three other species (Sr I, Zr II, and Ce II), with the latter two presented by two transitions in the spectra, had discrepancies in their logarithmic abundances at around 0.2 dex level. Although the POLARBASE spectrum had higher resolution than the ELODIE spectrum, several lines in the POLARBASE did not have clear line profiles. Unfortunately, there was only one spectrum available in the POLARBASE archive, so a more thorough analysis is recommended to check the abundances of the star from the POLARBASE spectrum.

The model parameters obtained for HD 218209 clearly indicate a Solar analogue character for the star. Although no definite classification scheme exists, Solar analogue stars are defined as the dwarf stars of early G-type which have properties analogous to the Sun (e.g. differences in T_{eff} and $\log g$ are $\pm \leq 100\text{--}200 \text{ K}$ and $\pm \leq 0.1\text{--}0.2$ dex). Indeed, seeing the star listed in a recent study by Takeda (2023) as a Solar analogue was not surprising for us. The model parameters ($T_{\text{eff}} = 5506 \text{ K}$, $\log g = 4.38$ cgs, $[\text{Fe}/\text{H}] = -0.46$ dex, $\xi = 0.74 \text{ km s}^{-1}$) reported by Takeda (2023) are in good agreement with those obtained in this study. However, we report up-to-date abundances for the star using 24 species identified in both ELODIE and POLARBASE spectra of the star.

HD 218209 is listed in *Gaia* DR2 (Gaia Collaboration et al. 2018) with *Gaia* DR2 2213415145505277824 designation and a T_{eff} of 5648 K. The surface gravity and metallicity of the star were not reported. HD 218209 is also listed in the *Gaia* DR3 (Gaia Collaboration et al. 2023). Our spectroscopic measurements of the temperature and surface gravity of the star align very well with the values reported by the *Gaia* consortium, which are $T_{\text{eff}} = 5528 \text{ K}$ and $\log g = 4.40$ cgs. However, there seems to be an error in the reported metallicity of the star by *Gaia*, which states $[\text{Fe}/\text{H}] = -0.79$ dex. This discrepancy is likely due to the incorrect selection of the template spectrum for

the star in the *Gaia* DR3, where the metallicity of the template star is reported as -0.50 dex.

In the *Gaia* DR3 (Gaia Collaboration et al. 2023), an important addition is a collection of 220 million low-resolution BP/RP spectra. The GSP-Phot catalogue provides consistent estimations of stellar parameters for 471 million sources with $G < 19$ mag, derived from the BP/RP spectra, parallax, and integrated photometry. It assumes that each source is a single star and that any intrinsic time variability is lost when using combined BP/RP spectra. However, it is important to note that the GSP-Phot results from the BP/RP spectra in the *Gaia* DR3 may still be affected by systematic effects, particularly in the $[M/H]$ estimates with large systematic errors. Consequently, it is advised not to rely on these estimates as they can only provide qualitative information at best (Beck et al. 2023).

In a study of stellar and sub-stellar companions of nearby stars from the *Gaia* DR2 (Gaia Collaboration et al. 2018), Kervella et al. (2019) examined the status of stars exhibiting anomalies in their proper motions as binary stars. HD 218209 as a high proper-motion star happens to be one of the common stars. The study found no evidence of a companion around HD 218209, even at distances ranging from 1 to 50 astronomical units (au) and down to planetary masses. Therefore, the authors concluded that HD 218209 is a single star (P. Kervella, private communication, 2023).

Soubiran & Girard (2005), in their exploration of abundance discrepancies between the thin disc and thick disc of the Galaxy, identified HD 218209 out of the 44 stars as being part of the Hercules stream with a probability of 0.76. The Hercules stream shares chemical characteristics with the thin disc, which bolsters the dynamic hypothesis (i.e. the influence of the central bar of the Galaxy impacting stars) of its origin. However, kinematic and orbital dynamics analysis for the star is the subject of another study.

Peer Review: Externally peer-reviewed.

Author Contribution: Conception/Design of study - T.Ş., S.B.; Data Acquisition - T.Ş., M.M., N.Ç.; Data Analysis/Interpretation - T.Ş., S.B., M.M., N.Ç.; Drafting Manuscript - T.Ş.; Critical Revision of Manuscript - T.Ş., S.B., M.M., N.Ç; Final Approval and Accountability - T.Ş., S.B., M.M., N.Ç.

Conflict of Interest: Authors declared no conflict of interest.

Financial Disclosure: This study has partly been supported by the Scientific and Technological Research Council (TÜBİTAK) MFAG-121F265.

Acknowledgements: We thank Ferhat GÜNEY for his help with the preparation of Figure 2. We also thank Gizay YOLALAN and Sena A. ŞENTÜRK for helpful discussion.

Note: The Co-Editor-in-Chief was not involved in the evaluation, peer-review and decision processes of the article. These processes were carried out by the Editor-in-Chief and the member editors of the editorial management board.

LIST OF AUTHOR ORCIDS



T. Şahin <https://orcid.org/0000-0002-0296-233X>
 M. Marıřmak <https://orcid.org/0000-0002-9397-2778>
 N. Çınar <https://orcid.org/0000-0002-5155-9280>
 S. Bilir <https://orcid.org/0000-0003-3510-1509>

REFERENCES

- Abia C., Rebolo R., Beckman J. E., Crivellari L., 1988, *A&A*, **206**, 100
- Aguilera-Gómez C., Ramírez I., Chanamé J., 2018, *A&A*, **614**, A55
- Allende Prieto C., et al., 2008, *Astronomische Nachrichten*, **329**, 1018
- Asplund M., Grevesse N., Sauval A. J., Scott P., 2009, *ARA&A*, **47**, 481
- Bard A., Kock M., 1994, *A&A*, **282**, 1014
- Beck P. G., et al., 2023, *arXiv e-prints*, p. [arXiv:2307.10812](https://arxiv.org/abs/2307.10812)
- Biemont E., Godefroid M., 1980, *A&A*, **84**, 361
- Biemont E., Grevesse N., Hannaford P., Lowe R. M., 1981, *ApJ*, **248**, 867
- Boeche C., Grebel E. K., 2016, *A&A*, **587**, A2
- Casagrande L., Schönrich R., Asplund M., Cassisi S., Ramírez I., Meléndez J., Bensby T., Feltzing S., 2011, *A&A*, **530**, A138
- Castelli F., Kurucz R. L., 2003, in Piskunov N., Weiss W. W., Gray D. F., eds, Published on behalf of the IAU by the Astronomical Society of the Pacific Vol. 210, *Modelling of Stellar Atmospheres*. p. A20 ([arXiv:astro-ph/0405087](https://arxiv.org/abs/astro-ph/0405087)), doi:10.48550/arXiv.astro-ph/0405087
- Da Silva R., Milone A. C., Reddy B. E., 2011, *A&A*, **526**, A71
- Da Silva R., Milone A. d. C., Rocha-Pinto H. J., 2015, *A&A*, **580**, A24
- De Silva G. M., et al., 2015, *MNRAS*, **449**, 2604
- Den Hartog E. A., Lawler J. E., Sneden C., Cowan J. J., 2003, *ApJS*, **148**, 543
- Den Hartog E. A., Lawler J. E., Sobeck J. S., Sneden C., Cowan J. J., 2011, *ApJS*, **194**, 35
- Den Hartog E. A., Lawler J. E., Sneden C., Cowan J. J., Roederer I. U., Sobeck J., 2021, *ApJS*, **255**, 27
- Gaia Collaboration et al., 2018, *A&A*, **616**, A11
- Gaia Collaboration et al., 2023, *A&A*, **674**, A1
- Gehren T., Liang Y. C., Shi J. R., Zhang H. W., Zhao G., 2004, *A&A*, **413**, 1045
- Gilmore G., et al., 2012, *The Messenger*, **147**, 25
- Hannaford P., Lowe R. M., Grevesse N., Biemont E., Whaling W., 1982, *ApJ*, **261**, 736
- Hansen C. J., Bergemann M., Cescutti G., François P., Arcones A., Karakas A. I., Lind K., Chiappini C., 2013, *A&A*, **551**, A57
- Heijmans J., et al., 2012, in McLean I. S., Ramsay S. K., Takami H., eds, *Society of Photo-Optical Instrumentation Engineers (SPIE) Conference Series Vol. 8446, Ground-based and Airborne Instrumentation for Astronomy IV*. p. 84460W, doi:10.1117/12.925806
- Heiter U., Jofré P., Gustafsson B., Korn A. J., Soubiran C., Thévenin F., 2015, *A&A*, **582**, A49
- Kervella P., Arenou F., Mignard F., Thévenin F., 2019, *A&A*, **623**, A72
- Kim B., An D., Stauffer J. R., Lee Y. S., Terndrup D. M., Johnson J. A., 2016, *ApJS*, **222**, 19
- Klose J. Z., Fuhr J. R., Wiese W. L., 2002, *Journal of Physical and Chemical Reference Data*, **31**, 217
- Kovtyukh V. V., Soubiran C., Belik S. I., 2004, *A&A*, **427**, 933
- Kurucz R. L., Furenlid I., Brault J., Testerman L., 1984, *Solar flux atlas from 296 to 1300 nm*
- Lawler J. E., Den Hartog E. A., Sneden C., Cowan J. J., 2006, *ApJS*, **162**, 227
- Lawler J. E., Sneden C., Cowan J. J., Ivans I. I., Den Hartog E. A., 2009, *ApJS*, **182**, 51
- Lawler J. E., Guzman A., Wood M. P., Sneden C., Cowan J. J., 2013, *ApJS*, **205**, 11
- Lawler J. E., Wood M. P., Den Hartog E. A., Feigensohn T., Sneden C., Cowan J. J., 2014, *ApJS*, **215**, 20
- Lawler J. E., Sneden C., Cowan J. J., 2015, *ApJS*, **220**, 13
- Lawler J. E., Sneden C., Nave G., Den Hartog E. A., Emrahođlu N., Cowan J. J., 2017, *ApJS*, **228**, 10
- Lawler J. E., Hala Sneden C., Nave G., Wood M. P., Cowan J. J., 2019, *ApJS*, **241**, 21
- Lee Y. S., et al., 2011, *AJ*, **141**, 90
- Luck R. E., 2017, *AJ*, **153**, 21
- Ludwig H.-G., Freytag B., Steffen M., 1999, *A&A*, **346**, 111
- Magic Z., Weiss A., Asplund M., 2015, *A&A*, **573**, A89
- Martell S. L., et al., 2017, *MNRAS*, **465**, 3203
- Masana E., Jordi C., Ribas I., 2006, *A&A*, **450**, 735
- Meléndez J., Barbuy B., 2009, *A&A*, **497**, 611
- Mishenina T. V., Soubiran C., Kovtyukh V. V., Korotin S. A., 2004, *A&A*, **418**, 551
- Mishenina T. V., Gorbaneva T. I., Basak N. Y., Soubiran C., Kovtyukh V. V., 2011, *Astronomy Reports*, **55**, 689
- Mishenina T. V., Pignatari M., Korotin S. A., Soubiran C., Charbonnel C., Thielemann F. K., Gorbaneva T. I., Basak N. Y., 2013, *A&A*, **552**, A128
- Mishenina T., Gorbaneva T., Pignatari M., Thielemann F. K., Korotin S. A., 2015, *MNRAS*, **454**, 1585
- Molaro P., Monai S., 2012, *A&A*, **544**, A125
- Moore C. E., Minnaert M. G. J., Houtgast J., 1966, *The solar spectrum 2935 Å to 8770 Å*
- Pagel B. E. J., Patchett B. E., 1975, *MNRAS*, **172**, 13
- Pehlivan Rhodin A., Hartman H., Nilsson H., Jönsson P., 2017, *A&A*, **598**, A102
- Petit P., Louge T., Théado S., Paletou F., Manset N., Morin J., Marsden S. C., Jeffers S. V., 2014, *PASP*, **126**, 469
- Placco V. M., et al., 2021, *ApJ*, **912**, L32
- Rebolo R., Molaro P., Beckman J. E., 1988, *A&A*, **192**, 192
- Rice M., Brewer J. M., 2020, *ApJ*, **898**, 119
- Shi J. R., Gehren T., Zhao G., 2011, *A&A*, **534**, A103
- Sneden C. A., 1973, PhD thesis, University of Texas, Austin
- Song N., Alexeeva S., Sitnova T., Wang L., Grupp F., Zhao G., 2020, *A&A*, **635**, A176
- Soubiran C., Girard P., 2005, *A&A*, **438**, 139
- Soubiran C., Bienaymé O., Siebert A., 2003, *A&A*, **398**, 141

- Sozzetti A., Torres G., Latham D. W., Stefanik R. P., Korzennik S. G., Boss A. P., Carney B. W., Laird J. B., 2009, [ApJ](#), **697**, 544
- Steinmetz M., et al., 2006, [AJ](#), **132**, 1645
- Takeda Y., 2023, [Acta Astron.](#), **73**, 35
- Takeda Y., Zhao G., Takada-Hidai M., Chen Y.-Q., Saito Y.-J., Zhang H.-W., 2003, [Chinese J. Astron. Astrophys.](#), **3**, 316
- Takeda Y., Kawanomoto S., Honda S., Ando H., Sakurai T., 2007, [A&A](#), **468**, 663
- Valenti J. A., Fischer D. A., 2005, [ApJS](#), **159**, 141
- Yanny B., et al., 2009, [AJ](#), **137**, 4377
- Zhao G., Zhao Y.-H., Chu Y.-Q., Jing Y.-P., Deng L.-C., 2012, [Research in Astronomy and Astrophysics](#), **12**, 723
- Şahin T., 2017, [Turkish Journal of Physics](#), **41**, 367
- Şahin T., Bilir S., 2020, [ApJ](#), **899**, 41
- Şahin T., Lambert D. L., 2009, [MNRAS](#), **398**, 1730
- Şahin T., Lambert D. L., Klochkova V. G., Tavganskaya N. S., 2011, [MNRAS](#), **410**, 612
- Şahin T., Lambert D. L., Klochkova V. G., Panchuk V. E., 2016, [MNRAS](#), **461**, 4071

Comprehensive Analysis of the Open Cluster Collinder 74

T. Yontan^{1*} , and R. Canbay² 

¹Istanbul University, Faculty of Science, Department of Astronomy and Space Sciences, 34119, Beyazit, Istanbul, Turkiye

²Istanbul University, Institute of Graduate Studies in Science, Programme of Astronomy and Space Sciences, 34116, Beyazit, Istanbul, Turkiye

ABSTRACT

In this study, we have used the *Gaia* Third Data Release (*Gaia* DR3) to investigate an intermediate-age open cluster Collinder 74. We have identified 102 probable cluster members by considering stars with a membership probability exceeding 0.5 and located within the designated confinement radius. The mean proper-motion components of Collinder 74 are estimated as $(\mu_\alpha \cos \delta, \mu_\delta) = (0.960 \pm 0.005, -1.526 \pm 0.004)$ mas yr⁻¹. We detected previously confirmed four blue straggler stars which show flat radial distribution. Colour excess, distance, and age of the cluster were estimated simultaneously by fitting PARSEC isochrones to the observational data on *Gaia* based colour magnitude diagram. These values were derived as $E(G_{BP} - G_{RP}) = 0.425 \pm 0.046$ mag, $d = 2831 \pm 118$ pc and $t = 1800 \pm 200$ Myr, respectively. The mass function slope was estimated as $\Gamma = 1.34 \pm 0.21$ within the mass range $0.65 \leq M/M_\odot \leq 1.58$ which is well matched with that of Salpeter. Stellar mass distribution indicated that the massive and most likely stars are concentrated around the cluster center. The total mass of the cluster was found to be $365 M/M_\odot$ for the stars with probabilities $P > 0$. Galactic orbit integration shows that the Collinder 74 follows a boxy pattern outside the solar circle and is a member of the thin-disc component of the Galaxy.

Keywords: Galaxy: open clusters and associations; individual: Collinder 74; stars: Hertzsprung Russell (HR) diagram; Galaxy: Stellar kinematics

1. INTRODUCTION

Open star clusters (OCs), also known as Galactic clusters, are loosely bound groups of stars that emerged from the same molecular cloud, sharing a common origin and age. As relatively young and dynamically active systems, OCs typically contain hundreds to thousands of stars that share similar chemical composition, age, and distance. The formation origin of OCs plays a crucial role in our understanding of stellar formation and evolution and makes them ideal laboratories for studying stellar properties, such as temperature, luminosity, and mass (Lada & Lada 2003; Kim et al. 2017). Also, member stars of OCs have similar movement directions in the sky, this knowledge makes proper-motion components useful tools for separating physical members from the field star contamination (Sariya et al. 2021). This method provides a reliable sample of member stars for the estimation of astrophysical parameters for OCs (Bisht et al. 2020; Sariya et al. 2021).

In this study, we estimated the structural, kinematic, and astrophysical properties of Collinder 74 (Coll 74) open cluster. The cluster is positioned at $\alpha = 05^h48^m40^s.8$, $\delta = +07^\circ22'26''.4$ (J2000) corresponding to Galactic coordinates $l = 199^\circ.019$, $b = -10^\circ.379$ according to Cantat-Gaudin et al. (2020). Coll 74 is a centrally concentrated old open cluster

located in the third Galactic quadrant toward the Galactic anti-center region. Ann et al. (1999) afforded *UBVI* CCD photometry and suggested that the age of the cluster is 1300 ± 200 Myr and it is located at 2511 ± 245 pc from the Sun. Tadross (2001) performed *UBV* CCD observations and defined colour excess, distance and age of the cluster as $E(B - V) = 0.38$ mag, $d = 2254$ pc and $t = 1600$ Myr, respectively. Dias et al. (2006) presented the kinematics of the cluster using UCAC2 Catalogue positions and proper motions. They derived proper-motion components as $(\mu_\alpha \cos \delta, \mu_\delta) = (-0.49, -3.49)$ mas yr⁻¹. Carraro & Costa (2007) investigated CCD photometry in the *V* and *I*-bands and obtained colour excess, distance and age of the cluster as $E(B - V) = 0.28 \pm 0.04$ mag, $d = 1500$ pc and $t = 3000$ Myr, respectively. From the analyses of *BVI* photometry Hasegawa et al. (2008) concluded that the Coll 74 is 3680 pc away from the Sun and 1400 Myr old cluster. Dias et al. (2014) derived the mean proper-motion components by taking into account the U.S. Naval Observatory CCD Astrograph Catalogue (UCAC4; Zacharias et al. 2013) as $(\mu_\alpha \cos \delta, \mu_\delta) = (1.92 \pm 0.55, -3.00 \pm 0.10)$ mas yr⁻¹. Loktin & Popova (2017) redetermined main parameters using published photometric measurements provided by 2MASS catalogue for 959 clusters including Coll 74. They estimated colour excess, distance and age as $E(B - V) = 0.418$

Corresponding Author: T. Yontan E-mail: talar.yontan@istanbul.edu.tr

Submitted: 29.09.2023 • Revision Requested: 18.10.2023 • Last Revision Received: 19.10.2023 • Accepted: 20.10.2023



This article is licensed under a Creative Commons Attribution-NonCommercial 4.0 International License (CC BY-NC 4.0)

Table 1. Basic parameters of the Collinder 74 open cluster collected from the literature.

$E(B - V)$ (mag)	μ_V (mag)	d (pc)	[Fe/H] (dex)	t (Myr)	$\langle \mu_\alpha \cos \delta \rangle$ (mas yr ⁻¹)	$\langle \mu_\delta \rangle$ (mas yr ⁻¹)	V_γ (km s ⁻¹)	Ref
0.38±0.04	13.08±0.25	2511±245	0.07	1300±200	–	–	–	(01)
0.38	13.00	2254	0.054	1600	–	–	–	(02)
0.38	13.21	2549	–	1300	–	–	–	(03)
–	–	–	–	–	-0.49	-3.49	–	(04)
0.28±0.04	11.75±0.10	1500	–	3000	–	–	–	(05)
0.36	13.95	3680	-0.38	1400	–	–	–	(06)
0.604	13.98	2637	–	1230	0.91	-3.86	–	(07)
–	–	–	–	–	1.92±0.55	-3.00±0.10	–	(08)
–	–	2510	0.050	1288	–	–	–	(09)
0.418	12.588	3293	–	1400	0.294±0.181	-1.091±0.172	–	(10)
–	–	–	–	–	0.77±2.15	0.47±3.54	–	(11)
–	–	2453 ⁺⁷⁹⁷ ₋₄₈₄	–	–	1.011±0.016	-1.512±0.016	–	(12)
–	–	2453 ⁺⁷⁹⁷ ₋₄₈₄	–	–	1.011±0.016	-1.512±0.016	20.18±0.39	(13)
–	–	2747±332	–	2190±131	0.981±0.200	-1.497±0.199	–	(14)
–	–	2453 ⁺⁷⁹⁷ ₋₄₈₄	-0.05±0.03	–	1.011±0.121	-1.512±0.122	15.94±17.57	(15)
0.274	11.99	2498±494	–	1900	1.011±0.121	-1.512±0.122	–	(16)
0.391±0.076	–	2153±144	-0.083±0.084	2760	0.995±0.170	-1.528±0.175	20.20±0.80	(17)
–	–	2356	–	2100	1.011±0.121	-1.512±0.122	20.18±0.39	(18)
0.511±0.074	–	2466±22	–	627±348	0.964±0.007	-1.546±0.007	20.93±4.10	(19)
0.301±0.033	13.052±0.088	2831±118	0.052±0.034	1800±200	0.960±0.005	-1.526±0.004	20.55±0.41	(20)

(01) Ann et al. (1999), (02) Tadross (2001), (03) Lata et al. (2002), (04) Dias et al. (2006), (05) Carraro & Costa (2007), (06) Hasegawa et al. (2008), (07) Kharchenko et al. (2013), (08) Dias et al. (2014), (09) Marsakov et al. (2016), (10) Loktin & Popova (2017), (11) Dias et al. (2018), (12) Cantat-Gaudin et al. (2018), (13) Soubiran et al. (2018), (14) Liu & Pang (2019), (15) Zhong et al. (2020), (16) Cantat-Gaudin et al. (2020), (17) Dias et al. (2021), (18) Tarricq et al. (2021), (19) Hunt & Reffert (2023), (20) This study

mag, $d = 3293$ pc and $t = 1400$ Myr, respectively. Also, from RAVE catalogue Loktin & Popova (2017) estimated proper-motion components in equatorial coordinate system as $(\mu_\alpha \cos \delta, \mu_\delta) = (0.294 \pm 0.181, -1.091 \pm 0.172)$ mas yr⁻¹, respectively.

With the first data release of the *Gaia* (Gaia Collaboration et al. 2016), many researchers investigated the astrometric and kinematic properties of the Coll 74. According to literature studies performed with *Gaia* data, values of the mean radial velocity of the cluster differs from 15.94 ± 17.57 km s⁻¹ (Zhong et al. 2020) to 20.20 ± 0.80 km s⁻¹ (Dias et al. 2021) and distance to the Sun changes between 1500 pc (Carraro & Costa 2007) and 3680 pc (Hasegawa et al. 2008). Also, the age of the cluster varies from 1230 Myr (Kharchenko et al. 2013) to 3000 Myr (Carraro & Costa 2007). The literature results are listed in Table 1 for detailed comparison. The main purpose of this study is to find out structural, astrophysical, and kinematic properties of the Coll 74 open cluster.

2. DATA

The astrometric, photometric, and spectroscopic data for Coll 74 open cluster was taken from *Gaia*'s third data release (*Gaia* DR3, Gaia Collaboration et al. 2023). To do this, we used the central equatorial coordinates of Cantat-Gaudin et al. (2020) $\langle \alpha, \delta \rangle = (05^h 48^m 40^s.8, +07^\circ 22' 26''.4)$ and compiled the detected stars in the direction of the cluster for $35'$ -radius field. Hence, we identified 73,326 stars within the applied radius. The

finding chart of the Coll 74 ($35' \times 35'$) is shown in Figure 1. The main cluster catalogue contains each stars' position (α, δ), photometric magnitude and colour index ($G, G_{BP} - G_{RP}$), trigonometric parallax (ϖ), proper-motion components ($\mu_\alpha \cos \delta, \mu_\delta$), radial velocity (V_γ) and their errors within the $8 < G \leq 22$ mag.

To achieve reliable structural and astrophysical parameters for Coll 74, we obtained a faint limited magnitude of the used data. For this, we calculated the number of stars that correspond to the G magnitude intervals. The histogram of a number of stars versus G magnitudes is shown in Figure 2, where a number of stars rise towards the fainter G magnitudes and declines after a certain limit. This limit value is $G = 20.5$ mag for the Coll 74 and in the following analyses, we used only the stars brighter than $G = 20.5$ mag. We calculated the mean photometric errors of the stars for G magnitude intervals. The mean errors for G and $G_{BP} - G_{RP}$ colour indices reach up 0.011 and 0.228 mag for $G = 20.5$ limiting magnitude, respectively. The photometric errors for G magnitudes and $G_{BP} - G_{RP}$ colour indices versus G magnitude intervals are shown in Figure 3.

3. RESULTS

3.1. Spatial structure of Collinder 74

To interpret stellar distribution within the cluster we constructed the radial density profile (RDP) considering adopted central equatorial coordinates presented by Cantat-Gaudin et al. (2020). We divided the $35'$ cluster region into many concentric rings surrounding the cluster center and calculated stellar

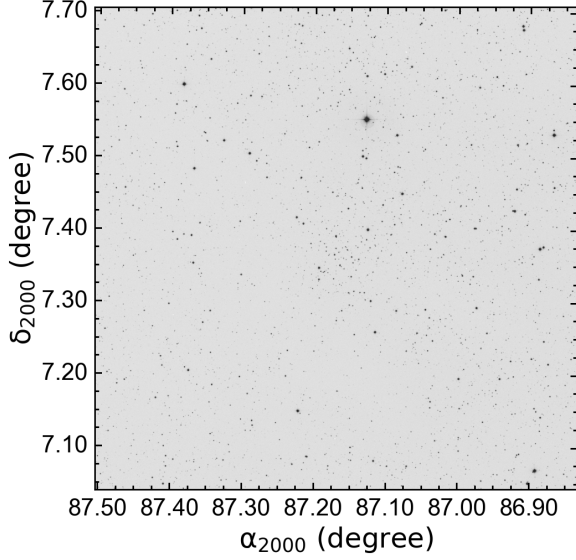


Figure 1. Finding chart of the Coll 74 for $35' \times 35'$ region. Up and left directions represent North and East, respectively.

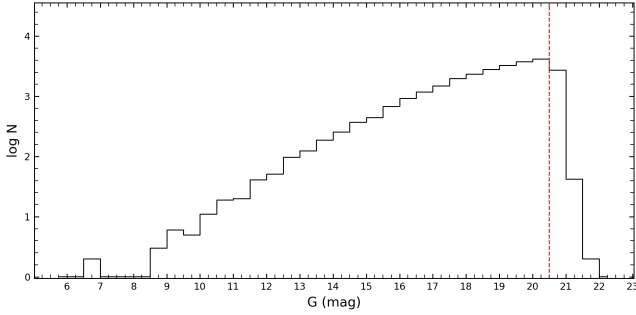


Figure 2. Distribution of the stars in the direction of Coll 74 for G magnitude intervals. The photometric completeness limit is indicated by a red dashed line.

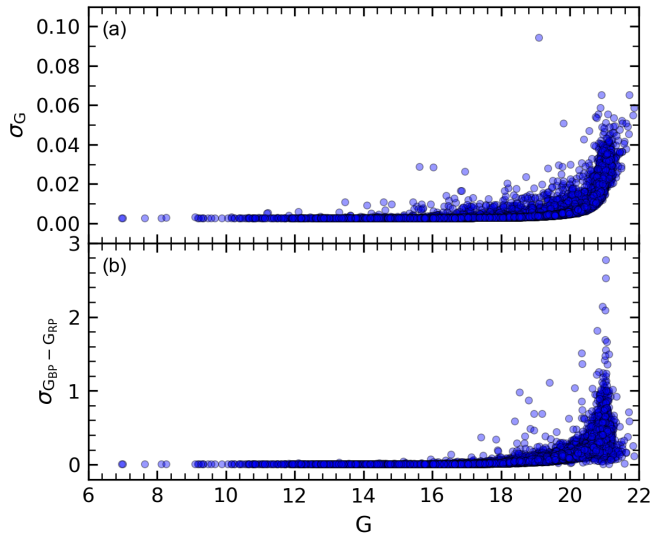


Figure 3. Distribution of mean photometric errors obtained for G apparent magnitude (a) and $G_{BP} - G_{RP}$ colour index versus G magnitude intervals.

densities ($\rho(r)$) from the stars within $G \leq 20.5$ mag. The stellar densities in i^{th} ring were calculated by the equation of

$R_i = N_i/A_i$, where, N_i and A_i indicate the number of stars and area of related ring, respectively. To visualise RDP, we plotted stellar density distribution versus distance from cluster center and fitted the empirical King (1962) model identified by the following equation:

$$\rho(r) = f_{bg} + \frac{f_0}{1 + (r/r_c)^2}. \quad (1)$$

Here, r is the radius of the cluster. The f_{bg} , f_0 , r_c are the background stellar density, the central stellar density and the core radius, respectively. We used the minimum χ^2 estimation for RDP analyses and estimated f_{bg} , f_0 and r_c . In Figure 4 we showed the best-fit result of RDP which is demonstrated by the black solid line. It can be seen from the figure that stellar density is higher near the cluster center and it flattens toward the outer region of the cluster and at a point merges with the field star density. This point is described as limiting radius (r_{lim}) and visually adopted as $10'$. The best-fit solution of RDP analyses resulted that the structural parameters to be $f_0 = 8.42 \pm 0.35$ stars arcmin $^{-2}$, $f_{bg} = 5.45 \pm 0.16$ stars arcmin $^{-2}$ and $r_c = 1.38 \pm 0.12$ arcmin for the Coll 74.

3.2. Membership Analyses of Collinder 74

Working with a sample of stars that are part of the cluster itself is crucial to accurately characterise its properties, such as its age, mass, luminosity function, and dynamics. Field star contamination may contribute to noise and bias during the analyses and can cause inaccurate results. Therefore, field star separation is necessary to understand the astrophysical, astrometric, and kinematic properties of the studied cluster. As their physical formation processes, cluster members are gravitationally

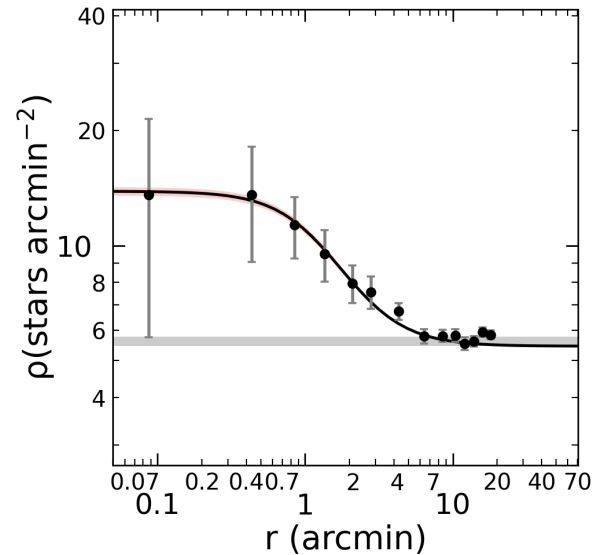


Figure 4. The RDP of King (1962) for Coll 74. Stellar density errors were determined from Poisson statistics $1/\sqrt{N}$, where N is the number of stars. The fitted black curve and horizontal grey shaded area show the best-fitted RDP and background stellar density, respectively. Also, red-shaded area indicates the 1σ uncertainty of the fit.

bound to the cluster. Therefore, they exhibit similar vectorial movements across the sky relative to the background field stars. By analyzing proper-motion components, it becomes possible to identify stars that share the cluster's motion characteristics as potential cluster members. Hence, proper-motion components are useful tools to separate cluster members and calculate their membership probabilities (Sariya et al. 2021; Bisht et al. 2020). The precise astrometric data from *Gaia* DR3 data (Gaia Collaboration et al. 2023) provide a crucial role for membership analyses.

We used the method of Photometric Membership Assignment in Stellar Clusters (UPMASK, Krone-Martins & Moitinho 2014) considering *Gaia* DR3 astrometric data to calculate membership probabilities of stars in the region of the Coll 74. UPMASK uses a clustering algorithm to group stars that have similar positions, proper-motion components, trigonometric parallaxes and are close to each other in space. The algorithm then assigns membership probabilities to each star based on its likelihood of belonging to a particular cluster. We utilised the method in five-dimensional astrometric space considering astrometric measurements (α , δ , $\mu_\alpha \cos \delta$, μ_δ , ϖ), also their uncertainties, of each star. To determine the membership possibilities (P) of stars we run the program with 100 iterations. As a result, taking into account the stars within both the estimated limiting radius ($r_{\text{lim}}=10'$) and the completeness limit $G = 20.5$ mag, for the open cluster Coll 74 we obtained 102 most likely member stars with membership probabilities of $P \geq 0.5$. These stars are used in the estimation of astrometric and astrophysical parameters of Coll 74.

To visualise the clustering of the most likely member stars, we plotted vector-point diagram (VPD) by using proper-motion components of the stars and showed it in Figure 5. It is evident from the VPD that Coll 74 is embedded in the field stars. Even if this is the case, the cluster structure can be distinguished by investigating the probability values of the stars. We estimated mean proper-motion values from the stars with membership probabilities greater than 0.5 and found the values as $(\mu_\alpha \cos \delta, \mu_\delta) = (0.960 \pm 0.005, -1.526 \pm 0.004)$ mas yr $^{-1}$. The trigonometric parallax histogram of the most likely member stars is shown in Figure 6. By fitting the Gaussian function to the histogram, we estimated the mean trigonometric parallax as $\varpi = 0.363 \pm 0.043$ mas for the Coll 74 and corresponding distance value (with the linear equation $d(\text{pc}) = 1000/\varpi$) mas as $d_\varpi = 2755 \pm 326$ pc. This distance value is close to the values estimated in *Gaia* era, as listed in Table 1.

3.3. The Blue Straggler Stars of Collinder 74

Blue straggler stars (BSSs) in open clusters defy the natural aging process by appearing younger and bluer than their surrounding companions. While most stars in open clusters follow common evolutionary processes, BSSs defy the laws of stellar evolution in the cluster by reversing this trend. Interactions

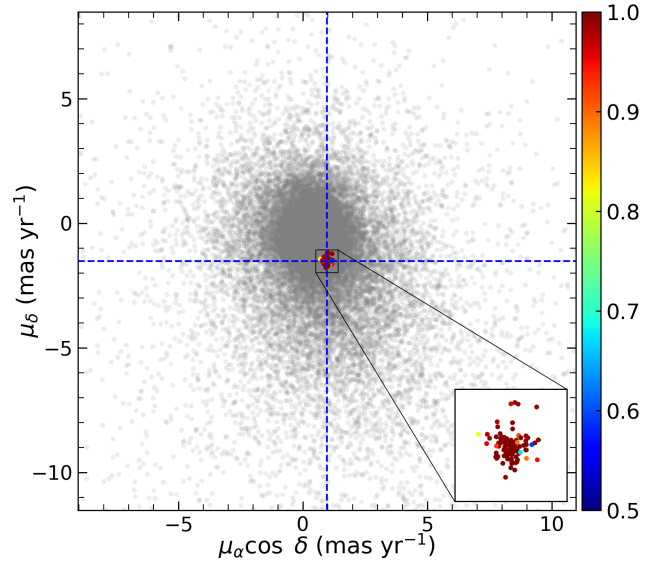


Figure 5. VPD of Coll 74. The colour scale on the right panel indicates the membership probabilities of the stars for the cluster. The enlarged panel inset shows the cluster's denser region in VPD. The intersection of the dashed blue lines represents the mean proper-motion value for Coll 74.

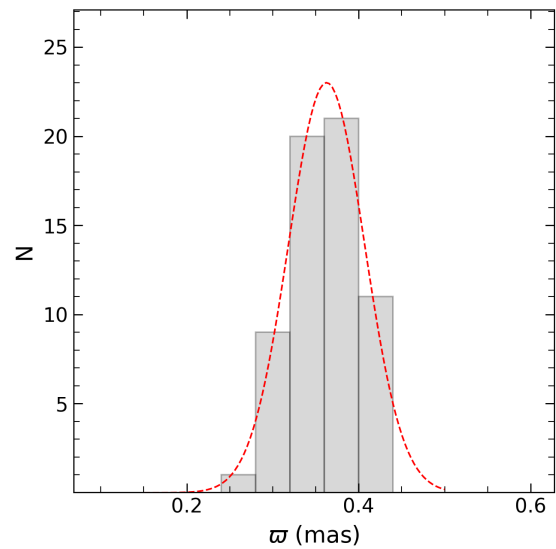


Figure 6. Histogram of star count of the most likely members ($P \geq 0.5$) in trigonometric parallaxes. The red dashed line indicates the fitted Gaussian function.

between stars in binary systems or stellar collisions within the dense cluster environment are among the leading formation mechanisms for BSSs (Sandage 1953; Zinn & Dahn 1976; Hills & Day 1976).

We identified four BSSs in Coll 74. These stars are confirmed as cluster members with membership probabilities $P \geq 0.9$. The positions of BSSs are shown in Figure 7. Rain et al. (2021) defined five BSSs by using *Gaia* DR2 (Gaia Collaboration et al. 2018) photometric and astrometric data. Due to the membership analyses being based on *Gaia* DR3 data and we took into account the stars within limiting radius ($r_{\text{lim}} \leq 10'$),

one of the Rain et al. (2021) BSS was not considered. Jadhav & Subramaniam (2021) using *Gaia* DR2 data and identified BSSs in 1246 open clusters. They found four BSSs members in Coll 74 which are the same star sample as presented in this study.

Ferraro et al. (2012) considering the radial distribution of BSSs in the clusters, defined three classes for BSSs. Three of BSSs in Coll 74 are located at a radial distances of 0.42, 0.88, and 0.98 arcmin, whereas one star is located at 6.25 arcmin. According to their radial distribution and the criterion of Ferraro et al. (2012), we can conclude that the BSSs of Coll 74 show flat distribution and cluster belongs to the family I. The formation mechanisms of blue stragglers in family I clusters are thought dominantly to be caused by stellar collisions and mass transfer in close binary systems.

3.4. Astrophysical Parameters of Collinder 74

To derive age, distance modulus and colour excess of Coll 74, we fitted theoretical PARSEC isochrones of Bressan et al. (2012) to the observed CMD constructed from the most likely cluster members. The age, distance modulus and colour excess of the cluster were estimated simultaneously, while the metallicity of Coll 74 was taken from Zhong et al. (2020) as $[\text{Fe}/\text{H}] = -0.052 \pm 0.034$ dex. We fitted PARSEC models by taking into account the morphology of the cluster and reached the best fit. For the selection of the isochrones and estimation of astrophysical parameters, we transformed the assumed metallicity ($[\text{Fe}/\text{H}] = -0.052 \pm 0.034$ dex) to the mass fraction z . To do this, we applied the equation of Bovy¹ that are available for PARSEC models (Bressan et al. 2012). The equations are given as follows:

$$z_x = 10^{[\text{Fe}/\text{H}] + \log\left(\frac{z_\odot}{1 - 0.248 - 2.78 \times z_\odot}\right)}, \quad (2)$$

and

$$z = \frac{(z_x - 0.2485 \times z_x)}{(2.78 \times z_x + 1)}. \quad (3)$$

where z_x and z_\odot are intermediate values where solar metallicity z_\odot was adopted as 0.0152 (Bressan et al. 2012). The calculated mass fraction is $z = 0.0136$ for Coll 74.

We plotted $G \times (G_{\text{BP}} - G_{\text{RP}})$ and superimposed isochrones, scaled to the $z = 0.0136$, of different ages ($\log t = 9.20, 9.25$ and 9.30 yr) by visual inspection to the most likely cluster main-sequence, turn-off and giant members with probabilities over $P \geq 0.5$ as shown in Figure 7. The best fit supports the isochrone with $\log t = 9.25$ yr to the cluster morphology, this isochrone corresponding to $t = 1800 \pm 200$ Myr. The estimated age is comparable with the values of Tadross (2001) and Cantat-Gaudin et al. (2020). Also, good isochrone fitting result supplies the distance modulus and colour excess of the Coll 74

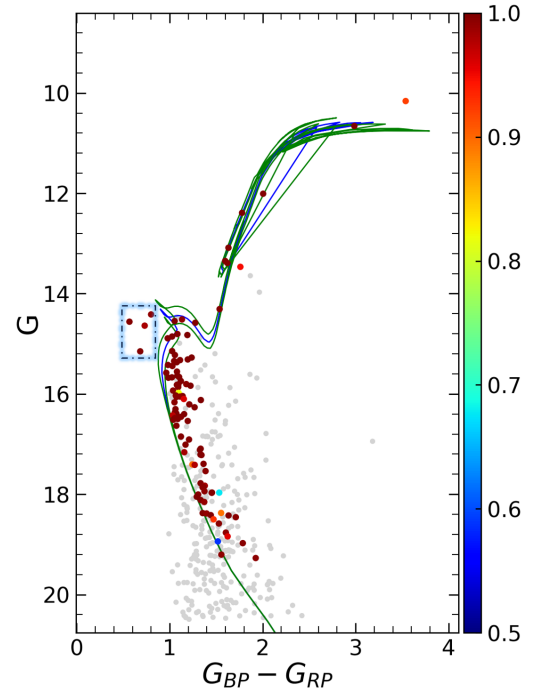


Figure 7. Colour-magnitude diagram for the studied cluster Coll 74. Different colour and colourbar scales show the membership probabilities of stars with $P \geq 0.5$. Stars with probabilities $P < 0.5$ are demonstrated with filled grey circles. BSSs of the cluster are shown in a blue dashed-lined box. The best solution of fitted isochrones and their errors are inferred as the blue and green lines, respectively. The age of the blue-lined isochrone matches 1800 Myr for the cluster.

to be $\mu_G = 13.052 \pm 0.088$ mag, corresponding to isochrone distance $d_{\text{iso}} = 2831 \pm 118$ pc and $E(G_{\text{BP}} - G_{\text{RP}}) = 0.425 \pm 0.046$ mag, respectively. We used the relations of Carraro et al. (2017) to estimate the errors of distance modulus and isochrone distance. Our derived isochrone distance is compatible with most of the studies presented by different researchers (see Table 1) as well as the trigonometric parallax distance, $d_\pi = 2755 \pm 326$ pc, estimated in this study. For a more accurate comparison with literature studies, we converted this value to the *UBV*-based colour excess $E(B - V)$. We utilised the equation $E(G_{\text{BP}} - G_{\text{RP}}) = 1.41 \times E(B - V)$ given by Sun et al. (2021) and determined the value as $E(B - V) = 0.301 \pm 0.033$ mag. This result is close to the values given by Tadross (2001), Lata et al. (2002), Carraro & Costa (2007) and Hasegawa et al. (2008) within the errors (see Table 1).

We also estimated heliocentric Galactic coordinates $(X, Y, Z)_\odot$ of Coll 74. Here, X is the distance from the Galactic center in the Galactic plane ($l = 0^\circ, b = 0^\circ$), Y is the distance in the direction of Galactic rotation ($l = 90^\circ, b = 0^\circ$) and Z is the vertical distance from Galactic plane to the North Galactic Pole ($l = 0^\circ, b = 90^\circ$). Galactocentric coordinates provide a convenient way to describe the positions of celestial objects relative to the Galactic center, Sun, and Galactic plane. By considering isochrone distance, Galactic longitude, and latitude of the cluster, we derived these distances as $(X, Y, Z)_\odot = (-2633, -907, -510)$ pc.

¹ <https://github.com/jobovy/isodist/blob/master/isodist/Isochrone.py>

4. GALACTIC ORBIT STUDY OF THE COLLINDER 74

The Galactic orbits of open clusters are important for understanding how these celestial objects dynamically evolve within the Milky Way (Taşdemir & Yontan 2023). We derived the orbits and orbital parameters of Coll 74 with the help of the python based Galactic dynamics library GALPY² of Bovy (2015). This library implements MWPOTENTIAL2014 model, which commonly uses a potential model in Galactic dynamics. The MWPOTENTIAL2014 model is based on a combination of different components that represent the various structures within the Milky Way, including the bulge, disc, and halo. These components are parameterised to approximate the observed properties of the Galaxy: the bulge is modelled as a power-law density profile as described in Bovy (2015), the disc is typically modelled as an exponential disk with a specified scale length and scale height as defined by Miyamoto & Nagai (1975) and the halo is often modelled as a spherical or ellipsoidal distribution with a specified density profile as defined by Navarro et al. (1996). We accepted Sun's Galactocentric distance and orbital velocity as $R_{gc} = 8$ kpc and $V_{rot} = 220$ km s⁻¹, respectively (Bovy 2015; Bovy & Tremaine 2012), as well as Sun's distance from the Galactic plane was adopted as 25 ± 5 pc (Jurić et al. 2008).

The mean radial velocity (V_γ) of the cluster was calculated from available *Gaia* DR3 radial velocity measurements of the stars. We considered the most likely member stars with probabilities over $P \geq 0.5$ whose number are 16. We used the equations of Soubiran et al. (2018) which are based on the weighted average of the radial velocities of the stars. Hence, the mean radial velocity of the Coll 74 was determined as $V_\gamma = 20.55 \pm 0.41$ km s⁻¹ which is in good agreement with mean radial velocity findings presented by Soubiran et al. (2018), Dias et al. (2021), Tarricq et al. (2021) and Hunt & Reffert (2023). To estimate orbital parameters, we used equatorial coordinates ($\alpha = 05^h48^m40^s.8$, $\delta = +07^\circ22'26''.4$) taken from Cantat-Gaudin et al. (2020), mean proper-motion components ($\mu_\alpha \cos \delta = 0.960 \pm 0.005$, $\mu_\delta = -1.526 \pm 0.004$ mas yr⁻¹), isochrone distance ($d_{iso} = 2831 \pm 118$ pc) and the radial velocity ($V_\gamma = 20.55 \pm 0.41$ km s⁻¹) calculated in the study (see also Table 2) for Coll 74 as input parameters.

The orbit integration was applied for the forward with an integration step of 1 Myr up to 2.5 Gyr to estimate the possible current position of Coll 74. The resultant orbit is shown in Figure 8a. The figure pictures the path followed by the cluster in $Z \times R_{gc}$ plane, which represents the side view of the orbit. Here, Z and R_{gc} are the distance from the Galactic plane and the Galactic center, respectively. Also, the orbit analyses were carried out for the past epoch across a time equal to $t = 1800 \pm 200$ Myr of the cluster's age. Figure 8b shows the cluster's distance variation in time on the $R_{gc} \times t$ plane. The figure also

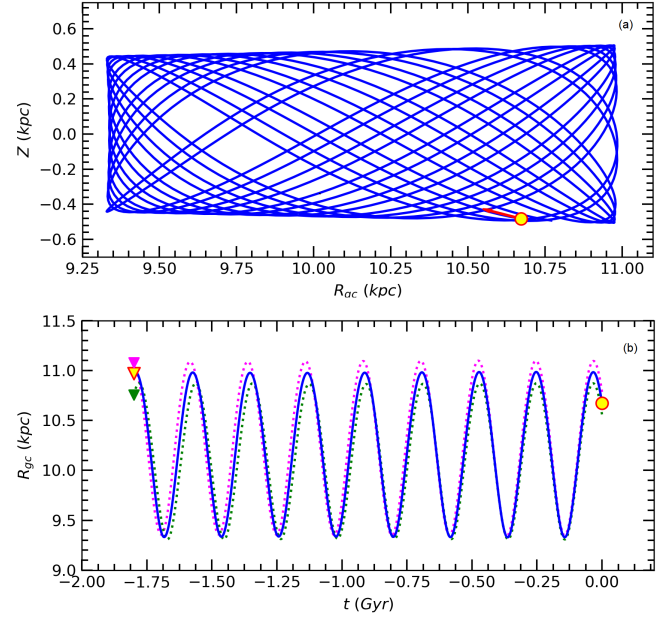


Figure 8. The Galactic orbits and birth radii of Coll 74 in the $Z \times R_{gc}$ (a) and $R_{gc} \times t$ (b) planes. The filled yellow circles and triangles show the present-day and birth positions, respectively. The red arrow is the motion vector of Coll 74. The green and pink dotted lines show the orbit when errors in input parameters are considered, while the green and pink filled triangles represent the birth locations of the open cluster based on the lower and upper error estimates.

represents the influence of errors in the input parameters on the orbit of Coll 74. Orbit analyses stated that the Coll 74 was formed outside the solar vicinity with a birth radius of $R_{gc} = 10.97 \pm 0.32$ kpc.

From the orbit integration we derived the following parameters for Coll 74: apogalactic ($R_a = 10987 \pm 112$ pc) and perigalactic ($R_p = 9337 \pm 20$ pc) distances, eccentricity ($e = 0.081 \pm 0.004$), maximum vertical distance from Galactic plane ($Z_{max} = 506 \pm 22$ pc), space velocity components ($U, V, W = -11.43 \pm 0.79, -29.50 \pm 1.08, -2.56 \pm 0.05$ km s⁻¹), and orbital period ($P_{orb} = 291 \pm 2$ Myr). The Local Standard of Rest (LSR) correction was applied to the (U, V, W) components of the Coll 74. To do this, we considered the space velocity component values (U, V, W)_⊙ = (8.83 ± 0.24, 14.19 ± 0.34, 6.57 ± 0.21) km s⁻¹ of Coşkunoğlu et al. (2011). Hence, LSR corrected space velocity components were found to be (U, V, W)_{LSR} = (-2.60 ± 0.25, -15.31 ± 1.13, 4.01 ± 0.22) km s⁻¹. Total space velocity was estimated as $S_{LSR} = 16.04 \pm 1.18$ km s⁻¹, which is compatible with the velocity value given for thin-disc objects (Leggett 1992). We interpreted from the perigalactic and apogalactic distances that Coll 74 is completely outside the solar circle (Figure 8a). The cluster reaches a maximum distance above the Galactic plane at $Z_{max} = 506 \pm 22$ pc, which shows that Coll 74 belongs to the thin-disc component of the Milky Way (Bilir et al. 2006a,b, 2008).

² See also <https://galpy.readthedocs.io/en/v1.5.0/>

5. LUMINOSITY AND MASS FUNCTIONS

The luminosity function (LF) of an open cluster represents the number of stars at different brightness within the cluster. The LF and mass function (MF) of open clusters are related because the luminosity of a star is generally correlated with its mass. This correlation is also defined as mass-luminosity relation and provides transformation of LF into the MF (Bisht et al. 2019).

For LF analyses of Coll 74, first, we selected the main-sequence stars with membership probabilities $P > 0$ and located inside the limiting radius obtained in the study ($r_{\text{lim}}^{\text{obs}} = 10'$). Hence, we reached 324 stars within the $15 \leq G \leq 20.5$ magnitude interval. Then considering distance modulus ($M_G = G - 5 \times \log d + A_G$) with apparent magnitude (G), isochrone distance (d_{iso}) and G band absorption (A_G) estimated in the study, we transformed apparent G magnitudes into the absolute M_G magnitudes. The histogram of LF for the cluster that constructed an interval of 1 mag is shown in Figure 9. This figure shows that the number of main-sequence stars increases up to $M_G=6$ mag properly, after this limit the counts drop gradually.

For MF estimation, we used PARSEC isochrones (Bressan et al. 2012) that scaled to the derived age and adopted metallicity fraction (z) for the cluster. From this isochrone, we produced a high-degree polynomial equation between the G -band absolute magnitudes and masses. By applying this equation to the selected main-sequence stars ($P > 0$), we transformed their absolute magnitudes M_G into masses. Hence, we found a mass range of the 324 stars within the $0.65 \leq M/M_{\odot} \leq 1.58$. The MF slope was derived from the following equation:

$$\log(dN/dM) = -(1 + \Gamma) \times \log M + C. \quad (4)$$

In the equation dN is the number of stars per unit mass dM , M is the central mass, C denotes the constant for the equation, and Γ represents the slope of the MF. The estimated MF slope for Coll 74 is $\Gamma = 1.34 \pm 0.21$, which is in good agreement with the value of Salpeter (1955). The resulting MF is shown in Figure 10.

The masses of stars in Coll 74 were derived as a function of stars' membership probabilities. The number of stars with probabilities $P > 0$ and $P \geq 0.5$ was determined as 324 and

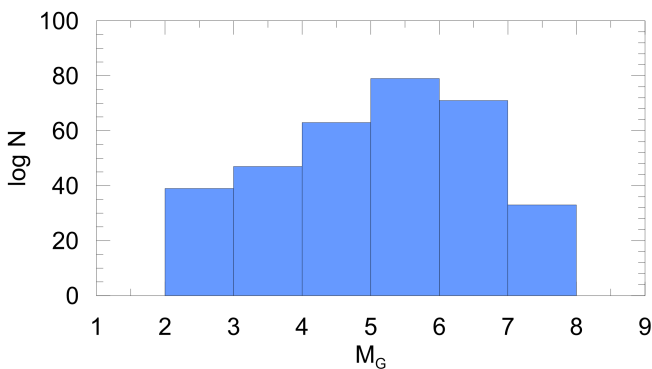


Figure 9. The luminosity function of Coll 74.

102, respectively. Hence, the total mass of the cluster for these probabilities is to be $365M_{\odot}$ and $132M_{\odot}$, respectively. We interpreted that the total mass of the cluster estimated from the stars with probabilities $P \geq 0.5$ corresponds to about 36% of the total mass for the stars with all probabilities. To investigate the mass distribution of the stars in Coll 74, 324 stars with $P > 0$ were plotted according to their equatorial coordinates and membership probabilities as shown in Figure 11. It can be interpreted from the figure that the stars with probabilities over 0.8 and massive ones are mostly concentrated central region of the cluster, whereas low-mass stars with probabilities under 0.8 are distributed beyond the cluster center. This case shows that the Coll 74 is a mass segregated open cluster.

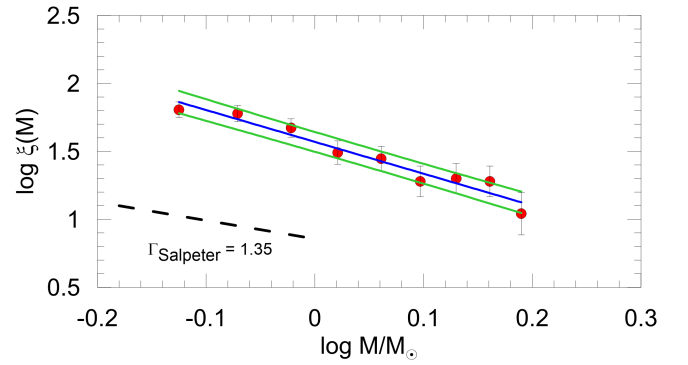


Figure 10. Derived mass function for Coll 74. The blue line represents the MF, whereas the green lines indicate the $\pm 1\sigma$ standard deviations. The black dashed line represented Salpeter (1955)'s slope.

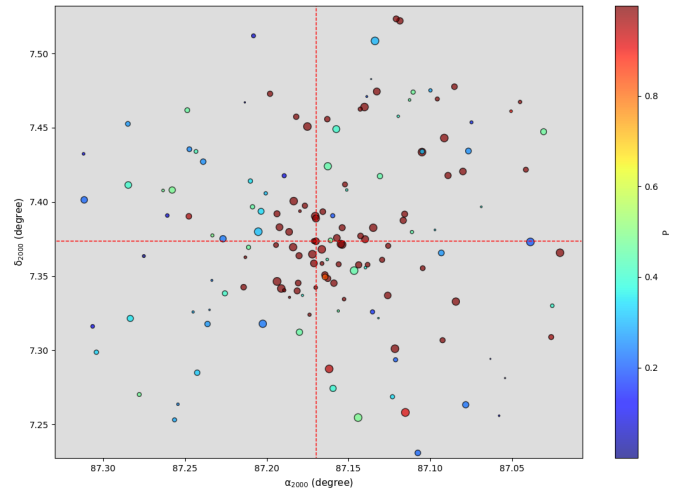


Figure 11. Mass distribution of the stars in the Coll 74. The radius sizes of the stars indicate the masses, and the different colours show the membership probabilities of the stars. The intersection of the red dashed lines indicates the central position of the cluster in the equatorial coordinate system.

6. CONCLUSION

We performed a detailed *Gaia* DR3 data-based study of open cluster Collinder 74. The number of member stars with prob-

abilities over 0.5 were 102. Considering these stars, we calculated structural and fundamental astrophysical parameters, investigated luminosity and mass functions, and estimated the orbit of the cluster. All parameters obtained in the study are listed in Table 2. The main results of the study are summarized as follows:

1. From the RDP analyses, we determined the limiting radius by visual inspection as $r_{\text{lim}}^{\text{obs}} = 10'$.

2. Considering results of photometric completeness limit, membership probability analyses, and limiting radius, we identified 102 most likely members with probabilities $P \geq 0.5$ for Coll 74. These stars were used in the cluster analyses.

3. The mean proper-motion components were obtained as $(\mu_{\alpha} \cos \delta, \mu_{\delta}) = (0.960 \pm 0.005, -1.526 \pm 0.004)$ mas yr⁻¹.

4. Four most probable BSS members were identified within the limiting radius of the cluster. We concluded that the Coll 74 belongs to family I according to the radial distribution of its BSSs.

5. The metallicity value for the cluster was adopted as $[\text{Fe}/\text{H}] = -0.052 \pm 0.034$ dex which is presented by [Zhong et al. \(2020\)](#). We transformed this value into the mass fraction $z = 0.0136$ and kept it as a constant parameter for the age and distance modulus estimation.

6. By fitting PARSEC isochrone ([Bressan et al. 2012](#)) to the G versus $(G_{\text{BP}} - G_{\text{RP}})$ colour-magnitude diagram, we estimated colour excess of the Coll 74 as $E(G_{\text{BP}} - G_{\text{RP}}) = 0.425 \pm 0.046$ mag, which corresponds to a colour excess in UBV system to be $E(B - V) = 0.301 \pm 0.033$ mag. We estimated this value by using the equation $E(G_{\text{BP}} - G_{\text{RP}}) = 1.41 \times E(B - V)$ as given by [Sun et al. \(2021\)](#).

7. The isochrone fitting distance of Coll 74 was determined as $d_{\text{iso}} = 2831 \pm 118$ pc. This value is supported by the distance $d_{\varpi} = 2755 \pm 326$ pc that derived from mean trigonometric parallax.

8. PARSEC isochrone of [Bressan et al. \(2012\)](#) provides the age of the cluster to be $t = 1800 \pm 200$ Myr.

9. The LF and MF were investigated from the main-sequence stars with probabilities $P > 0$. The MF slope was found as $\Gamma = 1.34 \pm 0.21$ which is in good agreement with the value of [Salpeter \(1955\)](#).

10. Orbit integration was performed via MWPOTENTIAL2014 model. We concluded that Coll 74 orbits in a boxy pattern outside the solar circle, as well as the cluster, is a member of the thin-disc component of the Milky Way. Moreover, the birth radius (10.97 ± 0.32 kpc) shows that the forming region of the cluster is outside the solar circle.

Peer Review: Externally peer-reviewed.

Author Contribution: Conception/Design of study - T.Y., R.C.; Data Acquisition - T.Y., R.C.; Data Analysis/Interpretation - T.Y., R.C.; Drafting Manuscript - T.Y.,

Table 2. Fundamental parameters of Coll 74.

Parameter	Value
$(\alpha, \delta)_{\text{J2000}}$ (Sexagesimal)	05:48:40.8, +07:22:26.4
$(l, b)_{\text{J2000}}$ (Decimal)	199.0189, -10.3791
f_0 (stars arcmin ⁻²)	8.42 ± 0.35
f_{bg} (stars arcmin ⁻²)	5.45 ± 0.16
r_c (arcmin)	1.38 ± 0.12
r_{lim} (arcmin)	10
r (pc)	8.24
Cluster members ($P \geq 0.5$)	102
$\mu_{\alpha} \cos \delta$ (mas yr ⁻¹)	0.960 ± 0.005
μ_{δ} (mas yr ⁻¹)	-1.526 ± 0.004
ϖ (mas)	0.363 ± 0.043
d_{ϖ} (pc)	2755 ± 326
$E(B - V)$ (mag)	0.301 ± 0.033
$E(G_{\text{BP}} - G_{\text{RP}})$ (mag)	0.425 ± 0.046
A_G (mag)	0.792 ± 0.086
$[\text{Fe}/\text{H}]$ (dex)*	-0.052 ± 0.034
Age (Myr)	1800 ± 200
Distance modulus (mag)	13.052 ± 0.088
Isochrone distance (pc)	2831 ± 118
$(X, Y, Z)_{\odot}$ (pc)	$(-2633, -907, -510)$
R_{gc} (kpc)	10.67
MF slope	1.34 ± 0.21
Total mass (M/M_{\odot}) ($P > 0$)	365
V_{γ} (km s ⁻¹)	20.55 ± 0.41
U_{LSR} (km s ⁻¹)	-2.60 ± 0.25
V_{LSR} (kms ⁻¹)	-15.31 ± 1.13
W_{LSR} (kms ⁻¹)	4.01 ± 0.22
S_{LSR} (kms ⁻¹)	16.04 ± 1.18
R_a (pc)	10987 ± 112
R_p (pc)	9337 ± 20
z_{max} (pc)	506 ± 22
e	0.081 ± 0.004
P_{orb} (Myr)	291 ± 2
Birthplace (kpc)	10.97 ± 0.32

*[Zhong et al. \(2020\)](#)

R.C.; Critical Revision of Manuscript - T.Y., R.C.; Final Approval and Accountability - T.Y., R.C.

Conflict of Interest: Authors declared no conflict of interest.

Financial Disclosure: This study has been supported in part by the Scientific and Technological Research Council (TÜBİTAK) 122F109

Acknowledgements: This research has made use of the WEBDA database, operated at the Department of Theoretical Physics and Astrophysics of the Masaryk University. We also made use of NASA's Astrophysics Data System as well as

the VizieR and Simbad databases at CDS, Strasbourg, France and data from the European Space Agency (ESA) mission *Gaia*³, processed by the *Gaia* Data Processing and Analysis Consortium (DPAC)⁴. Funding for DPAC has been provided by national institutions, in particular, the institutions participating in the *Gaia* Multilateral Agreement.

LIST OF AUTHOR ORCIDS

T. Yontan <https://orcid.org/0000-0002-5657-6194>

R. Canbay <https://orcid.org/0000-0003-2575-9892>

REFERENCES

- Ann H. B., Lee M. G., Chun M. Y., Kim S. L., Jeon Y. B., Park B. G., 1999, *Journal of Korean Astronomical Society*, 32, 7
- Bilir S., Karaali S., Ak S., Yaz E., Hamzaoglu E., 2006a, *New Astron.*, 12, 234
- Bilir S., Karaali S., Gilmore G., 2006b, *MNRAS*, 366, 1295
- Bilir S., Cabrera-Lavers A., Karaali S., Ak S., Yaz E., López-Corredoira M., 2008, *Publ. Astron. Soc. Australia*, 25, 69
- Bisht D., Yadav R. K. S., Ganesh S., Durgapal A. K., Rangwal G., Fynbo J. P. U., 2019, *MNRAS*, 482, 1471
- Bisht D., Zhu Q., Yadav R. K. S., Durgapal A., Rangwal G., 2020, *MNRAS*, 494, 607
- Bovy J., 2015, *ApJS*, 216, 29
- Bovy J., Tremaine S., 2012, *ApJ*, 756, 89
- Bressan A., Marigo P., Girardi L., Salasnich B., Dal Cero C., Rubele S., Nanni A., 2012, *MNRAS*, 427, 127
- Cantat-Gaudin T., et al., 2018, *A&A*, 618, A93
- Cantat-Gaudin T., et al., 2020, *A&A*, 640, A1
- Carraro G., Costa E., 2007, *A&A*, 464, 573
- Carraro G., Sales Silva J. V., Moni Bidin C., Vazquez R. A., 2017, *AJ*, 153, 99
- Coşkunoğlu B., et al., 2011, *MNRAS*, 412, 1237
- Dias W. S., Assafin M., Flório V., Alessi B. S., Líbero V., 2006, *A&A*, 446, 949
- Dias W. S., Monteiro H., Caetano T. C., Lépine J. R. D., Assafin M., Oliveira A. F., 2014, *A&A*, 564, A79
- Dias W. S., Monteiro H., Assafin M., 2018, *MNRAS*, 478, 5184
- Dias W. S., Monteiro H., Moitinho A., Lépine J. R. D., Carraro G., Paunzen E., Alessi B., Villela L., 2021, *MNRAS*, 504, 356
- Ferraro F. R., et al., 2012, *Nature*, 492, 393
- Gaia Collaboration et al., 2016, *A&A*, 595, A1
- Gaia Collaboration et al., 2018, *A&A*, 616, A1
- Gaia Collaboration et al., 2023, *A&A*, 674, A1
- Hasegawa T., Sakamoto T., Malasan H. L., 2008, *PASJ*, 60, 1267
- Hills J. G., Day C. A., 1976, *Astrophys. Lett.*, 17, 87
- Hunt E. L., Reffert S., 2023, *A&A*, 673, A114
- Jadhav V. V., Subramaniam A., 2021, *MNRAS*, 507, 1699
- Jurić M., et al., 2008, *ApJ*, 673, 864
- Kharchenko N. V., Piskunov A. E., Schilbach E., Röser S., Scholz R. D., 2013, *A&A*, 558, A53
- Kim S. C., Kyeong J., Park H. S., Han I., Lee J. H., Moon D.-S., Lee Y., Kim S., 2017, *Journal of Korean Astronomical Society*, 50, 79
- King I., 1962, *AJ*, 67, 471
- Krone-Martins A., Moitinho A., 2014, *A&A*, 561, A57
- Lada C. J., Lada E. A., 2003, *ARA&A*, 41, 57
- Lata S., Pandey A. K., Sagar R., Mohan V., 2002, *A&A*, 388, 158
- Leggett S. K., 1992, *ApJS*, 82, 351
- Liu L., Pang X., 2019, *ApJS*, 245, 32
- Loktin A. V., Popova M. E., 2017, *Astrophysical Bulletin*, 72, 257
- Marsakov V. A., Gozha M. L., Koval' V. V., Shpigel' L. V., 2016, *Astronomy Reports*, 60, 43
- Miyamoto M., Nagai R., 1975, *PASJ*, 27, 533
- Navarro J. F., Frenk C. S., White S. D. M., 1996, *ApJ*, 462, 563
- Rain M. J., Ahumada J. A., Carraro G., 2021, *A&A*, 650, A67
- Salpeter E. E., 1955, *ApJ*, 121, 161
- Sandage A. R., 1953, *AJ*, 58, 61
- Sariya D. P., et al., 2021, *AJ*, 161, 101
- Soubiran C., et al., 2018, *A&A*, 619, A155
- Sun M., Jiang B., Yuan H., Li J., 2021, *ApJS*, 254, 38
- Taşdemir S., Yontan T., 2023, *Physics and Astronomy Reports*, 1, 1
- Tadross A. L., 2001, *New Astron.*, 6, 293
- Tarricq Y., et al., 2021, *A&A*, 647, A19
- Zacharias N., Finch C. T., Girard T. M., Henden A., Bartlett J. L., Monet D. G., Zacharias M. I., 2013, *AJ*, 145, 44
- Zhong J., Chen L., Wu D., Li L., Bai L., Hou J., 2020, *A&A*, 640, A127
- Zinn R., Dahn C. C., 1976, *AJ*, 81, 527

³ <https://www.cosmos.esa.int/gaia>

⁴ <https://www.cosmos.esa.int/web/gaia/dpac/consortium>

A Theoretical Study: DNA Binding and ADMET Profile of Some Hydroxycinnamic Acids

B. Bıçak¹ , and S. Kecel Gündüz^{1*} 

¹Istanbul University, Faculty of Science, Department of Physics, Vezneciler, 34134, Istanbul, Türkiye

ABSTRACT

Phytochemicals are important compounds produced by plants that have various beneficial effects on human health. These compounds are found in plant structures and are known to exhibit properties such as anticancer, antioxidant, and antiviral effects, making them valuable for medical studies as potential active ingredients for drugs. Phenolic compounds are compounds that have a protective effect in various disease classes such as cardiovascular diseases, cancer, and neurodegenerative diseases. Hydroxycinnamic acids are also phenolic compounds, and prominent groups of compounds include p-coumaric acid, caffeic acid, sinapic acid and ferulic acid. These compounds are known to have various therapeutic effects, from antioxidant to anticancer effects. DNA, one of the receptors used as a target in anticancer studies, is targeted by small molecules with therapeutic effect. Theoretically, an estimate of such interactions can be made at the atomic level with the molecular docking method. In addition, pharmacokinetic properties can be determined by making estimations of absorption, distribution, metabolism, excretion, and toxicity of drug candidate molecules with ADMET studies. In this study, optimized structures, chemical stability, interactions with DNA and ADMET profiles of hydroxycinnamic acids (caffeic acid, ferulic acid, p-coumaric acid, and sinapic acid) were elucidated.

Keywords: Molecular Docking; ADMET; Hydroxycinnamic acids; DNA Binding

1. INTRODUCTION

Phytochemicals are compounds that plants produce to protect themselves. Phytochemical compounds and the number of compounds in the content vary according to the plant species. Over 5000 phytochemicals have been identified to date, but many more remain unidentified (Tsao & Deng 2004). Phytochemicals are divided into five main groups as carotenoid, phenolic compounds, alkaloids, nitrogen-containing compounds, and organosulfur group. Among them, phenolic compounds are divided into five branches. These branches are tannins, phenolic acids, flavonoids, coumarins and stilbenes. Among them, phenolic acid is classified as hydroxycinnamic acid and hydroxybenzoic acid.

Hydroxycinnamic acids, which are compounds with a C6-C3 phenylpropane structure, differ according to the position and number of hydroxyl groups attached to the phenylpropane ring. The most common types of hydroxycinnamic acid found in fruits and vegetables are chlorogenic acid, caffeic acid, p-coumaric acid, ferulic acid, and sinapic acid.

P-Coumaric acid is a compound with antioxidant, anti-inflammatory, anti-cancer, anti-diabetic, and anti-melanogenic properties and the most dominant hydroxycinnamic acid in citrus fruits and pineapple (Roychoudhury et al. 2021). P-

coumaric acid has a protective effect in atherosclerosis, oxidative cardiac injury, oxidative heart damage, UV-ocular tissue damage, neuron damage, anxiety, gout, and diabetes (Kianmehr et al. 2020). Caffeic acid, is the most dominant hydroxycinnamic acid in plums, apples, apricots, blueberries, and tomatoes, and has antioxidant, anti-inflammatory, anticancer, and neuroprotective effects (Alam et al. 2022). Caffeic acid has been found to be effective against various types of human cancer (Alam et al. 2022; Jung et al. 2007; Kang et al. 2011). Additionally, it is an antioxidant and anti-inflammatory agent (Alam et al. 2022; Korkina 2007). Ferulic acid has anti-inflammatory, antioxidant, antimicrobial activity, anticancer, and antidiabetic effect. Additionally, ferulic acid shows low toxicity and strong antioxidant effect (Zduńska et al. 2018). Sinapic acid has antioxidant, antimicrobial, anti-inflammatory, anticancer, and anti-anxiety properties (Nićiforović & Abramović 2014).

DNA has two main functions as transcription and replication. These functions have an important place in the proper functioning of the cells living and multiplying, as well as other processes in the body. DNA is one of the targets of different therapeutics such as anticancer and antiviral drugs. Small molecules can act as a drug when activation or inhibition of DNA functions is required to exert a therapeutic effect (Bıçak et al. 2022). Various

Corresponding Author: S. Kecel Gündüz **E-mail:** skecel@istanbul.edu.tr

Submitted: 14.09.2023 • **Revision Requested:** 20.10.2023 • **Last Revision Received:** 25.10.2023 • **Accepted:** 26.10.2023



This article is licensed under a Creative Commons Attribution-NonCommercial 4.0 International License (CC BY-NC 4.0)

theoretical methods are used to evaluate interactions between target macromolecules and small compounds. One of them is the molecular docking method. The aim of this study is to examine the interactions of hydroxycinnamic acids with B-DNA and to elucidate their chemical stability, absorption, absorption distribution, metabolism, excretion, and toxicity profiles.

2. MATERIAL METHOD

2.1. Optimization and HOMO-LUMO Analysis

The initial structures of caffeic acid, ferulic acid, p-coumaric acid, and sinapic acid were taken from the PubChem site with the corresponding PubChem CID numbers 689043, 445858, 637542, and 637775 (Kim et al. 2023). The optimizations of the hydroxycinnamic acids were carried out by the Gaussian09 package program (Frisch et al. 2009) using the DFT method and B3LYP/6311++G(d, p) basis set. For the determination of frontier molecular orbitals required to obtain properties such as chemical stability, ionization potential, electron affinity, and chemical hardness of all molecules under a vacuum environment.

2.2. Molecular Docking Analysis

The molecular docking method, which has an important place in the discovery of molecules with the potential of being a drug, allows to reveal of the lowest energy binding score between ligand and receptor complex structure by molecular interactions. All ligands (caffeic acid, p-coumaric acid, sinapic acid, ferulic acid) were prepared at AutoDockTools 1.5.6 software. The structure of a B-DNA Dodecamer (PDB Code: 1BNA; Drew et al. 1981) was selected as a receptor and downloaded from protein data bank¹. All water molecules in pdb file were removed, polar hydrogen atoms were added, and grid boxes were adjusted at AutoDockTools 1.5.6 software. After all preparations were completed, the molecular docking studies were realized by AutoDock Vina 1.1.2 (Trott & Olson 2010) and obtained binding affinities and RMSD values. The receptor-ligand interactions were visualized by PyMOL (DeLano 2002) software program with the obtained interaction information.

2.3. ADMET Analysis

The ADMET analyses of the caffeic acid, p-coumaric acid, sinapic acid, and ferulic acid were carried out by the online server pkCSM (Pires et al. 2015).

3. RESULT AND DISCUSSION

3.1. Structural Analysis

The hydroxycinnamic acids were optimized to obtain the values of bonds, angles, and dihedral angles with the DFT method B3LYP/6-311++ G(d, p) basis set using the Gaussian09 package program (see Tables A1, A2, A3, and A4). The energies of optimized structures were given in Table 1. Sinapic acid was determined as having the lowest energy among the hydroxycinnamic acids.

3.2. HOMO-LUMO Analysis

The highest occupied molecular orbital (HOMO) and the lowest unoccupied molecular orbital (LUMO) are related to the chemical reactivity and kinetic stability. Additionally, the HOMO is related to the ability to donate an electron and the LUMO is related to the ability to obtain an electron (Bıçak 2023; Saraç 2018).

The HOMO and LUMO energy values for p-coumaric acid in a vacuum environment were -6.40910 eV and -2.13582 eV, respectively. The HOMO and LUMO energy values for caffeic acid in a vacuum environment were -6.28610 eV and -2.1317 eV, respectively. The HOMO and LUMO energy values for ferulic acid in a vacuum environment were -6.351685 eV and -2.12439 eV, respectively. The HOMO and LUMO energy values for sinapic acid in a vacuum environment were -6.10978 eV and -2.08276 eV, respectively (see Table 2).

The large HOMO-LUMO energy gap is associated with high molecular stability. The smaller the difference (ΔE) in the energy levels, the easier the reaction will occur (Bıçak 2023; Saraç 2018). In this study, p-coumaric acid had the largest HOMO-LUMO gap, while sinapic acid had the smallest HOMO-LUMO gap. In addition, ionization potential, electron affinity, electronegativity, chemical potential, and chemical hardness information of the hydroxycinnamic acids were given in Table 2.

3.3. Molecular Docking Analysis

3.3.1. p-coumaric acid

To investigate the interaction of the p-coumaric acid molecule with B-DNA, nine different conformations of p-coumaric acid bound to B-DNA were defined. The most stable binding pose and binding affinity value among them were determined through molecular docking analysis. The best binding poses which corresponds to the best binding affinity value was calculated as -5.5 kcal mol⁻¹. The p-coumaric acid made six hydrogen bonds with B-DNA. The hydrogen bonding and close interactions between p-coumaric acid and B-DNA were given in Figure 1 and Table 3. At the close interactions, it was observed that the guanines belonging to DNA and the p-coumaric acid molecule had interacted with each other. DG10 and DG16,

¹ <https://www.rcsb.org/>

Table 1. The energies of the optimized structures of hydroxycinnamic acids.

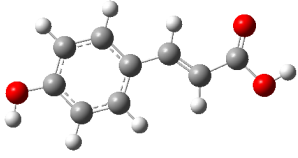
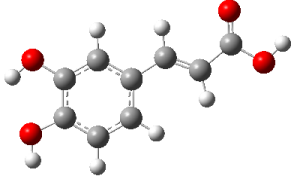
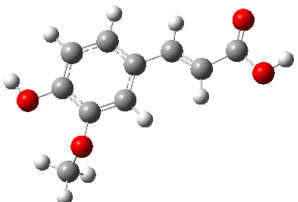
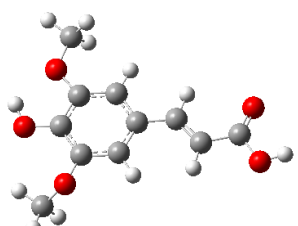
Hydroxycinnamic acids	Energy		
	a.u.	kcal mol ⁻¹	eV
 p-Coumaric acid	-573.6201	-359952	-15609.00670
 Caffeic acid	-648.8678	-407171	-17656.60088
 Ferulic acid	-688.1695	-431833	-18726.05471
 Sinapic acid	-802.7282	-503720	-21843.35682

Table 2. The calculated values of ionization potential, electron affinity, electronegativity, chemical hardness, chemical softness and HOMO-LUMO gaps for hydroxycinnamic acids.

Hydroxycinnamic acids		p-Coumaric acid		Caffeic acid		Ferulic acid		Sinapic acid	
Vacuum	TDDFT/B3LYP-6311++G(d, p)	(a.u.)	(eV)	(a.u.)	(eV)	(a.u.)	(eV)	(a.u.)	(eV)
HOMO energy	E_{HOMO}	-0.23553	-6.40910	-0.23101	-6.28610	-0.23342	-6.35168	-0.22453	-6.10978
LUMO energy	E_{LUMO}	-0.07849	-2.13582	-0.07834	-2.13174	-0.07807	-2.12439	-0.07654	-2.08276
Ionization potential	$I = -E_{\text{HOMO}}$	0.23553	6.40910	0.23101	6.28610	0.23342	6.35168	0.22453	6.10978
Electron affinity	$A = -E_{\text{LUMO}}$	0.07849	2.13582	0.07834	2.13174	0.07807	2.12439	0.07654	2.08276
Electronegativity	$\chi = (I + A)/2$	0.15701	4.27246	0.15468	4.20906	0.15575	4.23818	0.15054	4.09640
Chemical potential	$\mu = -(I + A)/2$	-0.15701	-4.27246	-0.15468	-4.20906	-0.15575	-4.23818	-0.15054	-4.09640
Chemical hardness	$\eta = (I - A)/2$	0.07852	2.13664	0.07634	2.07732	0.07768	2.11378	0.07400	2.01364
$\Delta E(\text{gap})$	$E_{\text{LUMO}} - E_{\text{HOMO}}$	0.15704	4.27328	0.15267	4.15436	0.15535	4.22729	0.14799	4.02701

which have close interactions with p-coumaric acid, were determined to form hydrogen bonds with p-coumaric acid.

It was observed that especially DG10 and DG16 are involved in hydrogen bond interactions as both donors and acceptors. O2 and O3 atoms of p-coumaric acid and H1 bonded to O3 played the most active role in hydrogen bond interactions. The p-coumaric acid made very strong hydrogen bonds. Especially strong hydrogen bonds of 2.1 Å lengths of H1 and O3 atoms

of coumaric acid with DG16 and DG10 have come to the fore. Information on all other hydrogen bond interactions between p-coumaric acid and B-DNA is given in Table 3.

3.3.2. Caffeic acid

Molecular docking analysis of DNA, which is the main target of therapeutic molecules, and caffeic acid, which has therapeutic

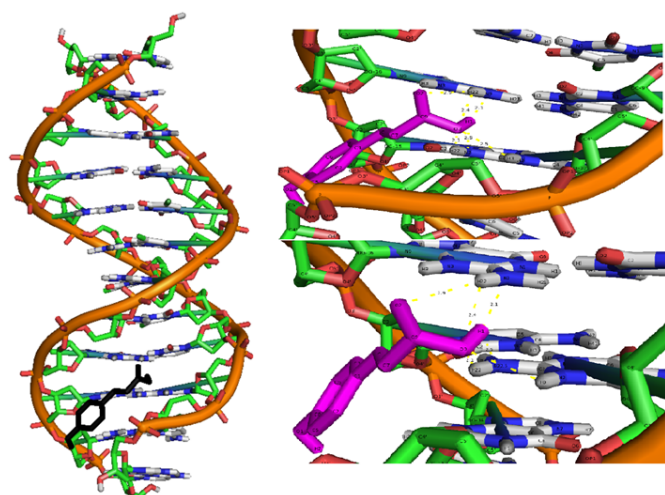


Figure 1. The close interactions of the p-coumaric acid (purple) with B-DNA.

Table 3. Hydrogen bond interactions of Coumaric acid-B-DNA complex.

Binding Affinity: $-5.5 \text{ kcal mol}^{-1}$		
Donor Atom	Acceptor Atom	Bond Length (Å)
H1 of Coumaric acid	N2 of DG16 (Chain B)	2.1
H1 of Coumaric acid	N2 of DG10 (Chain A)	2.5
H22 of DG16 (Chain B)	O2 of Coumaric acid	2.9
H22 of DG16 (Chain B)	O3 of Coumaric acid	2.4
H22 of DG10 (Chain A)	O3 of Coumaric acid	2.1
H3 of DG10 (Chain A)	O3 of Coumaric acid	2.5

effects, was performed in this study. Molecular docking analysis identified nine different conformations of caffeic acid docked to DNA, yielding the most stable binding pose and binding affinity value. As a result of molecular docking analysis, the best binding affinity value was calculated as $-6.2 \text{ kcal mol}^{-1}$. The hydrogen bonding and close interactions between caffeic acid and B-DNA were given in Figure 2 and Table 4. By looking at the close interactions, it was observed that the adenines, guanines, and cytosines belonging to DNA and the caffeic acid molecule interact. DC9, DG10, DG12, DG14, DC15, DG16, and DA17, which have close interactions with caffeic acid, were determined to form hydrogen bonds with caffeic acid.

Similar to literature studies (Ali et al. 2017; Sreejith, Mohan & Kurup 2017), it was determined that DA17, DG10, and DG16 of B-DNA were involved in hydrogen bond interactions as both donor and acceptor. Looking at the hydrogen bond interactions, it was seen that the H1, O1, and O4 atoms of caffeic acid played the most active role in binding to B-DNA. In docking studies, the stability of the complex structure and the strong bonding profile are directly proportional to the hydrogen bond interactions. In the hydrogen bond interactions, the strongest interaction occurred between the H1 of caffeic acid and the N2 atom of DG16, and its length was determined as 2.2 Å.

Information on all other hydrogen bond interactions between caffeic acid and B-DNA is given in Table 4.

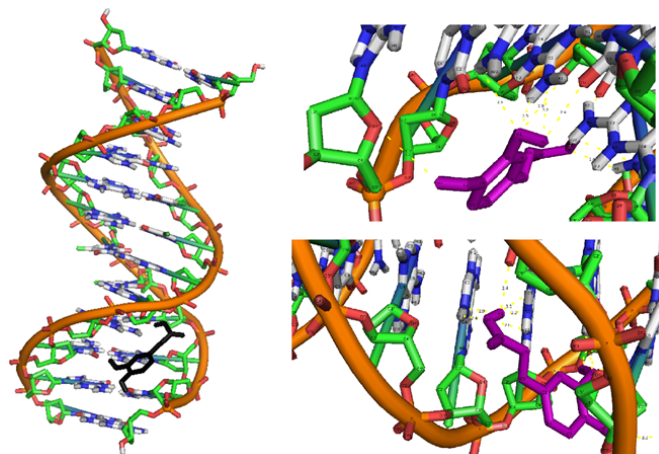


Figure 2. The close interactions of the caffeic acid (purple) with B-DNA.

Table 4. Hydrogen bond interactions of Caffeic acid with B-DNA.

Binding Affinity: $-6.2 \text{ kcal mol}^{-1}$		
Donor Atom	Acceptor Atom	Bond Length (Å)
H3 of Caffeic acid	O4' of DG12 (Chain A)	3.2
H1 of Caffeic acid	N3 of DA17 (Chain B)	2.9
H1 of Caffeic acid	O2 of DC9 (Chain A)	2.4
H1 of Caffeic acid	N2 of DG16 (Chain B)	2.2
H2 of Caffeic acid	N2 of DG10 (Chain A)	3.2
H2 of Caffeic acid	O2 of DC15 (Chain B)	2.6
H3 of DA17 (Chain B)	O4 of Caffeic acid	2.4
H22 of DG16 (Chain B)	O4 of Caffeic acid	2.8
H21 of DG16 (Chain B)	O4 of Caffeic acid	3.1
H21 of DG14 (Chain B)	O1 of Caffeic acid	2.9
H22 of DG10 (Chain A)	O1 of Caffeic acid	2.5
H21 of DG10 (Chain A)	O1 of Caffeic acid	2.9

3.3.3. Sinapic acid

By docking study of sinapic acid and B-DNA, the most suitable binding poses and binding affinities were determined, and the best binding affinity value was calculated as $-6.4 \text{ kcal mol}^{-1}$ through the AutoDock Vina program. The sinapic acid made four hydrogen bonds with DG10, DA17, and DA18 of B-DNA. According to the literature, DG10, DA17, and DA18 are important residues in hydrogen bonding interaction with B-DNA (Ali et al. 2017; Sreejith, Mohan & Kurup 2017). The hydrogen bonding and close interactions between sinapic acid and B-DNA were given in Figure 3 and Table 5.

When we examined the resulting profile of molecular docking, we observed that especially DA17 is involved in hydrogen

bond interactions as both donors and acceptors. O15 and H28 atoms of sinapic acid formed hydrogen bonds with N3 and H3 atoms of DA17. These hydrogen bonds have 2.4 Å and 2.3 Å lengths. Looking at other hydrogen bonds, H28 and O15 of sinapic acid formed a hydrogen bond with O4' atom of DA18 and H22 atom of DG 10, respectively. These hydrogen bonds have 2.5 Å and 2.4 Å lengths. In hydrogen bond interactions, an interaction with a length of around 2 Å indicates that a strong or medium hydrogen bond interaction is formed. Sinapic acid tends to have neither very strong nor very weak hydrogen bond interactions with DNA. Information on all other hydrogen bonding interactions between sinapic acid and B-DNA are given in Table 5.

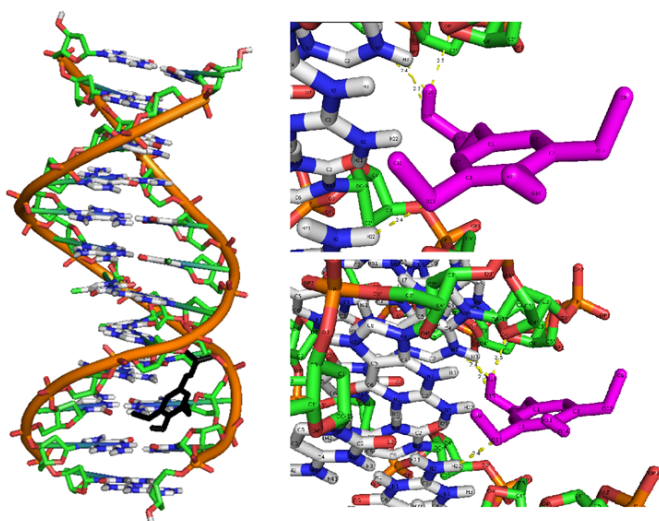


Figure 3. The close interactions of the sinapic acid (purple) with B-DNA.

Table 5. Hydrogen bond interactions of Sinapic acid with B-DNA.

Binding Affinity: $-6.4 \text{ kcal mol}^{-1}$		
Donor Atom	Acceptor Atom	Bond Length (Å)
H28 of Sinapic acid	N3 of DA17 (Chain B)	2.4
H28 of Sinapic acid	O4' of DA18 (Chain B)	2.5
H22 of DG10 (ChainA)	O13 of Sinapic acid	2.4
H3 of DA17 (Chain B)	O15 of Sinapic acid	2.3

3.3.4. Ferulic acid

In the ferulic acid and B-DNA docking study, the best nine different binding conformations and their binding energies were determined, like other hydroxycinnamic acids. The binding energy of ferulic acid in its best binding conformation was determined as $-6.4 \text{ kcal mol}^{-1}$. Ferulic acid made five hydrogen bonds with B-DNA, and in these interactions, DC9, DG10 in the A chain of B-DNA, and DG16 and DA17 in the B chain

of B-DNA stood out. The hydrogen bonding and close interactions between ferulic acid and B-DNA were given in Figure 4 and Table 6.

In the molecular docking study, H24 atom of ferulic acid had more than one hydrogen bond. H24 atom of ferulic acid formed hydrogen bonds with O2 of DC9, N2 of DG16, and N3 of DA17. The lengths of these hydrogen bonds were 1.9 Å, 3.1 Å and 3.0 Å, respectively. Considering these bond lengths, it was determined that ferulic acid makes a strong hydrogen bond with DC9. O11 and O13 atoms of ferulic acid formed hydrogen bonds with H22 of DG10 (2.4 Å) and H3 of DA17 (2.3 Å), respectively. In a docking study conducted on Ferulic acid-B-DNA, it was reported that the best binding energy was $-5.71 \text{ kcal mol}^{-1}$ (Zhang et al. 2019). In this study, the binding energy was determined as $-6.4 \text{ kcal mol}^{-1}$, and a detailed interaction profile was presented. Information on all other hydrogen bond interactions between ferulic acid and B-DNA were given in Table 6.

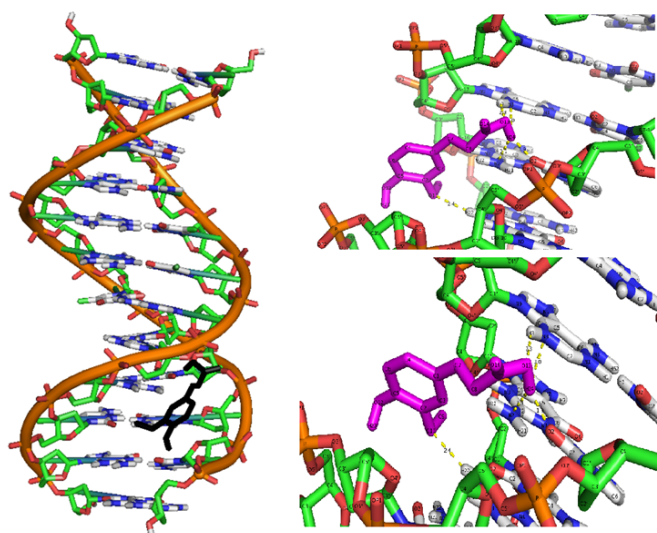


Figure 4. The close interactions of the ferulic acid (purple) with B-DNA.

Table 6. Hydrogen bond interactions of Ferulic acid with B-DNA complex.

Binding Affinity: $-6.4 \text{ kcal mol}^{-1}$		
Donor Atom	Acceptor Atom	Bond Length (Å)
H24 of Ferulic acid	O2 of DC9 (Chain A)	1.9
H24 of Ferulic acid	N3 of DA17 (Chain B)	3.0
H24 of Ferulic acid	N2 off DG16 (Chain B)	3.1
H22 of DG10 (Chain A)	O11 of Ferulic acid	2.4
H3 of DA 17 (Chain B)	O13 of Ferulic acid	2.3

Table 7. The absorption and distribution prediction of hydroxycinnamic acids.

Property	Model Name	p-Coumaric Acid	Caffeic Acid	Ferulic Acid	Sinapic Acid	Unit
		Predict	Predict	Value	Value	Numeric/Categorical
Absorption	Water solubility	-1.839	-1.737	-2.823	-2.974	(log mol/L)
Absorption	Caco2 permeability	1.144	0.123	0.249	0.057	log Papp in 10 ⁻⁶ cm/s
Absorption	Intestinal absorption (human)	91.673	65.001	94.766	94.661	% Absorbed
Absorption	Skin Permeability	-2.366	-2.625	-2.730	-2.734	log Kp
Absorption	P-glycoprotein substrate	No	Yes	Yes	Yes	Yes/No
Absorption	P-glycoprotein I inhibitor	No	No	No	No	Yes/No
Absorption	P-glycoprotein II inhibitor	No	No	No	No	Yes/No
Distribution	VDss (human)	-0.607	-0.554	-1.171	-1.068	log L/kg
Distribution	Fraction unbound (human)	0.421	0.490	0.438	0.358	Fu
Distribution	BBB permeability	-0.239	-0.824	-0.284	-0.270	log BB
Distribution	CNS permeability	-2.413	-2.649	-2.535	-2.679	log PS

3.4. ADMET Analysis

The absorption, distribution, metabolism, excretion, and toxicity properties of caffeic acid, p-coumaric acid, sinapic acid, and ferulic acid were determined with the help of the online server (pkCSM 2015). The water solubility is important for the absorption of drugs. The predicted water solubility value of a drug candidate is given as log mol L⁻¹. The predicted water solubility of 4 compounds was given in Table 7. The absorption of oral drugs is predicted using the Caco-2 monolayer cells as an in vitro model of the human intestinal mucosa permeability values were predicted and determined that p-coumaric acid has a high Caco-2 permeability (> 0.90). It was determined that these four compounds exhibit high intestinal absorption properties. According to the estimated skin permeability for all compounds, caffeic acid, ferulic acid, and sinapic acid had low skin permeability because log Kp was greater than -2.5 (Pires et al. 2015; pkCSM 2015).

P-glycoprotein is a protein of the cell membrane that pumps many foreign substances out of cells. P-glycoprotein substrate and inhibitors information for all compounds were given in Table 7. The steady-state volume of distribution was predicted for all compounds, and it was determined that all compounds were more distributed in plasma rather than tissue. Drugs are in equilibrium at the point of bound-unbound to serum proteins. The fraction unbound estimate returns the fraction that is predicted to be unbound in the plasma. The predictions of fraction unbound for all compounds were given in Table 7. When looking at the BBB and CNS permeability of the compounds, they were predicted to have weak profiles.

The compounds were determined not to be CYP P450 inhibitors based on the predictions in the metabolism section of the ADMET analysis. The predictions of Organic Cation Transporter 2 substrate were realized, and it was determined that the compounds had no renal OCT2 substrate. Total clearance values as a combination of hepatic and renal clearance were given in Table 8. When the toxicity estimates of the compounds were

examined, it was determined that they are not expected to lead to serious conditions such as skin sensitivity and hepatotoxicity. Based on Ames toxicity estimates, none of the compounds were mutagenic.

4. CONCLUSION

The study examined four hydroxycinnamic acids, and it was found that ferulic acid and sinapic acid had the lowest energy levels. The fact that ferulic acid and sinapic acid have better binding energy than the others was associated with the fact that they have more side groups for interactions. When the structure of the four compounds was examined, it was observed that the increase in binding energy was directly proportional to the increase in the groups attached to the ring. In the study of ferulic acid and sinapic acid, which have more side groups, although their binding energies were the same, their interaction sites and lengths in the DNA were different from each other. This situation was associated with the binding conformation.

In the ADMET study, it was determined that the intestinal absorption percentages of ferulic acid and sinapic acid were quite high, with values of 94.7% and 94.6%, respectively. These molecules were followed by the intestinal absorption percentages of p-coumaric acid and caffeic acid, respectively. When the toxic effects were examined with the help of pkCSM Web-servers Predictor, it was determined that hydroxycinnamic acids did not have any toxic effects according to skin sensitization, hepatotoxicity, and AMES toxicity predictions.

Table 8. The metabolism, excretion, and toxicity prediction of hydroxycinnamic acids.

Property	Model Name	p-Coumaric Acid	Cafeic Acid	Ferulic Acid	Sinapic Acid	Unit
		Predict	Predict	Value	Value	Numeric/Categorical
Metabolism	CYP2D6 substrate	No	No	No	No	Yes/No
Metabolism	CYP3A4 substrate	No	No	No	No	Yes/No
Metabolism	CYP1A2 inhibitor	No	No	No	No	Yes/No
Metabolism	CYP2C19 inhibitor	No	No	No	No	Yes/No
Metabolism	CYP2C9 inhibitor	No	No	No	No	Yes/No
Metabolism	CYP2D6 inhibitor	No	No	No	No	Yes/No
Metabolism	CYP3A4 inhibitor	No	No	No	No	Yes/No
Excretion	Total Clearance	0.696	0.544	0.619	0.760	log ml/min/kg
Excretion	Renal OCT2 substrate	No	No	No	No	Yes/No
Toxicity	AMES Toxicity	No	No	No	No	Yes/No
Toxicity	Max. tolerated dose (human)	0.758	-0.094	1.488	1.251	log mg/kg/day
Toxicity	hERG I inhibitor	No	No	No	No	Yes/No
Toxicity	hERG II inhibitor	No	No	No	No	Yes/No
Toxicity	Oral Rat Acute Toxicity (LD50)	2.070	2.281	2.491	2.411	mol/kg
Toxicity	Oral Rat Chronic Toxicity (LOAEL)	2.841	1.730	1.817	2.233	log mg/kg_bw/day
Toxicity	Hepatotoxicity	No	No	No	No	Yes/No
Toxicity	Skin Sensitization	No	No	No	No	Yes/No
Toxicity	<i>T.Pyriformis</i> toxicity	0.211	0.018	0.271	0.280	log ug/L
Toxicity	Minnow toxicity	1.815	2.072	2.074	1.731	log m

Peer Review: Externally peer-reviewed.

Author Contribution: Conception/Design of study - B.B., S.K.G; Data Acquisition - B.B., S.K.G; Data Analysis/Interpretation - B.B., S.K.G; Drafting Manuscript - B.B.; Critical Revision of Manuscript - S.K.G; Final Approval and Accountability - B.B.; Technical or Material Support - B.B., S.K.G.; Supervision: S.K.G

Conflict of Interest: Authors declared no conflict of interest.

Financial Disclosure: This study was supported by the Scientific Research Project Coordination Unit of Istanbul University [N-1650, N-3341].

LIST OF AUTHOR ORCIDS

B. Bıçak <https://orcid.org/0000-0003-1147-006X>
S. Keçel Gündüz <https://orcid.org/0000-0003-0973-8223>

REFERENCES

Alam M., Ahmed S., Elsbali A. M., Adnan M., Alam S., Hassan M. I., Pasupuleti V. R., 2022, *Front. Oncol.*, 12, 860508
Ali I., Lone M. N., Alothman Z. A., Alwarthan A., 2017, *J. Mol. Liq.*, 234, 391
Bıçak B., 2023, *J. Biomol. Struct. Dyn.*, 1

Bıçak B., Keçel Gündüz S., Budama Kılınc Y., Imhof P., Gök B., Akman G., Özel A. E., 2022, *J. Biomol. Struct. Dyn.*, 40, 12148
DeLano W. L., 2002, *Protein Crystallogr.*, 40, 82
Drew H. R., Wing R. M., Takano T., Broka C., Tanaka S., Itakura K., Dickerson R. E., 1981, *PNAS*, 78, 2179
Frisch M. J., et al., 2009, *Gaussian, Inc.*, Wallingford CT
Jung J. E., et al., 2007, *Carcinog.*, 28, 1780
Kang N. J. et al., 2011, *Carcinog.*, 32, 921
Kianmehr Z., Khorsandi K., Mohammadi M., Hosseinzadeh R., 2020, *Melanoma Res.*, 30, 136
Kim S., et al., 2023, *Nucleic Acids Res.*, 51, D1373
Korkina L., 2007, *Cellular and Molecular Biology*, 53, 15
Nićiforović N., Abramović H., 2014, *CRFSFS*, 13, 34
pkCSM: predicting small-molecule pharmacokinetic properties using graph-based signatures. Available online: URL (accessed on 10 September 2023)
Pires D. E., Blundell T. L., Ascher D. B., 2015, *J. Med. Chem.*, 58, 4066
Roychoudhury S. et al., 2021, *Antioxidants*, 10, 1205
Saraç K., 2018, *Bitlis Eren Üniversitesi Fen Bilimleri Dergisi*, 7, 311
Sreejith S., Mohan N., Kurup M. P., 2017, *Polyhedron*, 135, 278
Trott O., Olson A. J., 2010, *J. Comput. Chem.*, 31, 455
Tsao R., Deng Z., 2004, *J. Chromatogr. B.*, 812, 85
Zduńska K., Dana A., Kolodziejczak A., Rotsztein H., 2018, *Skin Pharmacol Physiol.*, 31, 332
Zhang G., Zhou Z., Xu J., Liao Y., Hu X., 2019, *J. Biomol. Struct. Dyn.*, 38, 1

Table A1. The optimized parameters of p-Coumaric acid.

	Value		Value		Value
R(1, 2)	1.3948	A(2, 1, 3)	120.0022	D(3, 1, 2, 4)	0.0138
R(1, 3)	1.3949	A(2, 1, 7)	120.0110	D(3, 1, 2, 13)	-178.7482
R(1, 7)	1.4544	A(3, 1, 7)	119.9868	D(7, 1, 2, 4)	-179.9659
R(2, 4)	1.3949	A(1, 2, 4)	119.9949	D(7, 1, 2, 13)	1.2721
R(2, 13)	1.0861	A(1, 2, 13)	122.5790	D(2, 1, 3, 5)	-0.0050
R(3, 5)	1.3949	A(4, 2, 13)	117.4151	D(2, 1, 3, 14)	-179.9182
R(3, 14)	1.0874	A(1, 3, 5)	119.9978	D(7, 1, 3, 5)	179.9747
R(4, 6)	1.3948	A(1, 3, 14)	121.0590	D(7, 1, 3, 14)	0.0615
R(4, 15)	1.0868	A(5, 3, 14)	118.9431	D(2, 1, 7, 8)	20.0056
R(5, 6)	1.3948	A(2, 4, 6)	120.0055	D(2, 1, 7, 17)	-160.7266
R(5, 16)	1.0865	A(2, 4, 15)	119.3118	D(3, 1, 7, 8)	-159.9741
R(6, 10)	1.3608	A(6, 4, 15)	120.6821	D(3, 1, 7, 17)	19.2936
R(7, 8)	1.3516	A(3, 5, 6)	120.0008	D(1, 2, 4, 6)	-0.0133
R(7, 17)	1.0881	A(3, 5, 16)	119.6696	D(1, 2, 4, 15)	-179.7477
R(8, 9)	1.4767	A(6, 5, 16)	120.3296	D(13, 2, 4, 6)	178.8116
R(8, 18)	1.0841	A(4, 6, 5)	119.9988	D(13, 2, 4, 15)	-0.9229
R(9, 11)	1.3535	A(4, 6, 10)	119.9935	D(1, 3, 5, 6)	-0.0044
R(9, 12)	1.2194	A(5, 6, 10)	120.0077	D(1, 3, 5, 16)	-179.9777
R(10, 19)	0.9727	A(1, 7, 8)	125.3127	D(14, 3, 5, 6)	179.9107
R(11, 20)	0.9811	A(1, 7, 17)	115.4297	D(14, 3, 5, 16)	-0.0627
		A(8, 7, 17)	119.2537	D(2, 4, 6, 5)	0.0039
		A(7, 8, 9)	120.0806	D(2, 4, 6, 10)	179.9933
		A(7, 8, 18)	122.9350	D(15, 4, 6, 5)	179.7346
		A(9, 8, 18)	116.9719	D(15, 4, 6, 10)	-0.2760
		A(8, 9, 11)	108.6985	D(3, 5, 6, 4)	0.0050
		A(8, 9, 12)	126.4575	D(3, 5, 6, 10)	-179.9844
		A(11, 9, 12)	124.8440	D(16, 5, 6, 4)	179.9781
		A(6, 10, 19)	108.9074	D(16, 5, 6, 10)	-0.0113
		A(9, 11, 20)	111.9898	D(4, 6, 10, 19)	-0.0169
				D(5, 6, 10, 19)	179.9725
				D(1, 7, 8, 9)	179.5317
				D(1, 7, 8, 18)	0.8608
				D(17, 7, 8, 9)	0.2897
				D(17, 7, 8, 18)	-178.3812
				D(7, 8, 9, 11)	-179.4305
				D(7, 8, 9, 12)	0.6322
				D(18, 8, 9, 11)	-0.6822
				D(18, 8, 9, 12)	179.3806
				D(8, 9, 11, 20)	-179.9700
				D(12, 9, 11, 20)	-0.0315

Table A2. The optimized parameters of Caffeic acid.

	Value		Value		Value
R(1, 2)	1.3949	A(2, 1, 3)	120.000	D(3, 1, 2, 4)	-0.0092
R(1, 3)	1.3949	A(2, 1, 7)	119.999	D(3, 1, 2, 14)	179.9170
R(1, 7)	1.4543	A(3, 1, 7)	120.001	D(7, 1, 2, 4)	179.9519
R(2, 4)	1.3948	A(1, 2, 4)	120.001	D(7, 1, 2, 14)	-0.1219
R(2, 14)	1.0880	A(1, 2, 14)	120.673	D(2, 1, 3, 6)	-0.0044
R(3, 6)	1.3949	A(4, 2, 14)	119.326	D(2, 1, 3, 15)	178.3207
R(3, 15)	1.0858	A(1, 3, 6)	119.993	D(7, 1, 3, 6)	-179.9660
R(4, 5)	1.3948	A(1, 3, 15)	122.998	D(7, 1, 3, 15)	-1.6404
R(4, 10)	1.3622	A(6, 3, 15)	116.989	D(2, 1, 7, 8)	160.0399
R(5, 6)	1.3949	A(2, 4, 5)	120.001	D(2, 1, 7, 17)	-19.2341
R(5, 11)	1.3621	A(2, 4, 10)	119.494	D(3, 1, 7, 8)	-19.9990
R(6, 16)	1.0869	A(5, 4, 10)	120.505	D(3, 1, 7, 17)	160.7270
R(7, 8)	1.3298	A(4, 5, 6)	120.001	D(1, 2, 4, 5)	0.0230
R(7, 17)	1.0870	A(4, 5, 11)	120.532	D(1, 2, 4, 10)	179.9211
R(8, 9)	1.4776	A(6, 5, 11)	119.467	D(14, 2, 4, 5)	-179.9040
R(8, 18)	1.0831	A(3, 6, 5)	120.004	D(14, 2, 4, 10)	-0.0061
R(9, 12)	1.3536	A(3, 6, 16)	119.279	D(1, 3, 6, 5)	0.0041
R(9, 13)	1.2194	A(5, 6, 16)	120.716	D(1, 3, 6, 16)	179.6570
R(10, 19)	0.9730	A(1, 7, 8)	122.838	D(15, 3, 6, 5)	-178.4190
R(11, 20)	0.9727	A(1, 7, 17)	116.184	D(15, 3, 6, 16)	1.2334
R(12, 21)	0.9811	A(8, 7, 17)	120.974	D(2, 4, 5, 6)	-0.0233
		A(7, 8, 9)	118.549	D(2, 4, 5, 11)	179.9629
		A(7, 8, 18)	124.626	D(10, 4, 5, 6)	-179.9200
		A(9, 8, 18)	116.797	D(10, 4, 5, 11)	0.0658
		A(8, 9, 12)	108.688	D(2, 4, 10, 19)	-179.9570
		A(8, 9, 13)	126.492	D(5, 4, 10, 19)	-0.0597
		A(12, 9, 13)	124.819	D(4, 5, 6, 3)	0.0097
		A(4, 10, 19)	108.332	D(4, 5, 6, 16)	-179.6380
		A(5, 11, 20)	109.015	D(11, 5, 6, 3)	-179.9770
		A(9, 12, 21)	111.987	D(11, 5, 6, 16)	0.3757
				D(4, 5, 11, 20)	-179.9790
				D(6, 5, 11, 20)	0.0075
				D(1, 7, 8, 9)	-179.2020
				D(1, 7, 8, 18)	-1.2206
				D(17, 7, 8, 9)	0.0379
				D(17, 7, 8, 18)	178.0194
				D(7, 8, 9, 12)	179.2113
				D(7, 8, 9, 13)	-0.7861
				D(18, 8, 9, 12)	1.0721
				D(18, 8, 9, 13)	-178.9250
				D(8, 9, 12, 21)	-179.9950
				D(13, 9, 12, 21)	0.0024








Table A3. The optimized parameters of Ferulic acid.

	Value		Value		Value
R(1, 3)	1.3950	A(3, 1, 4)	120.0001	D(4, 1, 3, 2)	-0.0123
R(1, 4)	1.3949	A(3, 1, 7)	120.0122	D(4, 1, 3, 15)	-178.7161
R(1, 7)	1.4543	A(4, 1, 7)	119.9877	D(7, 1, 3, 2)	-179.9620
R(2, 3)	1.3949	A(3, 2, 5)	119.9983	D(7, 1, 3, 15)	1.3342
R(2, 5)	1.3949	A(3, 2, 11)	119.4636	D(3, 1, 4, 6)	0.0076
R(2, 11)	1.3623	A(5, 2, 11)	120.5381	D(3, 1, 4, 16)	-179.8972
R(3, 15)	1.0866	A(1, 3, 2)	119.9925	D(7, 1, 4, 6)	179.9573
R(4, 6)	1.3948	A(1, 3, 15)	122.1636	D(7, 1, 4, 16)	0.0525
R(4, 16)	1.0875	A(2, 3, 15)	117.8318	D(3, 1, 7, 8)	19.9509
R(5, 6)	1.3949	A(1, 4, 6)	120.0083	D(3, 1, 7, 18)	-160.7625
R(5, 12)	1.3623	A(1, 4, 16)	121.0485	D(4, 1, 7, 8)	-159.9988
R(6, 17)	1.0867	A(6, 4, 16)	118.9431	D(4, 1, 7, 18)	19.2878
R(7, 8)	1.3516	A(2, 5, 6)	120.0113	D(5, 2, 3, 1)	0.0115
R(7, 18)	1.0881	A(2, 5, 12)	120.5463	D(5, 2, 3, 15)	178.7706
R(8, 10)	1.4765	A(6, 5, 12)	119.4424	D(11, 2, 3, 1)	-179.9685
R(8, 19)	1.0841	A(4, 6, 5)	119.9896	D(11, 2, 3, 15)	-1.2093
R(9, 11)	1.4262	A(4, 6, 17)	119.2501	D(3, 2, 5, 6)	-0.0059
R(9, 20)	1.0946	A(5, 6, 17)	120.7603	D(3, 2, 5, 12)	-179.9288
R(9, 21)	1.0946	A(1, 7, 8)	125.3211	D(11, 2, 5, 6)	179.9738
R(9, 22)	1.0934	A(1, 7, 18)	115.4272	D(11, 2, 5, 12)	0.0509
R(10, 13)	1.3536	A(8, 7, 18)	119.2480	D(3, 2, 11, 9)	-90.0288
R(10, 14)	1.2195	A(7, 8, 10)	120.0888	D(5, 2, 11, 9)	89.9913
R(12, 23)	0.9726	A(7, 8, 19)	122.9422	D(1, 4, 6, 5)	-0.0020
R(13, 24)	0.9810	A(10, 8, 19)	116.9558	D(1, 4, 6, 17)	-179.9938
		A(11, 9, 20)	110.4884	D(16, 4, 6, 5)	179.9048
		A(11, 9, 21)	110.6345	D(16, 4, 6, 17)	-0.0870
		A(11, 9, 22)	108.2689	D(2, 5, 6, 4)	0.0012
		A(20, 9, 21)	110.0868	D(2, 5, 6, 17)	179.9928
		A(20, 9, 22)	108.6520	D(12, 5, 6, 4)	179.9250
		A(21, 9, 22)	108.6468	D(12, 5, 6, 17)	-0.0834
		A(8, 10, 13)	108.7071	D(2, 5, 12, 23)	-179.9637
		A(8, 10, 14)	126.4598	D(6, 5, 12, 23)	0.1130
		A(13, 10, 14)	124.8331	D(1, 7, 8, 10)	179.5313
		A(2, 11, 9)	117.0371	D(1, 7, 8, 19)	0.8986
		A(5, 12, 23)	109.0069	D(18, 7, 8, 10)	0.2697
		A(10, 13, 24)	111.9924	D(18, 7, 8, 19)	-178.3630
				D(7, 8, 10, 13)	-179.4288
				D(7, 8, 10, 14)	0.6317
				D(19, 8, 10, 13)	-0.7161
				D(19, 8, 10, 14)	179.3444
				D(20, 9, 11, 2)	61.5627
				D(21, 9, 11, 2)	-60.6100
				D(22, 9, 11, 2)	-179.5631
				D(8, 10, 13, 24)	-179.9668
				D(14, 10, 13, 24)	-0.0260

Table A4. The optimized parameters of Sinapic acid.

	Value		Value		Value
R(1, 5)	1.3948	A(5, 1, 6)	119.9937	D(6, 1, 5, 2)	0.0003
R(1, 6)	1.3948	A(5, 1, 7)	120.0033	D(6, 1, 5, 17)	179.8788
R(1, 7)	1.4545	A(6, 1, 7)	120.0029	D(7, 1, 5, 2)	179.9946
R(2, 4)	1.3949	A(4, 2, 5)	119.9939	D(7, 1, 5, 17)	-0.1269
R(2, 5)	1.3949	A(4, 2, 12)	120.5790	D(5, 1, 6, 3)	-0.0004
R(2, 12)	1.3623	A(5, 2, 12)	119.4271	D(5, 1, 6, 18)	178.8619
R(3, 4)	1.3948	A(4, 3, 6)	120.0036	D(7, 1, 6, 3)	-179.9946
R(3, 6)	1.3948	A(4, 3, 13)	120.5715	D(7, 1, 6, 18)	-1.1324
R(3, 13)	1.3624	A(6, 3, 13)	119.4249	D(5, 1, 7, 8)	160.0005
R(4, 14)	1.3635	A(2, 4, 3)	119.9978	D(5, 1, 7, 19)	-20.5850
R(5, 17)	1.0854	A(2, 4, 14)	119.9973	D(6, 1, 7, 8)	-20.0052
R(6, 18)	1.0867	A(3, 4, 14)	120.0050	D(6, 1, 7, 19)	159.4092
R(7, 8)	1.3516	A(1, 5, 2)	120.0075	D(5, 2, 4, 3)	-0.0186
R(7, 19)	1.0883	A(1, 5, 17)	117.0108	D(5, 2, 4, 14)	179.9913
R(8, 11)	1.4766	A(2, 5, 17)	122.9816	D(12, 2, 4, 3)	-179.9688
R(8, 20)	1.0841	A(1, 6, 3)	120.0035	D(12, 2, 4, 14)	0.0411
R(9, 12)	1.4262	A(1, 6, 18)	122.0969	D(4, 2, 5, 1)	0.0092
R(9, 22)	1.0953	A(3, 6, 18)	117.8902	D(4, 2, 5, 17)	-179.8618
R(9, 23)	1.0954	A(1, 7, 8)	125.3163	D(12, 2, 5, 1)	179.9599
R(9, 24)	1.0951	A(1, 7, 19)	115.7052	D(12, 2, 5, 17)	0.0890
R(10, 13)	1.4261	A(8, 7, 19)	118.9759	D(4, 2, 12, 9)	179.9979
R(10, 25)	1.0946	A(7, 8, 11)	120.0815	D(5, 2, 12, 9)	0.0474
R(10, 26)	1.0946	A(7, 8, 20)	123.0911	D(6, 3, 4, 2)	0.0185
R(10, 27)	1.0935	A(11, 8, 20)	116.7585	D(6, 3, 4, 14)	-179.9913
R(11, 15)	1.3536	A(12, 9, 22)	111.6668	D(13, 3, 4, 2)	-179.9790
R(11, 16)	1.2192	A(12, 9, 23)	111.6539	D(13, 3, 4, 14)	0.0111
R(14, 21)	0.9730	A(12, 9, 24)	107.0681	D(4, 3, 6, 1)	-0.0091
R(15, 28)	0.9811	A(22, 9, 23)	112.471	D(4, 3, 6, 18)	-178.9186
		A(22, 9, 24)	106.7918	D(13, 3, 6, 1)	179.9885
		A(23, 9, 24)	106.7903	D(13, 3, 6, 18)	1.0790
		A(13, 10, 25)	110.4906	D(4, 3, 13, 10)	90.0047
		A(13, 10, 26)	110.6405	D(6, 3, 13, 10)	-89.9929
		A(13, 10, 27)	108.2629	D(2, 4, 14, 21)	0.0531
		A(25, 10, 26)	110.0823	D(3, 4, 14, 21)	-179.9371
		A(25, 10, 27)	108.6523	D(1, 7, 8, 11)	179.5311
		A(26, 10, 27)	108.6486	D(1, 7, 8, 20)	-3.5866
		A(8, 11, 15)	108.6941	D(19, 7, 8, 11)	0.1342
		A(8, 11, 16)	126.4593	D(19, 7, 8, 20)	177.0165
		A(15, 11, 16)	124.8465	D(7, 8, 11, 15)	150.5662
		A(2, 12, 9)	117.0263	D(7, 8, 11, 16)	-29.3597
		A(3, 13, 10)	117.0277	D(20, 8, 11, 15)	-26.5087
		A(4, 14, 21)	108.3761	D(20, 8, 11, 16)	153.5655
		A(11, 15, 28)	111.9876	D(22, 9, 12, 2)	63.3908
				D(23, 9, 12, 2)	-63.4953
				D(24, 9, 12, 2)	179.9521
				D(25, 10, 13, 3)	61.6522
				D(26, 10, 13, 3)	-60.5204
				D(27, 10, 13, 3)	-179.4756
				D(8, 11, 15, 28)	-179.9644
				D(16, 11, 15, 28)	-0.0371

Verification of the Existence of Recently Published New Energy Levels of Atomic Holmium

D. Bingöl¹ , Gö. Başar^{2*} , Gü. Başar³ , I. K. Öztürk² , F. Güzelçimen² , S. K. Barka^{4,5} , and S. Kröger⁶ 

¹Istanbul University, Institute of Graduate Studies in Sciences, 34452, Beyazit, Istanbul, Türkiye

²Istanbul University, Faculty of Science, Department of Physics, 34134, Vezneciler, Istanbul, Türkiye

³Istanbul Technical University, Faculty of Science and Letters, Physics Engineering Department, 34469, Maslak, Istanbul, Türkiye

⁴Istanbul Technical University, Graduate School, Physics Engineering Program, 34469, Maslak, Istanbul, Türkiye

⁵Acibadem Mehmet Ali Aydınlar University, Vocational School of Health Services, Opticianry Program, 34752, Ataşehir, Istanbul, Türkiye

⁶Hochschule für Technik und Wirtschaft Berlin, Fachbereich 1, Wilhelminenhofstr. 75A, 12459, Berlin, Germany

ABSTRACT

The objective of this work was to review five energy levels of atomic Holmium that are reported in the literature, for which are indicated that further verification is required. All theoretically possible transitions to these 5 levels were investigated experimentally in the wavelength region of a TiSa laser from 693 nm to 765 nm using laser-induced fluorescence spectroscopy and a hollow cathode discharge lamp. In case a laser-induced fluorescence was detected, the hyperfine structure of the measured lines was fitted and used as fingerprint in the confirmation of the levels under investigation. A total of 20 lines were investigated with laser spectroscopy, but only 2 among those lines were suitable for the intended verification. Therefore, selected lines from a previously measured Fourier Transform (FT) spectra were analysed, additionally. The experimental hyperfine structures were compared with the simulated ones. 9 of the 25 examined FT lines confirm the existence of the levels under investigation. Further 3 FT lines were strongly disturbed by neighbouring overlapped lines. Despite the number of lines, only 2 of 5 levels could be confirmed with high certainty. For the other 3 levels, the lines seen in the FT spectrum were either weak or unresolved, so that confirmation was not possible with a high degree of certainty.

Keywords: laser spectroscopy; hyperfine structure; holmium

1. INTRODUCTION

The rare earth element holmium (Ho), has an atomic number of 67 and has only one stable isotope, ¹⁶⁵Ho. It plays an important role in astrophysics, namely in the study of nucleosynthesis, the process by which heavy elements are created in stars, and in measuring the age of a star cluster (see for example, [Snedden et al. 2009](#)).

The ground state electron configuration of atomic holmium (Ho I) is [Xe]4f¹¹ 6s² with the term ⁴I_{15/2}. The isotope ¹⁶⁵Ho has the nuclear spin quantum number $I = 7/2$, relatively high nuclear magnetic moment $\mu_I = 4.17(3) \mu_N$ and a fairly big electric quadrupole moment $Q = +2.74 \text{ barn} - 3.6 \text{ barn}$ ([Stone 2005](#)). Due to the open *f*-electron shell configuration, Ho I has a high density of spectral lines and a correspondingly large number of fine structure levels. All the mentioned properties distinguish Ho as a good candidate for the investigation of fine structure and hyperfine structure and make it a subject of study by us and other research groups, especially in the last decade ([Al-Labady et al. 2017](#); [Başar et al. 2017](#); [Stefanska et](#)

[al. 2018a,b,c](#); [Furmann et al. 2018](#); [Özdağlıç et al. 2019a,b,c](#); [Elantkowska et al. 2019](#); [Başar et al. 2020](#); [Chomski et al. 2021, 2022, 2023](#)). Despite all accomplished and ongoing research, there is still lack of information on the fine structure (fs) and hyperfine structure (hfs) of Ho I.

In the most recent paper on the fs and hfs of atomic Ho conducted by [Chomski et al. \(2023\)](#), 32 new energy levels are given. It is stated by [Chomski et al. \(2023\)](#) that five of these levels need further verification. The purpose of the present study is to investigate and confirm these five levels.

2. EXPERIMENT

Laser induced fluorescence (LIF) spectroscopy was used to verify the unconfirmed energy levels of the Holmium atom given by [Chomski et al. \(2023\)](#). A laboratory made hollow cathode lamp was used to measure the hfs spectra of free Ho atoms. A 0.125 mm thick Ho foil was placed inside the 20 mm long cylindrical hollow cathode made of copper. The gas discharge

Corresponding Author: Gö. Başar **E-mail:** gbasar@istanbul.edu.tr

Submitted: 13.10.2023 • **Revision Requested:** 28.10.2023 • **Last Revision Received:** 05.11.2023 • **Accepted:** 06.11.2023



This article is licensed under a Creative Commons Attribution-NonCommercial 4.0 International License (CC BY-NC 4.0)

runs with Ne inert gas at about 2 mbar pressure and a discharge current of 60 mA. Doppler line broadening was reduced by cooling the cathode with liquid nitrogen.

A tunable cw single longitudinal mode Ti-Sa laser (Coherent, MBR 110, 4 W) pumped with a solid state laser (Coherent, Verdi 18 W) was used for the excitation of Ho atoms. In this study, the wavelength range from 693 nm to 765 nm was available. In order to keep the saturation broadening of the absorption lines low, the power of the laser was reduced to 1 W.

The laser beam was modulated with a mechanical chopper before passing through the gaseous plasma and the LIF measurements were performed with the lock-in technique. For the LIF measurements, the fluorescent light emitted from the hollow cathode lamp was collected with the help of a lens and mirrors and with another lens it was to be redirected and focused on the entrance slit of a monochromator (McPherson 607, grating: 1200 lines/mm). The fluorescence light was detected with a Photomultiplier (Hamamatsu, R928) at the exit slit of the monochromator. The fluorescence transitions from the upper level of the laser-excitation transition were recorded as positive LIF signals, whereas the fluorescence transitions from the lower level of the laser-excitation transition were recorded as negative LIF signals.

To measure the hfs of the lines under investigation, the laser wavelength was scanned continuously over a range of up to 25 GHz according to the width of the structures. The absolute wavelength of the laser was measured with the help of a wavemeter (High Finesse 6-200). For calibration of the relative frequency axis of the scan range, a small portion of the laser beam was sent to a lab-built, temperature-controlled confocal Fabry-Perot interferometer. The interference maxima obtained simultaneously with the measurement were used for the calibration of the frequency scale. The scanning rate of the wavelength was usually set to 2.5 GHz min^{-1} and recorded as steps of about 2 MHz. Each line measured with LIF was registered at least five times.

In addition to the laser measurements, data from Fourier Transform (FT) spectra were available for evaluation. The FT spectra in the wavelength range of 300 nm to 850 nm were measured with a resolution of 0.025 cm^{-1} with the FT Spectrometer IFS125 HR at the Laser Centre of the University of Latvia in Riga and were already discussed in our previous studies (Özdoğan et al. 2019a,b,c).

3. METHOD FOR INVESTIGATION OF UNCONFIRMED LEVELS

In this work, five fine structure energy levels indicated as “probably existing new” and “require further verification” by Chomski et al. (2023) were investigated for confirmation. These levels are listed in Table 1 together with all the information provided in the reference. The last column of Table 1 presents the result of our investigation, which will be explained in the following sections.

Table 1. Energy levels (sorted by parity and then by energy) given by Chomski et al. (2023) as new but unconfirmed, together with their J quantum number, parity p and hyperfine structure constants A and B as given in Chomski et al. (2023). For comment see text in Section 4.

$E(\text{cm}^{-1})$	J	p	A (MHz)	B (MHz)	Comment (this work)
39019.06	11/2	e	1111.8 (6.5)	231 (26)	confirmed
40438.59	13/2	e	784.8 (2.0)	388 (91)	further verification recomm.
42189.40	9/2	e	451.4 (1.4)	-698 (192)	further verification recomm.
36071.92	19/2	o	980.6 (1.5)	2043 (103)	confirmed
44283.99	23/2	o	619.3 (1.9)	2481 (113)	further verification recomm.

As a first step, all theoretically possible transitions to these five levels in the wavelength range of the laser were calculated. For this step the program ELEMENTS (Windholz 2016) was used. The programme allows to simulate the hfs of the lines and to search for the appropriate fluorescence lines. The simulations are based on the hfs constants A and B from the literature.

In the next step, for each line the laser was scanned at the position of the calculated wavelengths. The width of the scan was estimated by the results of the simulation of the hfs. For these LIF measurements, the monochromator was in each case adjusted to the most intense fluorescence lines from the lower or the upper energy levels of the calculated transition, respectively. Information about the intensities of the calculated fluorescence lines could be found in the literature (Özdoğan et al. 2019a,b) and was also provided via the program ELEMENTS. If no signal was found in the first attempt, other fluorescence lines were tested.

If a signal was detected and the line could be measured, subsequently the hfs of this line was examined. For this purpose the FITTER program (Zeiser et al. 2022) was used to fit the calculated hfs line profile to the experimental intensity distribution. The Voigt profile function was chosen. The program performs an iterative least-squares fit to optimize the fit parameters.

The focus of this present work is to confirm the findings of Chomski et al. (2023), for this to accomplish the HFS constants A and B of the upper and lower levels were fixed during the fit. The Voigt profile function with same profile parameter was used for each individual hfs component. The only free fit parameters were the centre of gravity of the hyperfine structure, the total intensity of the line, the full width at half maximum (FWHM) and a profile parameter, which describes the ratio of the Gaussian to the Lorentzian part in the Voigt profile. The intensities of the individual hfs components were coupled to the most intense component. Since in the LIF spectra the saturation effect clearly influences the intensity ratios of the individual hfs component, the saturation effect was taken into account, according to the procedure described in Kröger et al. (2023).

Table 2. Investigated energy levels, sorted by parity and energy together with all lines investigated with laser induced fluorescence (LIF) spectroscopy or Fourier transform (FT) spectroscopy. The second to last column lists the measurement method used in this work, the column before lists the method used in reference [1]. For comments see table notes.

Upper level from [1]			Line			Lower level			Comments		
E (cm ⁻¹)	J	p	λ_{air} (nm)	σ (cm ⁻¹)	S/R	E (cm ⁻¹)	J	p	[1]	This work	
39019.06(0.03)	11/2	e	496.102	20151.52		18867.54	13/2	o	LIF	FT	different structure
			527.327	18958.30	10	20060.76	11/2	o	LIF	FT*	observed
			539.653	18525.29	11	20493.77	13/2	o	observed	FT*	observed
			745.920	13402.58		25616.48	11/2	o		LIF*	observed
			756.564	13214.02		25805.04	9/2	o		LIF	different structure
40438.59(0.04)	13/2	e	457.196	21866.31		18572.28	15/2	o	FT	FT	different structure
			472.421	21161.65	7	19276.94	15/2	o	FT	FT**	blend
			501.243	19944.83		20493.76	13/2	o	LIF	FT	different structure
			533.023	18755.69	21	21682.90	15/2	o	observed	FT**	blend with very strong line (S/N=3900)
			542.606	18424.47	6	22014.12	15/2	o		FT*	observed, but very weak and only one peak
			557.880	17920.04	5	22518.55	11/2	o		FT**	only faintly visible at under a blending line
			693.527	14415.07		26023.52	15/2	o		LIF	not observed
			698.552	14311.37		26127.22	13/2	o		LIF	not observed
			702.044	14240.20		26198.39	15/2	o		LIF	not observed
			703.395	14212.84		26225.75	13/2	o		LIF	not observed
			706.494	14150.49		26288.10	13/2	o		LIF	not observed
			714.321	13995.46		26443.13	11/2	o		LIF	not observed
			715.015	13981.87		26456.72	15/2	o		LIF	not observed
			718.773	13908.76		26529.83	11/2	o		LIF	not observed
			725.810	13773.92		26664.67	11/2	o		LIF	not observed
			726.287	13764.87		26673.72	13/2	o		LIF	not observed
			733.621	13627.27		26811.32	15/2	o		LIF	not observed
739.650	13516.19		26922.40	15/2	o		LIF	not observed			
742.668	13461.25		26977.34	13/2	o		LIF	not observed			
746.688	13388.79		27049.80	11/2	o		LIF	not observed			
42189.40(0.05)	9/2	e	451.776	22128.64		20060.76	11/2	o	weak	FT	not observed
			499.074	20031.52	23	22157.88	9/2	o	LIF	FT*	observed
			508.226	19670.81	12	22518.59	11/2	o	LIF	FT	blend, no statement possible
			510.169	19595.87	4	22593.53	11/2	o	LIF	FT	very weak, other structure
			538.165	18576.48		23612.92	11/2	o	weak	FT	not observed
			737.989	13546.61		28642.79	11/2	o		LIF	not observed
764.707	13073.30		29116.10	11/2	o		LIF	not observed			
36071.92(0.05)	19/2	o	360.999	27693.01	9	8378.91	17/2	e	weak	FT	different structure
			403.933	24749.61	23	11322.31	21/2	e	FT	FT*	observed
			410.020	24382.15	178	11689.77	19/2	e	strong	FT*	observed, blend
			515.629	19388.40	14	16683.52	19/2	e	LIF	FT	different structure
			735.360	13595.03		22476.89	17/2	e		LIF	not observed
757.059	13205.37		22866.55	19/2	e		LIF*	observed			
44283.99(0.09)	23/2	o	438.683	22789.10		21494.89	21/2	e	observed	FT	not observed
			448.238	22303.32	4	21980.67	23/2	e	observed	FT*	observed, very weak
			477.940	20917.28	26	23366.71	21/2	e	FT	FT*	observed, blend
			478.136	20908.71	18	23375.28	25/2	e	observed	FT	blend
			493.013	20277.76	12	24006.23	23/2	e	LIF	FT	blend
			510.853	19569.65	19	24714.34	21/2	e	LIF	FT*	observed
533.500	18738.92		25545.07	21/2	e	LIF	FT	not observed			

there is no theoretical line to this level in the wavelength range used with our laser

[1] Chomski et al. (2022)

Note: p: parity, e: even, o: odd;

(*): line used for confirmation; (**): line with blend, confirmation not certain.

All comments in the third last column are from reference [1]; LIF not observed: the line is even not visible in our FT spectrum; different structure: the line is not observed, but another line is present at nearly the same wavelength

In addition to the laser measurements, lines were examined in the FT spectrum. For this as well the program ELEMENTS was used. All theoretically possible lines connected to the five levels under investigation were checked. If a signal was visible in the experimental FT spectrum, the hfs of the line was simulated and the simulated curve was compared with the corresponding section of the experimental spectrum. In several cases the line of interest was overlapped by another line (so-called blends). Sometimes the structure you are looking for can still be clearly recognised. Then the recognised section is compared with the simulation. Sometimes no clear statement can be made at all. In two cases the simulation was carried out with the superposition of two structures, in order to provide a better evidence for the investigated line. Since the simulation of the superposition of two structures is not possible with the simulation tool of the program ELEMENTS, the fit program FITTER (Zeiser et al. 2022) was used for this purpose with all parameters fixed except the centre of gravity of both structures.

The concrete results for the individual levels are discussed in the next section.

4. RESULTS

All spectral lines examined are compiled in Table 2, sorted by upper levels under investigation and by wavelength. The wave numbers σ were calculated according to Ritz combination principle from difference between upper and lower level energy. The wavelength in air λ_{air} were calculated from σ using the refractive index of air according to Ciddor (1996). Energy values and J values of the upper levels are given according to Chomski et al. (2023), the lower levels according to Wyart et al. (1977); Martin et al. (1978); Kröger et al. (1997).

All lines examined with the LIF method are included in Table 2; if no LIF signal was found, then with the corresponding comment. The lines examined in the FT spectrum were only listed in the table when a signal could be seen at the corresponding position. Exceptions are lines mentioned in Chomski et al. (2023). Such lines were also included in the table even though no signal could be seen at the location in our spectra (with the corresponding comment).

A total of 20 lines were examined with LIF. LIF signal could only be detected for three of these lines. For one out of the three lines, the hfs of the line did not match the expected transition. So in the end, matching LIF lines were only found for two of the levels under investigation.

Level 39019.06 cm^{-1}

For this level, two FT lines and one LIF line were found, all of which show clear and distinct structures that support the assumption of the level's existence. The lines are shown in Figure 1.

The simulations for the FT spectrum (Figure 1a and b) are

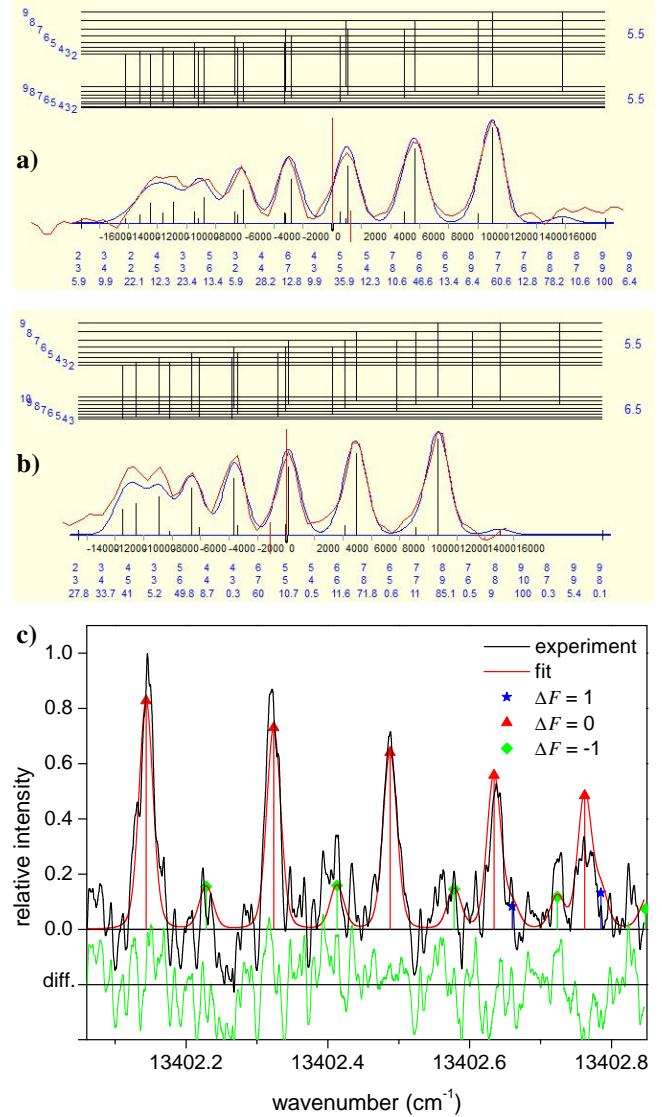


Figure 1. Lines including the new odd-parity upper energy level $E = 39019.06$ cm^{-1} , $J = 11/2$; a) and b) simulation, and c) fit a) FT-line at $\lambda_{\text{air}} = 527.327$ nm to the level $E = 20060.76$ cm^{-1} , $J = 11/2$ b) FT-line at $\lambda_{\text{air}} = 539.653$ nm to the level $E = 20493.77$ cm^{-1} , $J = 13/2$ c) LIF-line at $\lambda_{\text{air}} = 745.920$ nm to the level $E = 25616.48$ cm^{-1} , $J = 11/2$

screen shots from the program ELEMENTS (Windholz 2016). In the upper part of the representation of the simulations the term scheme with the corresponding transitions is drawn. The J -values of the levels are indicated on the right-hand edge of the term scheme, and the F -values of the hfs-sub-levels on the left-hand edge. Below the curve, for each hfs transition the F -quantum number of the upper and lower hfs-sub-levels and the relative intensity of the transitions are listed one above the other. These data are not in scale to the wavelength axis (which is given in MHz), but corresponds to the occurrence of the transitions (from left to right) in the order term scheme. The

same applies to all other figures of simulations of FT spectra (i.e. Figures 2a, 4c, 5, 6, 7a,b and 8a-c).

In the representation of the fit of the LIF spectrum (Figure 1c) the hfs components are marked by the difference ΔF of the F quantum number of the upper and lower hfs levels. In the lower part the figure, the difference (diff.) between experimental and best-fit curve is given. The same applies to the other figure of fit of the LIF spectrum (i.e. Figure 7c).

The hfs of the line measured with LIF and shown in Figure 1c is wider than the section that can be seen in the Figure. This is because the line is wider than the laser scan range. Although since only a section is visible, the structure of the line clearly fits the expected structure of the transition.

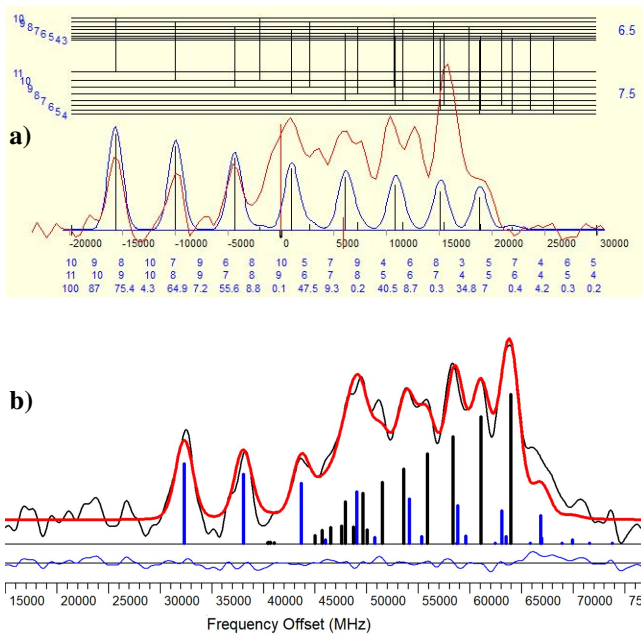


Figure 2. FT-Line including the new odd-parity upper energy level $E = 40438.59 \text{ cm}^{-1}$, $J = 13/2$; at $\lambda_{\text{air}} = 472.421 \text{ nm}$ to the level $E = 19276.94 \text{ cm}^{-1}$, $J = 15/2$
 a) simulation, and b) fit considering the blending line

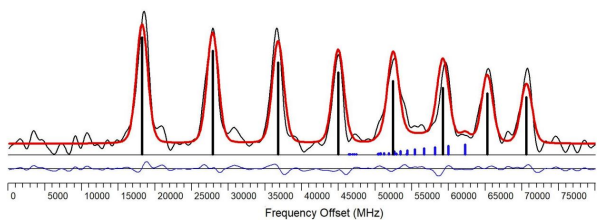


Figure 3. Further line including the new odd-parity upper energy level $E = 40438.59 \text{ cm}^{-1}$, $J = 13/2$; FT-line at $\lambda_{\text{air}} = 557.880 \text{ nm}$ to the level $E = 22518.55 \text{ cm}^{-1}$, $J = 11/2$; fit considering the blending line; line under investigation (blue bars) is only faintly visible under the blending line (black bars)

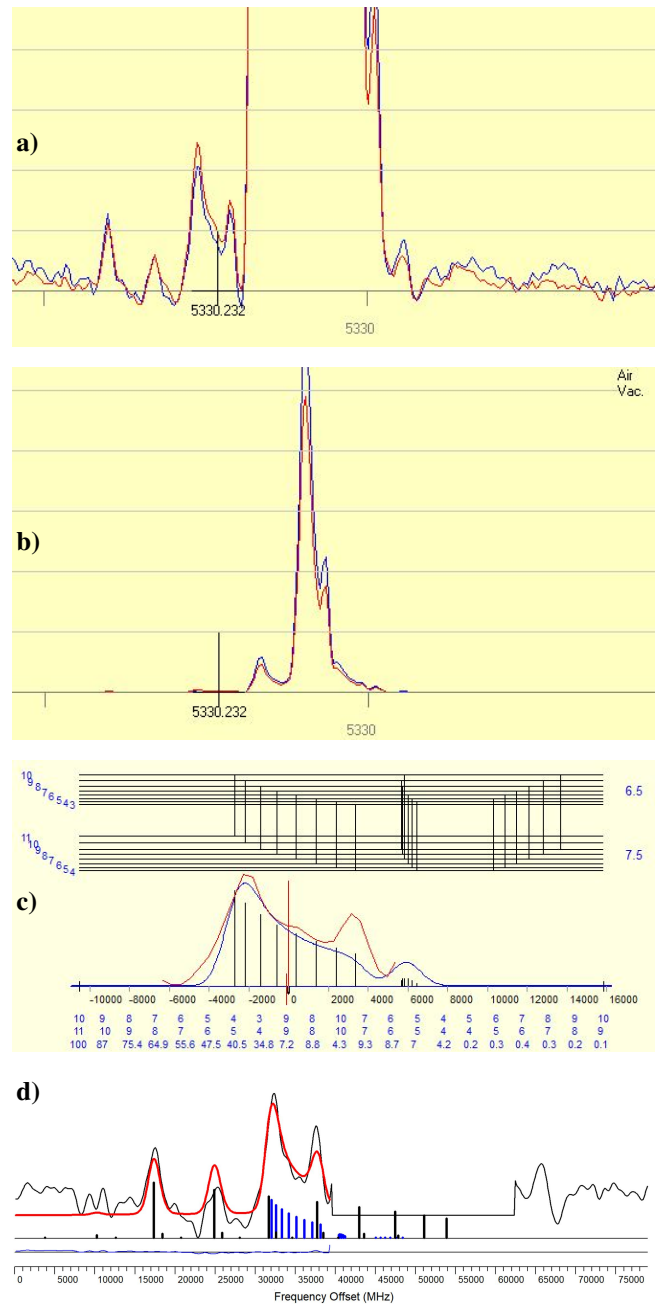


Figure 4. FT-Line including the new odd-parity upper energy level $E = 40438.59 \text{ cm}^{-1}$, $J = 13/2$ at $\lambda_{\text{air}} = 533.023 \text{ nm}$ to the level $E = 21682.90 \text{ cm}^{-1}$, $J = 15/2$; the line under investigation lies on the left edge of a very strong, well-known line. To illustrate this, in a) and b) the same section is shown with different scales on the y-axis. The vertical black bar marks the position (cog) of the line under investigation.

- a) one graduation mark corresponds to S/N of 10
- b) one graduation mark corresponds to S/N of 2560
- c) simulation of a very limited excerpt; only line under investigation
- d) simulation of a slightly wider excerpt, considering the additional weak blending line, whereby the area of the very strong blending line was blanked out

In summary, with these three lines the level 39019.06 cm^{-1} could be clearly confirmed.

Level 40438.59 cm⁻¹

For this level, 15 lines have been examined with LIF and not a single one showed a LIF signal. LIF measurements are not yet a proof that the level does not exist nor that it exists.

Additionally we examined all lines to this level in the FT spectrum. Six lines are listed in Table 2. Two of the lines, given by (Chomski et al. 2023) as transition to the level show a hfs which complete differ from the simulated/expected hfs for the investigated transitions. For two other lines given by (Chomski et al. 2023) and for one additional line not mentioned in (Chomski et al. 2023) there is a matching signal in the FT spectrum, but the lines were blended with other lines.

The first line is shown in Figure 2a and b, in 2a a simulation of only the transition under investigation and in 2b a simulation considering the blending line. In Figure 2b, the components of the different lines are marked with vertical bars of different colours (blue and black). The blending line is known (36954.18 cm⁻¹, $J = 13/2 \rightarrow 15792.13$ cm⁻¹, $J = 11/2$) and the known hfs constants A and B were used for the simulation.

The second line is shown in Figure 3 is weak and blended by a stronger line, which has a broader hfs. Not much could be seen in this case, but it is possible to show in Figure 3, that the disturbance under the strong line could come from the line we are looking for. Here the strong blending line is not classified or unclassifiable, respectively. This means that (at least) one unknown level is involved in the transition. Even without classification, it was possible to achieve an acceptable simulation.

The third line, shown in Figure 4a to d in different representations, lies at the edge of a very strong line, the intensity of which is higher by a factor of more than 500. At the same time the line under investigation is also blended by a second weak but wider splitting line. Figure 4a and b show only the section of the FT spectrum in two different scatterings of the y-axis (without simulation) in order to illustrate the differences in magnitude. The centre of gravity (cog) of the line under investigation is marked by a vertical black bar.

Figure 4c shows only a very small section of the spectrum with a simulation of only the examined line. The match is quite good even though the disturbance of one hfs component of the weak blending line is visible. The weak blending line is known (37623.18 cm⁻¹, $J = 15/2 \rightarrow 18867.54$ cm⁻¹, $J = 13/2$) while the strong blending line could not clearly identified. Figure 4d shows a simulation of the examined line together with the weak blending line. The hfs constants A and B of both levels of both lines were known and used for the simulation. The area of the strong line was blanked out in this simulation.

A further FT line shown in Figure 5 is observed, but it was very weak and unresolved.

All these lines are not very convincing for proof, thus we recommend further verification for this level.

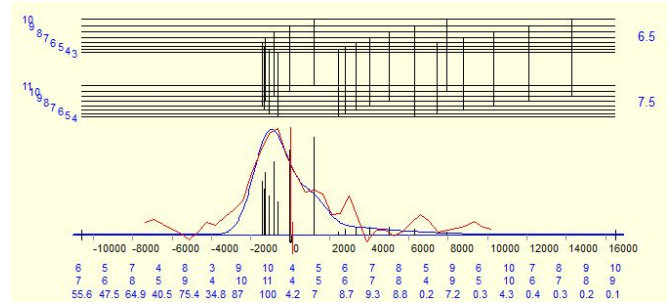


Figure 5. Further lines including the new odd-parity upper energy level $E = 40438.59$ cm⁻¹, $J = 13/2$; FT-line at $\lambda_{\text{air}} = 542.606$ nm to the level $E = 22014.12$ cm⁻¹, $J = 15/2$

Level 42189.40 cm⁻¹

For this level, five lines have been examined with LIF. None of those showed a LIF signal. The only FT line to this levels found is shown in n Figure 6. This line is not very strong and does not own much structure. Nevertheless, the shape quite clearly fits the transition under investigation. This single line studied is among the lines reported in (Chomski et al. 2023). However, this fact is not useful for reliable confirmation, thus, we recommend further verification for this level.

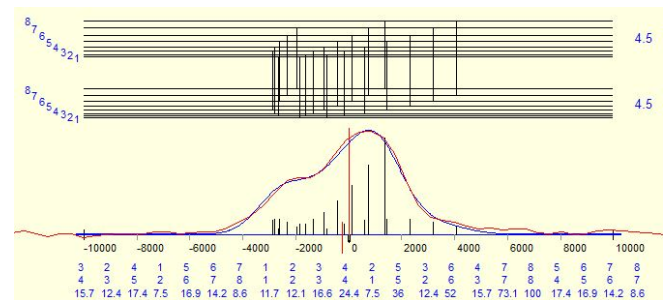


Figure 6. FT-line including the new odd-parity upper energy level $E = 42189.40$ cm⁻¹, $J = 9/2$ at $\lambda_{\text{air}} = 499.074$ nm to the level $E = 22157.88$ cm⁻¹, $J = 9/2$.

Level 36071.92 cm⁻¹

For this level, same as for the first level at 39019.06 cm⁻¹ two FT lines and one LIF line were found, all of which show clear and distinct structures. The lines are shown in Figure 7. The blends on the left side of the line in Figure 7a and on the right side of Figure 7b do not disturb the clearly recognisable structures. With these three lines the level 36071.92 cm⁻¹ could be clearly confirmed.

Level 44283.99 cm⁻¹

For this level, there is no theoretical line available that falls within the wavelength range of our laser. Instead, three FT lines were found (see Figure 8). One of the lines is very weak (Figure 8a), and for the other one the splitting is so small that only one

peak can be seen (Figure 8c). The remaining line showed a clear and distinct structure (Figure 8b). The value can therefore be considered as confirmed, however this single line is one among the lines reported in Chomski et al. (2023). Confirmation by a line that is not mentioned in the reference would have been more satisfactory. Thus, we declare the status of this level as “further investigation recommended.”

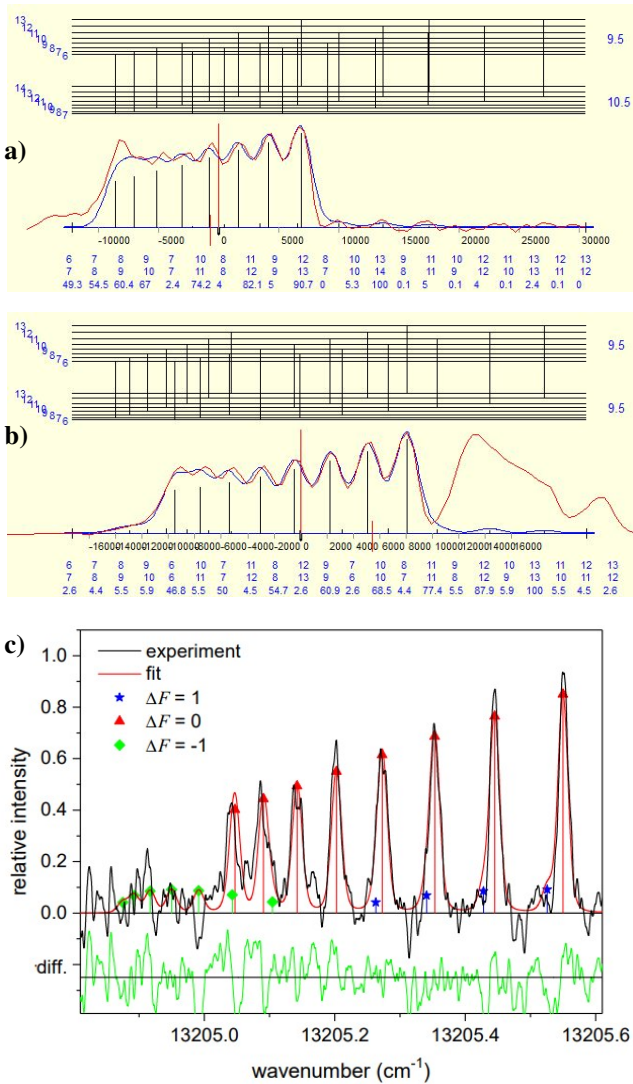


Figure 7. Lines including the new odd-parity upper energy level $E = 36071.92 \text{ cm}^{-1}$, $J = 19/2$; a) and b): simulation, and c): fit
 a) FT-line at $\lambda_{\text{air}} = 403.933 \text{ nm}$ to the level $E = 11322.31 \text{ cm}^{-1}$, $J = 21/2$
 b) FT-line at $\lambda_{\text{air}} = 410.020 \text{ nm}$ to the level $E = 11689.77 \text{ cm}^{-1}$, $J = 19/2$
 c) LIF-line at $\lambda_{\text{air}} = 757.059 \text{ nm}$ to the level $E = 22866.55 \text{ cm}^{-1}$, $J = 19/2$.

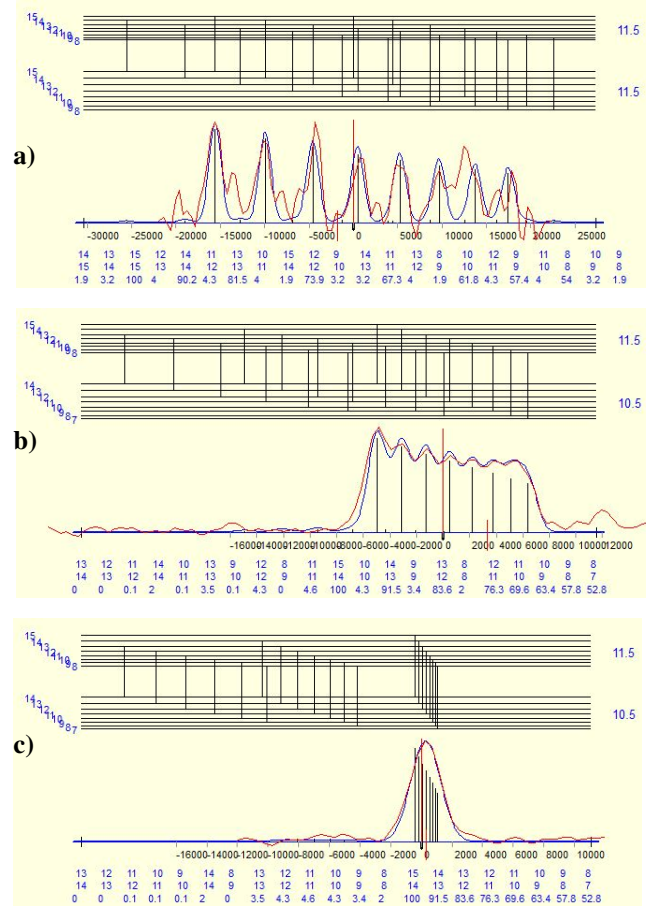


Figure 8. Lines including the new odd-parity upper energy level $E = 44283.99 \text{ cm}^{-1}$, $J = 23/2$ (simulations);
 a) FT-line at $\lambda_{\text{air}} = 448.238 \text{ nm}$ to the level $E = 21980.67 \text{ cm}^{-1}$, $J = 23/2$
 b) FT-line at $\lambda_{\text{air}} = 477.940 \text{ nm}$ to the level $E = 23366.71 \text{ cm}^{-1}$, $J = 21/2$
 c) FT-line at $\lambda_{\text{air}} = 510.853 \text{ nm}$ to the level $E = 24714.34 \text{ cm}^{-1}$, $J = 21/2$

5. FURTHER REMARKS TO THE WORK OF CHOMSKI ET AL.

We have noticed, that several hfs constants A and B of previously known energy levels presented in Chomski et al. (2023) as measured for the first time have been available in previously published studies. For comparison, these values in previous studies and from Chomski et al. (2023) are given in Table 3.

Also, there is a printing error for the J value of the level 20493.40 cm^{-1} : In the text as well as when reporting the results in Table 3 of Chomski et al. (2023) it is given as $J = 9/2$, whereas in Table 2 of the same reference it is given as $J = 11/2$. The value of $J = 11/2$ is correct.

Table 3. Hyperfine structure constants A and B for the known energy levels of atomic Ho investigated in Chomski et al. (2023), along with the values from previously published studies.

Level			A in MHz		B in MHz		Ref.
E in cm^{-1}	J	p	from [1]	from ref.	from [1]	from ref.	
20493.40	11/2 *	e	1019.3 (1.4)	1012.5 (0.7)	277 (70)	641 (28)	[2]
18572.28	15/2	o	805.8 (0.8)	808 (4)	1663 (318)	1990 (180)	[3]
40648.25	17/2	e	663.0 (0.8)	660.5 (1.6)	-761 (151)	-750 (80)	[3]
20210.60	21/2	o	1022.2 (1.3)	1021.8 (1.3)	-663 (95)	-600 (90)	[3]

* Given as $J = 9/2$ in [1].

[1] Chomski et al. (2023), [2] Stefanska et al. (2018c), [3] Özdalgıç et al. (2019c).

6. CONCLUSION

In this study, as a result of examining the five newly found but unconfirmed energy levels by Chomski et al. (2023), two of the examined levels were confirmed beyond doubt. For the other three levels we recommend further verification. The two levels that could be confirmed are those lying below 40000 cm^{-1} .

Peer Review: Externally peer-reviewed.

Author Contribution: Conception/Design of study - Gö. B., S.K.; Data Acquisition - Gü.B., D.B., S.K.B; Data Analysis/Interpretation - Gö. B., I.K.Ö, F.G., D.B.; Drafting Manuscript - Gö. B., S.K.; Critical Revision of Manuscript - I.K.Ö, Gö. B., S.K.B., S.K.; Final Approval and Accountability - S.K., Gö. B.

Conflict of Interest: Authors declared no conflict of interest.

Financial Disclosure: This work has been supported by the Istanbul University Scientific Research Project via Project No. 39701 and 37896.



LIST OF AUTHOR ORCIDS

D. Bingöl	https://orcid.org/0000-0002-1573-319X
Gö. Başar	https://orcid.org/0000-0002-2428-8163
Gü. Başar	https://orcid.org/0000-0002-8133-7590
I. K. Öztürk	https://orcid.org/0000-0002-3664-3388
F. Güzelçimen	https://orcid.org/0000-0001-8453-9975
S. K. Barka	https://orcid.org/0000-0001-5789-1738
S. Kröger	https://orcid.org/0000-0003-4991-9176

REFERENCES

- Al-Labady, N., Özdalgıç, B., Er, A., Güzelçimen, F., Öztürk, I. K., Kröger, S., Kruzins, A., Tamanis, M., Ferber, R., Başar, Gö., 2017, *ApJS*, 228, 16
- Başar, Gö., Al-Labady, N., Özdalgıç, B., Güzelçimen, F., Er, A., Öztürk, I. K., Ak, T., Bilir, S., Tamanis, M., Ferber, R., Kröger, S., 2017, *ApJS*, 228, 17
- Başar, Gö., Başar, Gü., Özdalgıç, B., Öztürk, I.K., Güzelçimen, F., Bingöl, D., Kröger, S., 2020, *JQSRT*, 243, 106809
- Burghardt, B., Buttgenbach, S., Glaeser, N., Harzer, R., Meisel, G., Roski, B., Traber, F., 1982, *ZPhyA*, 307, 193
- Childs, W.J., Cok, D.R., Goodman, L.S., 1983, *JOSA*, 73, 151
- Ciddor, P. E., 1996, *ApOpt*, 35, 1566
- Chomski, M., Furmann, B., Ruczkowski, J., Suski, M., Stefanska, D., 2021, *JQSRT*, 274, 107865
- Chomski, M., Suski, M., Wilman, S., Furmann, B., Ruczkowski, J., Stefanska, D., 2022, *JQSRT*, 279, 108045
- Chomski, M., Furmann, B., Suski, M., Głowacki, P., Stefanska, D., Mieloch S., 2023, *JQSRT*, 297, 108480
- Elantkowska, M., Ruczkowski, J., Sikorski A., Wilman, S., 2019, *JQSRT*, 237, 106642
- Furmann, B., Stefanska, D., Suski, M., Wilman, S., 2018, *JQSRT*, 219, 117
- Goodman, L.S., Schlüpmann, K., 1964, *ZPhy*, 178, 235
- Kröger, S., Wyart, J. F., Luc, P., 1997, *PhyS*, 55, 579
- Kröger, S., Windholz, L., Başar, Gö., 2023, *PARep*, 2023, 1, 32
- Martin, W. C., Zalubas, R., Hagan, L., 1978, *Atomic Energy Levels - The Rare-Earth Elements*, National Bureau of Standards, NSRDS-NBS, 60, 422
- Merzyn, G., Penselin, S., Wolber, G., 1972, *ZPhy*, 252, 412
- Özdalgıç, B., Güzelçimen, F., Öztürk I. K., Kröger, S., Kruzins, A., Tamanis, M., Ferber, R., Başar, Gö., 2019a, *ApJS*, 240, 27
- Özdalgıç, B., Başar, Gö., Güzelçimen, F., Öztürk I. K., Ak, T., Bilir, S., Tamanis, M., Ferber R., Kröger, S., 2019b, *ApJS*, 240, 28
- Özdalgıç, B., Başar, Gö., Kröger, S., 2019c, *ApJS*, 244, 41
- Reddy, M.N., Ahmad, S.A., Rao, G.N., 1992, *JOSAB*, 9, 22
- Snedden, C., Lawler, J. E., Cowan, J. J., et al., 2009, *ApJS*, 182, 80
- Stefanska, D., Furmann, B., 2018a, *JQSRT*, 206, 286
- Stefanska, D., Ruczkowski, J., Elantkowska, M., Furmann, B., 2018b, *JQSRT*, 209, 180
- Stefanska, D., Furmann, B., Głowacki, P., 2018c, *JQSRT*, 213, 159
- Stone, N.J., 2005, *ADNDT*, 90, 75
- Windholz, L., Guthöhrlein G.H., 2003, *PhST*, 105, 55
- Windholz, L., 2016, *PhyS*, 91, 114003
- Wyart, J.F., Camus, P., Verges, J., 1977, *PhyBC*, 92, 377
- Zeiser, A., Kröger, S., Pooyan-Weis, L., Windholz, L., Guthöhrlein, G., 2022, *JQSRT*, 290, 108294

Investigating Single Quantum Anharmonic Oscillator with Perturbation Theory

B. Adalı¹,  and F. Nutku^{2*} 

¹Istanbul University, TEBIP High Performers Program, Council of Higher Education of Türkiye, Vezneciler, 34134, Istanbul, Türkiye

²Istanbul University, Faculty of Science, Department of Physics, Vezneciler, 34134, Istanbul, Türkiye

ABSTRACT

In this article, for pedagogical purposes we have discussed the application of nondegenerate perturbation theory up to the third order to compute energy eigenvalues and wave functions for the quantum anharmonic oscillator. Energy levels of a single quartic oscillator for λ values in range of 0.1-1 are given. Perturbed and non-perturbed wave functions of the levels up to the fourth excited level are compared. Ground, first and second excited energy levels are also calculated by applying finite differences method and, results are compared with the ones obtained via perturbation theory. It is found that perturbation theory gives comparable results only for a small λ parameter and for the ground state. The quartic term in the Hamiltonian of the anharmonic oscillator leads to a more effective confinement of the particle which is deduced from the plots of wavefunctions and probability distributions. Meanwhile, the number of zero crossing nodes of the wavefunctions increases as the energy level increases, which is an expected result for both the harmonic and anharmonic oscillator.

Keywords: anharmonic oscillators; perturbation theory; quantum oscillator

1. INTRODUCTION

The quantum anharmonic oscillator has been analytically studied in the literature by [Bender & Wu \(1969, 1973\)](#). In their articles published in 1969, they examined the anharmonic oscillator defined by the following differential equation,

$$\left(-\frac{d^2}{dx^2} + \frac{1}{4}x^2 + \frac{1}{4}\lambda x^4\right)\phi(x) = E(\lambda)\phi(x). \quad (1)$$

They also investigated the boundary conditions for this oscillator. Using the Wentzel–Kramers–Brillouin (WKB) approximation method, they discovered that there are an infinite number of branch points as a function of λ^α in the limit as λ approaches 0. In an article published in 1973, they further studied the Rayleigh–Schrödinger expansions of energy eigenvalues for high-order perturbations of the anharmonic oscillator.

In a famous classical problem book of quantum mechanics [Flügge \(1999\)](#), cubic ($\lambda_1 x^3$) and quartic ($\lambda_2 x^4$) perturbations are added to the quantum harmonic oscillator's Hamiltonian and energy levels of the anharmonic oscillator are calculated by a perturbation method in first and second-order approximation.

[Turbiner \(1981\)](#) proposed a new iteration procedure for the solution of a Schrödinger equation with arbitrary local potential. With this method, both eigenvalues and eigenfunctions are represented as a convergent series. Potentials x^n ($n = 2, 3, 4$)

type and $m^2 g^2 + g x^4$ in one-dimensional space are considered as examples.

In another article of [Turbiner \(2005\)](#), quantum anharmonic oscillator was given by the following Schrödinger equation

$$-\frac{d^2\psi}{dx^2} + m^2 x^2 \psi + g x^4 \psi = E(m^2, g)\psi, \quad (2)$$

which was solved by logarithmic derivation of the eigenfunction approximation. As a result of his approach, the $y(x)$ function has no singularities at real values of x and shows asymptotic behavior as $\lim_{|x| \rightarrow \infty}$. He defined the simplest interpolation of $y(x)$ between $x = 0$ and $x = \infty$ as

$$y_0 = ax + b\sqrt{g}x|x|. \quad (3)$$

Subsequently, first, second, and third corrections to the energy for different a, b, c, m^2 values, and the first correction to the wave function for $m^2 = -1$ and $g = 2$ were evaluated.

In a further study, [Turbiner & del Valle \(2021\)](#) studied in the framework of perturbation theory with the logarithmic derivation of the wave function for the potential

$$V = x^2 + g^2 x^4. \quad (4)$$

They used Riccati-Bloch equation for perturbation theory in g^2 in x -space and generalized Bloch equation for semiclassical expansion in the power of \hbar for energy in (gx) -space. Then they showed the Riccati-Bloch equation and generalized Bloch

Corresponding Author: F. Nutku E-mail: fnutku@istanbul.edu.tr

Submitted: 02.10.2023 • Revision Requested: 07.10.2023 • Last Revision Received: 16.11.2023 • Accepted: 16.11.2023



This article is licensed under a Creative Commons Attribution-NonCommercial 4.0 International License (CC BY-NC 4.0)

equations yield the same expansion in powers of λ for the energy. The eigenfunctions were expressed in terms of interpolation parameters A, B . These parameters are dependent on the n, p quantum numbers. Variational energy was determined for $n = 0, 1, 2, p = 0, 1$ and $g^2 = 0.1, 1, 10, 20, 100$, with plots of the parameters A and B presented. As summarized above quantum anharmonic oscillator is still an interesting topic and also finds applications in mathematical physics such as in [Gaudreau et al. \(2013, 2015\)](#).

In this study, primarily for pedagogical purposes the energy levels of the quantum anharmonic oscillator and the corresponding wave functions have been obtained using non-degenerate perturbation theory up to the third order.

2. PERTURBATION THEORY

When a system's energy undergoes an external disturbance i.e., when an effect that changes the system's energy is applied, the Hamiltonian of the system changes. For a non-perturbed system, the Hamiltonian of the system satisfies the time-independent Schrödinger equation,

$$H\psi_n = E_n\psi_n. \quad (5)$$

For a perturbed system, the Hamiltonian is written within the framework of perturbation theory as

$$H = H^{(0)} + \lambda H'. \quad (6)$$

Here, the parameter λ is a number between 0 and 1. In this equation, $H^{(0)}$ represents the unperturbed Hamiltonian, and H' represents the perturbation term. In the framework of perturbation theory, the wave function ψ_n and the energies E_n are expanded in powers of λ as follows

$$E_n = E_n^{(0)} + \lambda E_n^{(1)} + \lambda^2 E_n^{(2)} + \lambda^3 E_n^{(3)} + \dots, \quad (7)$$

$$\psi_n = \psi_n^{(0)} + \lambda \psi_n^{(1)} + \lambda^2 \psi_n^{(2)} + \lambda^3 \psi_n^{(3)} + \dots \quad (8)$$

Here, $\psi_n^{(1)}$ represents the first-order correction to the eigenfunction representing n^{th} level and $E_n^{(1)}$ represents the first-order correction to the n^{th} energy eigenvalue. Similar expressions hold for higher-order corrections.

In general, when solving physics problems across various fields, it is often sufficient to compute terms up to the second order in these series, including the second-degree terms.

2.1. Perturbation Terms for Energy

The first-order energy correction is the expectation value of the perturbed term that is calculated by using the unperturbed wave functions.

$$E_n^{(1)} = \langle \psi_n^{(0)} | H' | \psi_n^{(0)} \rangle. \quad (9)$$

The second-order energy correction is calculated as

$$E_n^{(2)} = \sum_{m \neq n} \frac{|\langle \psi_m^{(0)} | H' | \psi_n^{(0)} \rangle|^2}{E_n^{(0)} - E_m^{(0)}}. \quad (10)$$

This formula involves a sum over all states m that is different from the state n . The matrix element $\langle \psi_m^{(0)} | H' | \psi_n^{(0)} \rangle$ is calculated again by using the wave functions of the unperturbed harmonic oscillator. For the third-order energy correction, a more complicated expression is used.

$$E_n^{(3)} = \sum_{k_2 \neq n} \sum_{k_3 \neq n} \frac{\langle \psi_n^{(0)} | H' | \psi_{k_3}^{(0)} \rangle \langle \psi_{k_3}^{(0)} | H' | \psi_{k_2}^{(0)} \rangle \langle \psi_{k_2}^{(0)} | H' | \psi_n^{(0)} \rangle}{(E_n^{(0)} - E_{k_2}^{(0)})(E_n^{(0)} - E_{k_3}^{(0)})} - \langle \psi_n^{(0)} | H' | \psi_n^{(0)} \rangle \sum_{k_3 \neq n} \frac{|\langle \psi_n^{(0)} | H' | \psi_{k_3}^{(0)} \rangle|^2}{(E_n^{(0)} - E_{k_3}^{(0)})^2}. \quad (11)$$

2.2. Perturbation Terms for Wave Function

The first-order wave function correction is given by

$$|\psi_n^{(1)}\rangle = \sum_{k_1 \neq n} \frac{\langle \psi_{k_1}^{(0)} | H' | \psi_n^{(0)} \rangle}{E_n^{(0)} - E_{k_1}^{(0)}} |\psi_{k_1}^{(0)}\rangle. \quad (12)$$

This equation involves a sum over all states k_1 that are different from the state n . The matrix element $\langle \psi_{k_1}^{(0)} | H' | \psi_n^{(0)} \rangle$ is computed using the wave functions of the unperturbed harmonic oscillator. The second and third-order corrections are more complicated as the following¹,

$$|\psi_n^{(2)}\rangle = \sum_{k_1 \neq n} \sum_{k_2 \neq n} \left(\frac{\langle \psi_{k_1}^{(0)} | H' | \psi_{k_2}^{(0)} \rangle \langle \psi_{k_2}^{(0)} | H' | \psi_n^{(0)} \rangle}{(E_n^{(0)} - E_{k_1}^{(0)})(E_n^{(0)} - E_{k_2}^{(0)})} - \frac{\langle \psi_n^{(0)} | H' | \psi_n^{(0)} \rangle \langle \psi_{k_1}^{(0)} | H' | \psi_n^{(0)} \rangle}{(E_n^{(0)} - E_{k_1}^{(0)})^2} \right) |\psi_{k_1}^{(0)}\rangle - \frac{1}{2} \sum_{k_1 \neq n} \frac{\langle \psi_n^{(0)} | H' | \psi_{k_1}^{(0)} \rangle \langle \psi_{k_1}^{(0)} | H' | \psi_n^{(0)} \rangle}{(E_{k_1}^{(0)} - E_n^{(0)})^2} |\psi_n^{(0)}\rangle, \quad (13)$$

¹ [https://en.wikipedia.org/wiki/Perturbation_theory_\(quantum_mechanics\)](https://en.wikipedia.org/wiki/Perturbation_theory_(quantum_mechanics))

$$\begin{aligned}
|\psi_n^{(3)}\rangle = & \sum_{k_1 \neq n} \sum_{k_2 \neq n} \sum_{k_3 \neq n} \left[\right. \\
& - \frac{\langle \psi_{k_1}^{(0)} | H' | \psi_{k_2}^{(0)} \rangle \langle \psi_{k_2}^{(0)} | H' | \psi_{k_3}^{(0)} \rangle \langle \psi_{k_3}^{(0)} | H' | \psi_n^{(0)} \rangle}{(E_{k_1}^{(0)} - E_n^{(0)})(E_n^{(0)} - E_{k_2}^{(0)})(E_n^{(0)} - E_{k_3}^{(0)})} \\
& + \frac{\langle \psi_n^{(0)} | H' | \psi_n^{(0)} \rangle \langle \psi_{k_1}^{(0)} | H' | \psi_{k_2}^{(0)} \rangle \langle \psi_{k_2}^{(0)} | H' | \psi_n^{(0)} \rangle}{(E_{k_1}^{(0)} - E_n^{(0)})(E_n^{(0)} - E_{k_2}^{(0)})} \\
& \left. \left(\frac{1}{E_n^{(0)} - E_{k_1}^{(0)}} + \frac{1}{E_n^{(0)} - E_{k_2}^{(0)}} \right) - \frac{|\langle \psi_n^{(0)} | H' | \psi_n^{(0)} \rangle|^2 \langle \psi_{k_1}^{(0)} | H' | \psi_n^{(0)} \rangle}{(E_{k_1}^{(0)} - E_n^{(0)})^3} \right. \\
& + \frac{|\langle \psi_n^{(0)} | H' | \psi_{k_2}^{(0)} \rangle|^2 \langle \psi_{k_1}^{(0)} | H' | \psi_n^{(0)} \rangle}{(E_{k_1}^{(0)} - E_n^{(0)})(E_n^{(0)} - E_{k_2}^{(0)})} \\
& \left. \left(\frac{1}{E_n^{(0)} - E_{k_1}^{(0)}} + \frac{1}{2(E_n^{(0)} - E_{k_2}^{(0)})} \right) \right] |\psi_{k_1}^{(0)}\rangle + \sum_{k_1 \neq n} \sum_{k_2 \neq n} \left[\right. \\
& - \frac{\langle \psi_n^{(0)} | H' | \psi_{k_2}^{(0)} \rangle \langle \psi_{k_2}^{(0)} | H' | \psi_{k_1}^{(0)} \rangle \langle \psi_{k_1}^{(0)} | H' | \psi_n^{(0)} \rangle}{2(E_n^{(0)} - E_{k_2}^{(0)})^2 (E_n^{(0)} - E_{k_1}^{(0)})} \\
& + \frac{\langle \psi_{k_2}^{(0)} | H' | \psi_n^{(0)} \rangle \langle \psi_{k_1}^{(0)} | H' | \psi_{k_2}^{(0)} \rangle \langle \psi_n^{(0)} | H' | \psi_{k_1}^{(0)} \rangle}{2(E_n^{(0)} - E_{k_2}^{(0)})^2 (E_n^{(0)} - E_{k_1}^{(0)})} \\
& \left. + \frac{|\langle \psi_n^{(0)} | H' | \psi_{k_1}^{(0)} \rangle|^2 \langle \psi_n^{(0)} | H' | \psi_n^{(0)} \rangle}{(E_n^{(0)} - E_{k_1}^{(0)})^3} \right] |\psi_n^{(0)}\rangle. \tag{14}
\end{aligned}$$

3. THE QUANTUM ANHARMONIC OSCILLATOR

In one dimension the Hamiltonian for the quantum anharmonic oscillator is given as

$$H = \frac{p^2}{2m} + \frac{1}{2}m\omega^2 x^2 + \lambda x^4, \tag{15}$$

where H includes an additional term to the quantum harmonic oscillator proportional to x^4 . The energy levels of quantum harmonic oscillator are determined by

$$E_n^{(0)} = \left(n + \frac{1}{2} \right) \hbar\omega, \tag{16}$$

where n is the quantum number, which can take on integer values, including zero. The wave function for the n^{th} state is expressed as

$$\psi_n(x) = A_n a_+^n \psi_0(x), \tag{17}$$

where, A_n is a normalization constant, a_+ is the raising operator and $\psi_0(x)$ is the ground state wave function. In our work, we first calculated perturbation terms by using algebraic methods of the quantum harmonic oscillator. Afterwards, the obtained ket states were replaced with normalized analytical functions of the quantum harmonic oscillator.

In the algebraic formalism of the quantum harmonic oscillator, the following operators are used. Momentum and position

operators, respectively

$$p = \frac{\hbar}{i} \frac{d}{dx}, \quad x = \sqrt{\frac{\hbar}{2m\omega}} (a_+ + a_-), \tag{18}$$

and x^2 operator,

$$x^2 = \frac{\hbar}{2m\omega} [a_+^2 + a_+ a_- + a_- a_+ + a_-^2], \tag{19}$$

also raising (creation) and lowering (annihilation) operators are given as

$$a_+ = \frac{1}{\sqrt{2\hbar m\omega}} (-ip + m\omega x), \tag{20}$$

$$a_- = \frac{1}{\sqrt{2\hbar m\omega}} (+ip + m\omega x). \tag{21}$$

If we apply the raising and lowering operators to the n^{th} ket state, we would obtain the following results.

$$a_+ |n\rangle = \sqrt{n+1} |n+1\rangle, \tag{22}$$

$$a_- |n\rangle = \sqrt{n} |n-1\rangle. \tag{23}$$

For the quantum anharmonic oscillator, the perturbation term depending on the 4th power of x will be written in terms of raising and lowering operators as the following

$$H' = \frac{\hbar^2}{4m^2\omega^2} (a + a^\dagger)^4. \tag{24}$$

3.1. Energy Corrections

The perturbation energy for the anharmonic oscillator is calculated using the perturbation theory formulas presented in Section 2.1. The terms of the series expansion of the n^{th} energy level of the quantum anharmonic oscillator are calculated as follows,

$$E_n^{(1)} = \frac{3\hbar^2 (2n^2 + 2n + 1)}{4m^2\omega^2}, \tag{25}$$

$$E_n^{(2)} = -\frac{\hbar^3 (34n^3 + 51n^2 + 59n + 21)}{8m^4\omega^5}, \tag{26}$$

$$E_n^{(3)} = \frac{3\hbar^4 (125n^4 + 250n^3 + 472n^2 + 347n + 111)}{16m^6\omega^8}. \tag{27}$$

As anticipated, $E_n^{(1)}$, $E_n^{(2)}$, and $E_n^{(3)}$ terms are proportional to \hbar^2 , \hbar^3 and \hbar^4 whereas the unperturbed energy $E_n^{(0)}$ is proportional to \hbar .

The total energy expression is calculated as the series expansion given by Equation 7. Energy values calculated for the ground and first two excited states for λ values ranging from 0.1 to 1 are given in Table 1. When compared to Hioe et al. (1978)'s work, our power series expansion-based perturbation theory calculations only give similar results for small perturbation parameter λ and low-energy states. It might be useful here to compare perturbation theory calculations with numerical results obtained by the finite differences method (FDM) as

Table 1. Energy levels of a single quartic oscillator for various λ values.

λ	Perturbation Method NumPy, SciPy, SymPy			Finite Differences Method Mathematica			Finite Differences Method SciPy, NumPy, finndif		
	E_0	E_1	E_2	E_0	E_1	E_2	E_0	E_1	E_2
0.1	0.5696	1.9134	3.9612	0.5591	1.7694	3.1383	0.5590	1.7688	3.1366
0.2	0.7115	3.3825	11.415	0.6024	1.9504	3.5359	0.6023	1.9497	3.5336
0.3	1.0507	7.3753	32.390	0.6380	2.0945	3.8443	0.6378	2.0936	3.8415
0.4	1.7120	15.360	74.416	0.6687	2.2167	4.1022	0.6686	2.2157	4.0990
0.5	2.8203	28.805	145.02	0.6961	2.3242	4.3268	0.6960	2.3231	4.3232
0.6	4.5005	49.178	251.74	0.7210	2.4208	4.5274	0.7208	2.4195	4.5233
0.7	6.8774	77.947	402.10	0.7439	2.5090	4.7095	0.7437	2.5076	4.7051
0.8	10.076	116.58	603.63	0.7651	2.5904	4.8770	0.7649	2.5890	4.8723
0.9	14.221	166.55	863.86	0.7850	2.6663	5.0326	0.7848	2.6648	5.0275
1.0	19.438	229.31	1190.3	0.8037	2.7376	5.1783	0.8035	2.7359	5.1728

presented in Table 1. In FDM, the second derivative operator $\frac{d^2}{dx^2}$ is replaced with finite differences and expressed as a tridiagonal matrix. Moreover, the potential operator is a diagonal matrix and summation with the tridiagonal matrix leads to the spatial discretization of the Schrödinger equation on a grid. The related mathematica code `xslittlegras`² which calculates energy eigenvalues and corresponding wave functions, is provided in the Supplementary section. FDM gives almost the same results as given in Table 4 in [Hioe et al. \(1978\)](#)'s work. Another implementation of FDM is done by using SciPy, NumPy, and findiff Python libraries `Mathcube`³ and the obtained results are listed in Table 1.

3.2. Wave Function Corrections

Using perturbation theory, the terms of the series expansion of the wave function corresponding to the n^{th} energy level of the quantum anharmonic oscillator were calculated as follows,

$$\begin{aligned}
 |\psi_n^{(1)}\rangle = & \frac{\hbar}{16m^2\omega^3} \left(\left[\sqrt{n(n-3)(n-2)(n-1)} |n-4\rangle \right] \right. \\
 & + \left[(8n-4)\sqrt{n(n-1)} |n-2\rangle \right] \\
 & - \left[(8n+12)\sqrt{n^2+3n+2} |n+2\rangle \right] \\
 & \left. - \left[\sqrt{n^4+10n^3+35n^2+50n+24} |n+4\rangle \right] \right), \quad (28)
 \end{aligned}$$

the second and third-order corrections to wave function $\psi_n^{(2)}$ is computed as mentioned in Section 2.2. Second-order correction

to wave function is found as

$$\begin{aligned}
 |\psi_n^{(2)}\rangle = & \frac{\hbar^2}{256m^4\omega^6} \left(\left(32n^{\frac{5}{2}} - 144n^{\frac{3}{2}} + 112\sqrt{n} \right) \right. \\
 & \left. \sqrt{n-3}\sqrt{n-2}\sqrt{n-1} |n-4\rangle \right. \\
 & + \left(-8n^{\frac{7}{2}} - 516n^{\frac{5}{2}} + 428n^{\frac{3}{2}} - 264\sqrt{n} \right) \sqrt{n-1} |n-2\rangle \\
 & - \left(65n^4 + 130n^3 + 487n^2 + 422n + 156 \right) |n\rangle \\
 & + \left(-8n^3 + 492n^2 + 1436n + 1200 \right) \sqrt{n^2+3n+2} |n+2\rangle \\
 & \left. + \left(32n^2 + 208n + 288 \right) \sqrt{n^4+10n^3+35n^2+50n+24} |n+4\rangle \right), \quad (29)
 \end{aligned}$$

and third-order correction to wave function is found as

$$\begin{aligned}
 |\psi_n^{(3)}\rangle = & \frac{\hbar^3}{512m^6\omega^9} \left(\left(-4n^{\frac{9}{2}} - 406n^{\frac{7}{2}} + 2062n^{\frac{5}{2}} - 2576n^{\frac{3}{2}} \right) \right. \\
 & + 1359\sqrt{n} + 2\hbar^2\omega^2 \left(-17n^{\frac{9}{2}} - 34n^{\frac{7}{2}} - 139n^{\frac{5}{2}} - 122n^{\frac{3}{2}} - 48\sqrt{n} \right) \left. \right) \\
 & \left(\sqrt{n-3}\sqrt{n-2}\sqrt{n-1} \right) |n-4\rangle + \left(30n^{\frac{11}{2}} \right. \\
 & + 325n^{\frac{9}{2}} + 6124n^{\frac{7}{2}} - 5941n^{\frac{5}{2}} + 8582n^{\frac{3}{2}} - 2040\sqrt{n} \\
 & + 2\hbar^2\omega^2 \left(-136n^{\frac{11}{2}} - 204n^{\frac{9}{2}} - 976n^{\frac{7}{2}} - 420n^{\frac{5}{2}} + 104n^{\frac{3}{2}} + 192\sqrt{n} \right) \left. \right) \\
 & \left(\sqrt{n-1} \right) |n-2\rangle + \left(1068n^5 + 2670n^4 + 13776n^3 \right. \\
 & + 17994n^2 + 14748n + 4464 \left. \right) |n\rangle + \left(-30n^5 + 175n^4 - 5124n^3 \right. \\
 & - 22663n^2 - 37686n - 22392 \\
 & + 2\hbar^2\omega^2 \left(136n^5 + 476n^4 + 150n^3 + 2644n^2 + 1848n + 576 \right) \left. \right) \\
 & \left(\sqrt{n^2+3n+2} \right) |n+2\rangle + \left(4n^4 - 390n^3 - 3256n^2 - 7902n \right. \\
 & - 6399 + 2\hbar^2\omega^2 \left(17n^4 + 34n^3 + 139n^2 + 122n + 48 \right) \left. \right) \\
 & \left. \left(\sqrt{n^4+10n^3+35n^2+50n+24} \right) |n+4\rangle \right). \quad (30)
 \end{aligned}$$

² <https://mathematica.stackexchange.com/questions/32293/find-eigen-energies-of-time-independent-schr%C3%B6dinger-equation>

³ <https://medium.com/@mathcube7/two-lines-of-python-to-solve-the-schr%C3%B6dinger-equation-2bcd55c2a0e>

Table 2. Zeros of wave functions for various λ values (only positive x and $x = 0$ points are listed).

λ	ψ_0	ψ_1	ψ_2	ψ_3	ψ_4
0.1	2.275	0, 2.146	0.738, 2.354	0, 1.373, 2.749	0.867, 1.903, 3.243
0.2	1.581	0, 1.805	0.884, 2.226	0, 0.302, 1.432, 2.682	0.101, 0.906, 1.911, 3.179
0.3	1.369	0, 1.753	0.908, 2.208	0, 0.331, 1.430, 2.666	0.101, 0.900, 1.897, 3.150
0.4	1.294	0, 1.739	0.910, 2.201	0, 0.330, 1.425, 2.659	0.095, 0.895, 1.889, 3.136
0.5	1.263	0, 1.733	0.910, 2.198	0, 0.326, 1.422, 2.654	0.090, 0.892, 1.883, 3.128
0.6	1.249	0, 1.730	0.908, 2.195	0, 0.323, 1.419, 2.651	0.086, 0.890, 1.880, 3.122
0.7	1.242	0, 1.728	0.907, 2.193	0, 0.317, 1.417, 2.648	0.081, 0.888, 1.877, 3.199
0.8	1.237	0, 1.727	0.906, 2.192	0, 0.317, 1.416, 2.647	0.079, 0.887, 1.875, 3.116
0.9	1.235	0, 1.726	0.905, 2.191	0, 0.315, 1.415, 2.645	0.076, 0.886, 1.874, 3.114
1.0	1.233	0, 1.725	0.904, 2.190	0, 0.313, 1.414, 2.644	0.074, 0.885, 1.873, 3.112

In each correction term kets are replaced with normalized wave functions of quantum harmonic oscillator. In the following, we presented constituent terms of the wave function for the ground and first excited states where \hbar, m, ω selected as 1. Terms of the ground state wave function are

$$\begin{aligned}\psi_0^{(0)}(x) &= \frac{e^{-\frac{x^2}{2}}}{\sqrt{\pi}}, \\ \psi_0^{(1)}(x) &= \frac{(-4x^4 - 12x^2 + 9) e^{-\frac{x^2}{2}}}{16\sqrt{\pi}}, \\ \psi_0^{(2)}(x) &= \frac{3 \cdot (96x^4 - 88x^2 - 41) e^{-\frac{x^2}{2}}}{64\sqrt{\pi}}, \\ \psi_0^{(3)}(x) &= \frac{3(-8404x^4 + 11052x^2 + 2265) e^{-\frac{x^2}{2}}}{512\sqrt{\pi}},\end{aligned}\quad (31)$$

and terms of the first excited state wave function are

$$\begin{aligned}\psi_1^{(0)}(x) &= \frac{\sqrt{2}x e^{-\frac{x^2}{2}}}{\sqrt{\pi}}, \\ \psi_1^{(1)}(x) &= \frac{\sqrt{2}x(-4x^4 - 20x^2 + 45) e^{-\frac{x^2}{2}}}{16\sqrt{\pi}}, \\ \psi_1^{(2)}(x) &= \frac{3\sqrt{2}x(176x^4 - 360x^2 - 225) e^{-\frac{x^2}{2}}}{64\sqrt{\pi}}, \\ \psi_1^{(3)}(x) &= \frac{3\sqrt{2}x(-22964x^4 + 65940x^2 + 5445) e^{-\frac{x^2}{2}}}{512\sqrt{\pi}}.\end{aligned}\quad (32)$$

The total wave function is calculated by using Equation 8. Care must be taken to ensure that the total wave function obtained by perturbation expansion must be checked for normalization. In this work, for each level n , the wave function is checked and normalized numerically. In Figure 1, total normalized wave functions belonging to quantum anharmonic and harmonic oscillators are presented. As seen from the plots, oscillations in the wave functions of the anharmonic oscillator are not well-periodic. Moreover, one and two additional peaks occur in the wave functions and probability distributions for odd and even parity solutions, respectively.

In Table 2, for the wave functions representing the ground and the first four excited states plotted in Figure 1, the numerical values of the x positions of the nodes are listed for λ values between 0.1 and 1. As expected, odd-numbered states are anti-symmetric, and even-numbered states are symmetric with respect to the origin. Therefore in Table 2, only positive roots and the $x = 0$ point intersections are listed. The number of intersections with the x -axis increases as the quantum state number increases, as expected. More interestingly, with the increase of the λ perturbation parameter, spreading of the peaks of the wave functions along the x -axis decreases.

As an example for the excited state with $n = 10$ and perturbation parameter $\lambda = 0.1$, probability distributions of quantum harmonic and anharmonic oscillators are given in Figure 2. If one compares the two probability distributions, it can be deduced that, due to the quartic term in the Hamiltonian, the localization range of the particle in one dimension decreases in the anharmonic oscillator case compared to the harmonic oscillator.

4. CONCLUSION

In this article we have computed the energy and wave function corrections for the quantum anharmonic oscillator up to the third order by using non-degenerate perturbation theory. Consistent energy values with the literature are found only for small perturbation parameters and low quantum levels. The x^4 term in the Hamiltonian leads to an increase in the intensity of confinement, which facilitates the localization of a particle.

Peer Review: Externally peer-reviewed.

Author Contribution: Conception/Design of study - F.N.; Data Acquisition - F.N., B.A.; Data Analysis/Interpretation - F.N.; Drafting Manuscript - F.N., B.A.; Critical Revision of Manuscript - F.N.; Final Approval and Accountability - F.N., B.A.; Technical or Material Support - F.N.; Supervision F.N.

Conflict of Interest: Authors declared no conflict of interest.

Financial Disclosure: Authors declared no financial support.

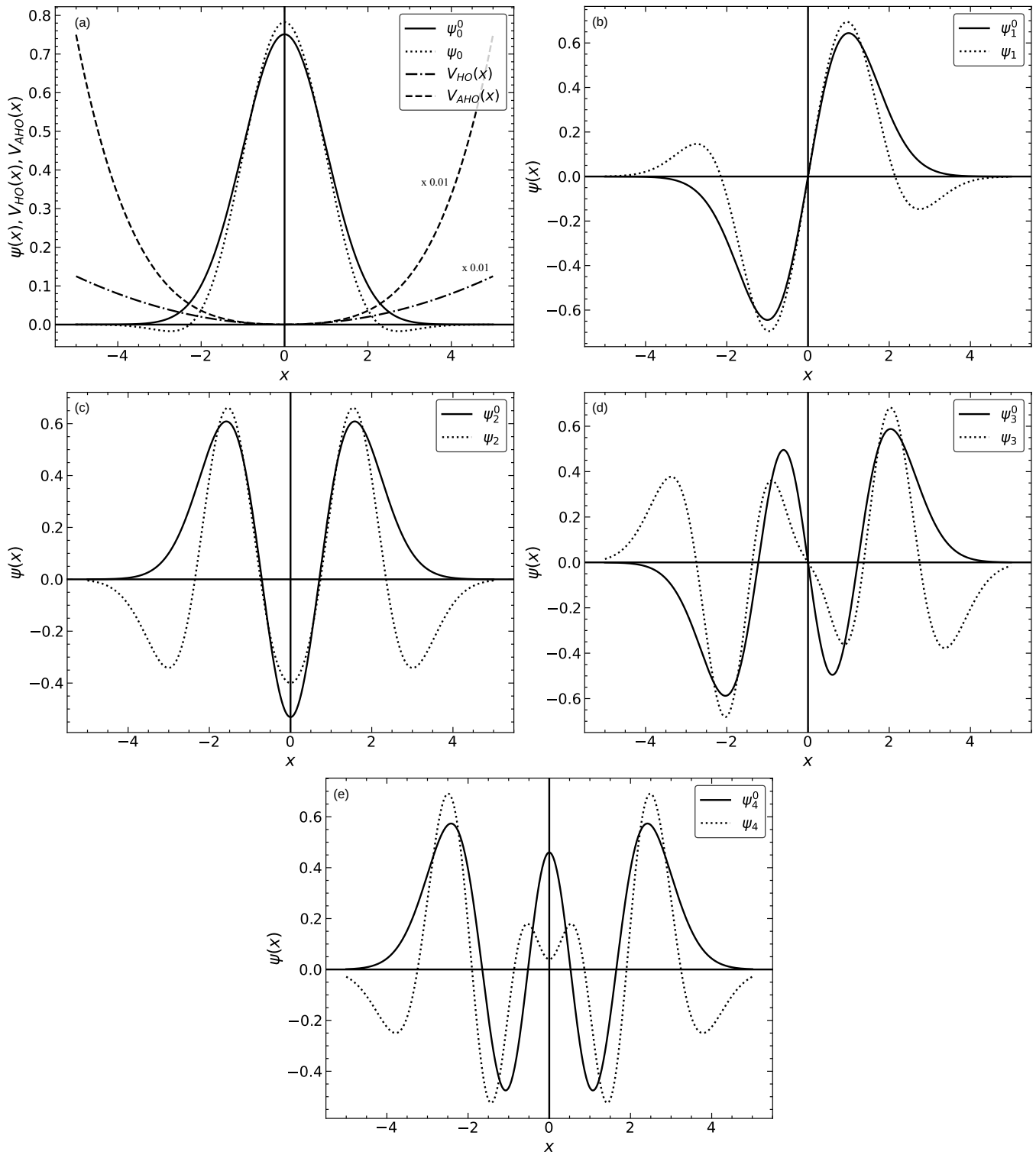


Figure 1. Wave functions of harmonic (solid) and quartic anharmonic (dotted) oscillator with $\lambda = 0.1$. In (a) harmonic and quartic potentials with $\lambda = 0.1$ are also plotted.

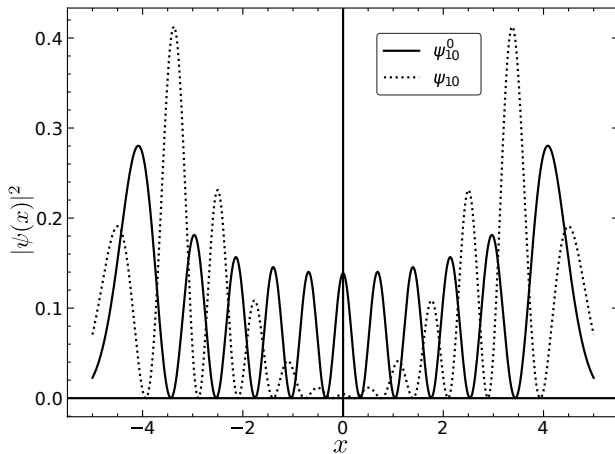


Figure 2. Probability distribution of quantum harmonic (solid) and quartic anharmonic (dotted) oscillator for quantum level $n = 10$ and $\lambda = 0.1$.

Peer Review: Externally peer-reviewed.

Author Contribution: Conception/Design of study - B.A., F.N.; Data Acquisition - B.A., F.N.; Data Analysis/ Interpretation - B.A., F.N.; Drafting Manuscript - B.A., F.N.; Critical Revision of Manuscript - B.A., F.N.; Final Approval and Accountability - B.A., F.N.

Conflict of Interest: Authors declared no conflict of interest.

Financial Disclosure: Authors declared no financial support.

Acknowledgements: The authors would like to appreciate all the developers of the following softwares; Python (Van Rossum & Drake 2009), NumPy (Harris et al. 2020), SciPy (Virtanen et al. 2020), matplotlib (Hunter 2007), findiff (Baer 2018) and Mathematica⁴ which are used in this study.

LIST OF AUTHOR ORCIDS

B. Adalı <https://orcid.org/0000-0002-9526-0168>
F. Nutku <https://orcid.org/0000-0002-2052-4894>

REFERENCES

- Baer M., 2018, findiff Software Package, <https://github.com/maroba/findiff>
- Bender C. M., Wu T. T., 1969, *Physical Review*, 184, 1231
- Bender C. M., Wu T. T., 1973, *Physical Review D*, 7, 1620
- Flügge S., 1999, *One-Body Problems without Spin*. Springer Berlin Heidelberg, Berlin, Heidelberg, pp 25–331, doi:10.1007/978-3-642-61995-3_2
- Gaudreau P., Slevinsky R. M., Safouhi H., 2013, *Annals of Physics*, 337, 261
- Gaudreau P. J., Slevinsky R. M., Safouhi H., 2015, *Annals of Physics*, 360, 520
- Harris C. R., et al., 2020, *Nature*, 585, 357
- Hioe F., Macmillan D., Montroll E., 1978, *Physics Reports*, 43, 305

⁴ <https://www.wolfram.com/mathematica/new-in-13/>

- Hunter J. D., 2007, *Computing in Science & Engineering*, 9, 90
- Turbiner A. V., 1981, *Journal of Physics A: Mathematical and General*, 14, 1641
- Turbiner A. V., 2005, *Letters in Mathematical Physics*, 74, 169
- Turbiner A. V., del Valle J. C., 2021, *Journal of Physics A: Mathematical and Theoretical*, 54, 295204
- Van Rossum G., Drake F. L., 2009, *Python 3 Reference Manual*. CreateSpace, Scotts Valley, CA
- Virtanen P., et al., 2020, *Nature Methods*, 17, 261

SUPPLEMENTARY

Codes that are used in calculating energy eigenvalues for anharmonic quantum oscillator are listed below.

Mathematica

```
ClearAll["Global'*"];
TISE1D[U_Function, {xmin_, xmax_}, NOGrid_ : 101,
  BoundaryCondition_String : "zero" :=
Module[{dx = (xmax - xmin)/(NOGrid -
1), Hmtx, Tmtx, Vmtx},
  Tmtx = -(1/(2 (dx)^2))
  SparseArray[{{i_, i_} -> -2, {i_, j_} /; Abs[i -
j] == 1 -> 1},
    {NOGrid, NOGrid}];
  Vmtx = DiagonalMatrix[U /@ Range[xmin, xmax, dx]];
  Hmtx = Tmtx + Vmtx;
  If[BoundaryCondition == "periodic",
    Hmtx[[1, -1]] = Hmtx[[-1, 1]] = -(1/(2 (dx)^2));];
  Sort[Transpose@Eigensystem[Hmtx],
    (#1[[1]] < #2[[1]]) &]
  TableForm[Table[V1[x_] = 1/2. x^2 + \[Lambda] x^4 ;
    Flatten[{\[Lambda],
      Transpose[
        Round[TISE1D[Function[{x}, V1[x]], {-
10, 10}, 1000], 0.0001]][[
1, 1 ;; 3]]],
    {\[Lambda], 0.1, 1, 0.1}],
    TableHeadings -> {None, {"\[Lambda]",
      "\[SubscriptBox[E], \{0\}\]",
      "\[SubscriptBox[E], \{1\}\]",
      "\[SubscriptBox[E], \{2\}\]",
      "\[SubscriptBox[E], \{3\}\]"}},
    TableAlignments -> Center]
```

Python

```
import numpy as np
from scipy.sparse import diags
from scipy.sparse.linalg import eigs
from findiff import FinDiff
l_E = np.array([])
il=0.1
V = {"V2":lambda x:1/2*x**2,
     "V4":lambda x:1/2*x**2 + il*x**4}["V4"]
for il in np.arange(0.1, 1.1 ,0.1):
    x = np.linspace(-5, 5, 200)
    energies, states = eigs(
        -0.5 * FinDiff(0, x[1]-
x[0], 2).matrix(x.shape) +
        diags(V(x),
            k=3, which='SR')
        energies = np.insert(energies, [0], il)
    l_E = np.append(l_E, energies)
l_E = np.round(l_E.real, 4).reshape((10,4))
print("\t1\t E0\t\t E1\t\t E2\t\t n", l_E)
```


AIMS AND SCOPE

Physics and Astronomy Reports aims to contribute to the scientific knowledge in all areas of physics and astronomy. It is an open-access, peer-reviewed and international journal published semiannually in June and December.

The journal is devoted to publish original research and review articles written in English. Original and high quality research articles, review articles (by invitation only), and high-quality conference proceedings (in special issues by the approval of the editorial board) are welcome. The journal targets international and national communities.

Processing and publication are free of charge with the journal. There is no article processing charges or submission fees for any submitted or accepted articles.

POLICIES

Publication Policy

The journal is committed to upholding the highest standards of publication ethics and pays regard to Principles of Transparency and Best Practice in Scholarly Publishing published by the [Committee on Publication Ethics \(COPE\)](#), the [Directory of Open Access Journals \(DOAJ\)](#), the [Open Access Scholarly Publishers Association \(OASPA\)](#), and the [World Association of Medical Editors \(WAME\)](#) on <https://publicationethics.org/resources/guidelines-new/principles-transparency-and-best-practice-scholarly-publishing>

The subjects covered in the manuscripts submitted to the journal for publication must be in accordance with the aim and scope of the journal. Only those manuscripts approved by every individual author and that were not published before or sent to another journal, are accepted for evaluation.

Changing the name of an author (omission, addition or order) in papers submitted to the Journal requires written permission from all the declared authors.

Plagiarism, duplication, fraudulent authorship/denied authorship, research/data fabrication, salami slicing/salami publication, breaching copyrights, and prevailing conflicts of interest are unethical behaviors. All manuscripts that are not in accordance with accepted ethical standards will be removed from publication. This also includes any possible malpractice discovered after publication.

Plagiarism:

Submitted manuscripts that pass the preliminary control are scanned for plagiarism using iThenticate software. If plagiarism/self-plagiarism is found, the authors will be

informed of it. Editors may resubmit the manuscript for a similarity check at any peer-review or production stage if required. High similarity scores may lead to rejection of the manuscript before and even after acceptance. Depending on the type of article and the percentage of the similarity score taken from each article, the overall similarity score is generally expected to be less than 15 or 20%.

Double Blind Peer-Review:

After the plagiarism check, the eligible ones are evaluated by the editors-in-chief for their originality, methodology, importance of the subject covered and compliance with the journal scope. The editor provides a fair double-blind peer review of the submitted articles and hands over the papers matching the formal rules to at least two national/international referees for evaluation and gives green light for publication upon modification by the authors in accordance with the referees' claims.

Open Access Statement

The journal is open access and all content is freely available without charge to the user or his/her institution. Except for commercial purposes, users are allowed to read, download, copy, print, search, or link to the full text of the articles in this journal without asking prior permission from the publisher or author. This is in accordance with the [BOAI](#) definition of open access.

The open access articles in the journal are licensed under the terms of the Creative Commons Attribution-NonCommercial 4.0 International ([CC BY-NC 4.0](#)) license.

Article Processing Charge

All expenses of the journal are covered by Istanbul University. The processing and publication are free of charge. There are no article processing charges or submission fees for any submitted or accepted articles.

Copyright Notice

Authors publishing with the journal retain the copyright to their work licensed under the Creative Commons Attribution-NonCommercial 4.0 International license (<https://creativecommons.org/licenses/by-nc/4.0/>) and grant the Publisher non-exclusive commercial right to publish the work. CC BY-NC 4.0 license permits unrestricted, non-commercial use, distribution, and reproduction in any medium, provided the original work is properly cited.

Correction, Retraction, Expression of Concern

The editor should consider publishing corrections if minor errors that do not affect the results, interpretations and conclusions of the published paper are detected. The editor should consider retraction if major errors and/or misconduct invalidate results and conclusions are detected.

The editors should consider issuing an expression of concern if there is evidence of research or publication misconduct by the authors; there is evidence that the findings are not reliable and institutions of the authors do not investigate the case or the possible investigation seems to be unfair or nonconclusive.

The [COPE](#) and [ICJME](#) guidelines are considered for correction, retractions or expression of concern.

Archiving Policy

To guarantee that all papers published in the journal are maintained and permanently accessible, articles are stored in Dergipark, which serves as a national archival website and simultaneously permits LOCKSS to collect, preserve, and serve content.

Additionally, the authors are encouraged to self-archive the final PDF version of their articles in open electronic archives, which conform to the standards of the Open Archives Initiative ([https:// www.openarchives.org/](https://www.openarchives.org/)). Authors should provide a link from the deposited version to the URL of IUPress journal website.

ETHICS

PUBLICATION ETHICS AND PUBLICATION MALPRACTICE STATEMENT

Physics and Astronomy Reports is committed to upholding the highest standards of publication ethics and pays regard to Principles of Transparency and Best Practice in Scholarly Publishing published by the [Committee on Publication Ethics \(COPE\)](#), the [Directory of Open Access Journals \(DOAJ\)](#), the [Open Access Scholarly Publishers Association \(OASPA\)](#), and the [World Association of Medical Editors \(WAME\)](#) on <https://publicationethics.org/resources/guidelines-new/principles-transparency-and-best-practice-scholarly-publishing>

All submissions must be original, unpublished (including full text in conference proceedings), and not under the review of any other publication. The authors must ensure that the submitted work is original in nature. They must certify that the manuscript has not already been published or submitted elsewhere, in any language. Applicable copy-

right laws and conventions must be followed. Copyright materials (e.g., tables, figures or extensive quotations) must be reproduced only with appropriate permission and acknowledgement. Any work or words by other authors, contributors, or sources must be appropriately credited and referenced.

Each manuscript is reviewed by at least two referees using a double-blind peer review process. Plagiarism, duplication, fraudulent authorship/ denied authorship, research/data fabrication, salami slicing/salami publication, breaching of copyrights, and prevailing conflicts of interest are unethical behaviors. All manuscripts that are not in accordance with accepted ethical standards will be removed from publication. This also includes any possible malpractice discovered after publication.

Research Ethics

Physics and Astronomy Reports adheres to the highest standards in research ethics and follows the principles of international research ethics as defined below. The authors are responsible for the compliance of the manuscripts with ethical rules.

- Principles of integrity, quality and transparency should be sustained in designing the research, reviewing the design and conducting the research.
- The research team and participants should be fully informed about the aims, methods, possible uses, requirements of the research, and risks of participation in research.
- The confidentiality of the information provided by the research participants and the confidentiality of the respondents should be ensured. The research should be designed to protect the autonomy and dignity of the participants.
- Research participants should voluntarily participate in the research, not under any coercion.
- Any possible harm to the participants must be avoided. Research should be planned in such a way that the participants are not at risk.
- The independence of research must be clear, and any conflicts of interest must be disclosed.
- In experimental studies with human subjects, written informed consent from the participants who decided to participate in the research must be obtained. In the case of children and those under wardship or with confirmed insanity, legal custodian assent must be obtained.

- If the study is to be carried out in any institution or organization, approval must be obtained from that institution or organization.
- In studies with human subjects, it must be noted in the method section of the manuscript that the informed consent of the participants and ethics committee approval from the institution where the study was conducted have been obtained.

Author's Responsibilities

The authors are responsible for ensuring that the article is in accordance with scientific and ethical standards and rules. The authors must ensure that the submitted work is original in nature. They must certify that the manuscript has not already been published or submitted elsewhere, in any language. Applicable copyright laws and conventions must be followed. Copyright materials (e.g., tables, figures or extensive quotations) must be reproduced only with appropriate permission and acknowledgement. Any work or words by other authors, contributors, or sources must be appropriately credited and referenced.

All the authors of the submitted manuscript must have direct scientific and academic contributions to the manuscript. The author(s) of the original research articles is defined as a person who is significantly involved in “conceptualization and design of the study”, “collecting the data”, “analyzing the data”, “writing the manuscript”, “reviewing the manuscript with a critical perspective” and “planning/conducting the study of the manuscript and/or revising it”. Fund raising, data collection and supervision of the research group are not sufficient roles to be accepted as authors. The author(s) must meet all these criteria described above. The order of names in the author list of an article must be a co-decision and must be indicated in the [Copyright Agreement Form](#).

Individuals who do not meet the authorship criteria but have contributed to the study must take place in the acknowledgement section. Individuals providing technical support, general support, material, financial support and assisting in writing are examples to be indicated in the acknowledgement section.

All authors must disclose any issues concerning financial relationships, conflicts of interest, and competing interests that may potentially influence the results of the research or scientific judgment. When an author discovers a significant error or inaccuracy in his/her own published paper, it is the author's obligation to promptly cooperate with the editor-in-chief to provide retractions or corrections of mistakes.

Responsibility for the Editor and Reviewers

The editor-in-chief evaluates manuscripts for their scientific content without regard to ethnic origin, gender, sexual orientation, citizenship, religious beliefs or the authors' political philosophy. He/She provides a fair double-blind peer review of the submitted articles for publication and ensures that all the information related to submitted manuscripts is kept as confidential before publishing.

The editor-in-chief is responsible for the content and overall quality of publications. He/She must publish errata pages or make corrections when needed.

The editor-in-chief does not allow any conflicts of interest between the authors, editors and reviewers. Only he has the full authority to assign a reviewer and is responsible for the final decision to publish the manuscripts in the journal.

The reviewers must have no conflict of interest with respect to the research, authors and/or research funders. Their judgment must be objective.

Reviewers must ensure that all information related to submitted manuscripts is kept confidential and must report to the editor if they are aware of copyright infringement and plagiarism on the author's side.

A reviewer who feels unqualified to review the topic of a manuscript or knows that its prompt review will be impossible should notify the editor and excuse him/herself from the review process.

The editor informs the reviewers that the manuscripts are confidential information and that this is a privileged interaction. The reviewers and editorial board cannot discuss the manuscripts with other people. The anonymity of referees must be ensured. In particular situations, the editor may share a review by one reviewer with other reviewers to clarify a particular point.

PEER REVIEW

Peer Review Policies

Only those manuscripts approved by every individual author and that were not published before or submitted to another journal, are accepted for evaluation.

Submitted manuscripts that pass the preliminary control are scanned for plagiarism using iThenticate software. After the plagiarism check, the eligible ones are evaluated by the editor-in-chief for their originality, methodology, importance of the subject covered, and compliance with the journal scope.

The editor hands over the papers matching the formal rules to at least two national/international referees

for double-blind peer review evaluation and gives green light for publication upon modification by the authors in accordance with the referees' claims.

Responsibility for the Editor and Reviewers

The editor-in-chief evaluates manuscripts for their scientific content without regard to ethnic origin, gender, sexual orientation, citizenship, religious beliefs or the authors' political philosophy. He/She provides a fair double-blind peer review of the submitted articles for publication and ensures that all the information related to submitted manuscripts is kept as confidential before publishing.

The editor-in-chief is responsible for the content and overall quality of publications. He/She must publish errata pages or make corrections when needed. The editor-in-chief does not allow any conflicts of interest between the authors, editors and reviewers. Only he has the full authority to assign a reviewer and is responsible for the final decision to publish the manuscripts in the journal.

The reviewers must have no conflict of interest with respect to the research, authors and/or research funders. Their judgment must be objective.

Reviewers must ensure that all information related to submitted manuscripts is kept confidential and must report to the editor if they are aware of copyright infringement and plagiarism on the author's side.

A reviewer who feels unqualified to review the topic of a manuscript or knows that its prompt review will be impossible should notify the editor and excuse him/herself from the review process.

The editor informs the reviewers that the manuscripts are confidential information and that this is a privileged interaction. The reviewers and editorial board cannot discuss the manuscripts with other people. The anonymity of referees must be ensured. In particular situations, the editor may share a review by one reviewer with other reviewers to clarify a particular point.

Peer Review Process

Only those manuscripts approved by every individual author and that were not published before or submitted to another journal, are accepted for evaluation.

Submitted manuscripts that pass the preliminary control are scanned for plagiarism using iThenticate software. After the plagiarism check, the eligible ones are evaluated by the editor-in-chief for their originality, methodology, importance of the subject covered and compliance with the journal scope. Editor-in-chief evaluates manuscripts for their scientific content without regard to ethnic origin,

gender, sexual orientation, citizenship, religious belief or political philosophy of the authors and ensures a fair double-blind peer review of the selected manuscripts.

The selected manuscripts are sent to at least two national/international referees for evaluation, and publication decision is made by the editor-in-chief upon modification by the authors in accordance with the referees' claims.

Editor-in-chief does not allow any conflicts of interest between the authors, editors, and reviewers and is responsible for the final decision for publication of the manuscript in the journal.

The reviewers' judgments must be objective. Reviewers' comments on the following aspects are expected during the review.

- Does the manuscript contain new and significant information?
- Does the abstract clearly and accurately describe the content of the manuscript?
- Is this problem significant and concisely stated?
- Are the methods comprehensively described?
- Are the interpretations and conclusions justified by the results?
- Is adequate reference made to other works in the field?
- Is the language acceptable?

Reviewers must ensure that all information related to submitted manuscripts is kept confidential and must report to the editor if they are aware of copyright infringement and plagiarism on the author's side.

A reviewer who feels unqualified to review the topic of a manuscript or knows that its prompt review will be impossible should notify the editor and excuse him/herself from the review process.

The editor informs the reviewers that the manuscripts are confidential information, and that this is a privileged interaction. The reviewers and editorial board cannot discuss the manuscripts with other people. The anonymity of the referees is important.

AUTHOR GUIDELINES

Manuscript Organization and Submission

1. The publication language of the journal is English
2. Authors are required to submit Copyright Agreement Form, Author Form and Title Page together with the main manuscript document

3. Manuscripts should be prepared using the article template in Latex format
4. Due to double-blind peer review, the main manuscript document must not include any author information.
5. Title page should be submitted together with the main manuscript document and should include the information below:
 - Category of the manuscript
 - The title of the manuscript.
 - All authors' names and affiliations (institution, faculty/department, city, country), e-mail addresses, and ORCIDs.
 - Information of the corresponding author (in addition to the author's information e-mail address, open correspondence address, and mobile phone number).
 - Financial support
 - Conflict of interest.
 - Acknowledgment.
6. Submitted manuscripts should have an abstract of 150-250 words before the introduction, summarizing the scope, the purpose, the results of the study, and the methodology used. Under the abstract, a minimum of 3 and a maximum of 6 keywords that inform the reader about the content of the study should be specified.
7. The manuscripts should contain mainly these components: title, abstract and keywords; sections, references, tables and figures. The main text of research articles should include introduction, methods, results, discussion, conclusion and references subheadings.
8. Tables and figures should be given with a number and a caption. Every Figure or Table should be referred within the text of the article in numerical order with no abbreviations (ie: Table 1, Figure 1)
9. References should be prepared in line with Harvard reference system. For information: <https://www.easybib.com/guides/citation-guides/harvard-referencing/>
10. Authors are responsible for all statements made in their work submitted to the journal for publication.

References

Physics and Astronomy Reports complies with Harvard system for referencing and in-text citations. For information: <https://www.easybib.com/guides/citation-guides/harvard-referencing/>. Accuracy of citations is the author's responsibility. All references should be cited in the text.

It is strongly recommended that authors use Reference Management Software such as Zotero, Mendeley, etc.

Submission Checklist

Please ensure the following:

- The title page was prepared according to the journal rules.
- This manuscript has not been submitted to any other journal.
- The manuscript has been checked for English language.
- The manuscript was written in accordance with the full-text writing rules determined by the journal.
- The manuscript has an abstract of 150-250 words and the number of keywords should be 3-6.
- The references are in line with the Harvard reference system.
- The Copyright Agreement Form has been filled in and is ready for submission together with the manuscript.
- The Author Contribution Form has been filled in and is ready for submission together with the manuscript.
- Permission for previously published copyrighted material (text,figure,table) has been obtained if used in the present manuscript.
- The Ethics Committee Report (if necessary) has been obtained and ready for submission together with the manuscript, and the ethics committee report date and number have been given in the manuscript text.
- Review of the journal policies.
- All authors have read and approved the final version of the manuscript.

EK 2-B

 Istanbul University
 İstanbul Üniversitesi

Journal name: Physics and Astronomy Reports
 Dergi Adı: Physics and Astronomy Reports

Copyright Agreement Form
 Telif Hakkı Anlaşması Formu

Responsible/Corresponding Author Sorumlu Yazar				
Title of Manuscript Makalenin Başlığı				
Acceptance Date Kabul Tarihi				
List of Authors Yazarların Listesi				
Sıra No	Name - Surname Adı-Soyadı	E-mail E-Posta	Signature İmza	Date Tarih
1				
2				
3				
4				
5				

Manuscript Type (Research Article, Review, etc.) Makalenin türü (Araştırma makalesi, Derleme, v.b.)				
Responsible/Corresponding Author: Sorumlu Yazar:				
University/company/institution	<i>Çalıştığı kurum</i>			
Address	<i>Posta adresi</i>			
E-mail	<i>E-posta</i>			
Phone; mobile phone	<i>Telefon no; GSM no</i>			

The author(s) agrees that:

The manuscript submitted is his/her/their own original work, and has not been plagiarized from any prior work, all authors participated in the work in a substantive way, and are prepared to take public responsibility for the work, all authors have seen and approved the manuscript as submitted, the manuscript has not been published and is not being submitted or considered for publication elsewhere, the text, illustrations, and any other materials included in the manuscript do not infringe upon any existing copyright or other rights of anyone. İSTANBUL UNIVERSITY will publish the content under Creative Commons Attribution-NonCommercial 4.0 International (CC BY-NC 4.0) license that gives permission to copy and redistribute the material in any medium or format other than commercial purposes as well as remix, transform and build upon the material by providing appropriate credit to the original work. The Contributor(s) or, if applicable the Contributor's Employer, retain(s) all proprietary rights in addition to copyright, patent rights. I/We indemnify İSTANBUL UNIVERSITY and the Editors of the Journals, and hold them harmless from any loss, expense or damage occasioned by a claim or suit by a third party for copyright infringement, or any suit arising out of any breach of the foregoing warranties as a result of publication of my/our article. I/We also warrant that the article contains no libelous or unlawful statements, and does not contain material or instructions that might cause harm or injury. This Copyright Agreement Form must be signed/ratified by all authors. Separate copies of the form (completed in full) may be submitted by authors located at different institutions; however, all signatures must be original and authenticated.

Yazar(lar) aşağıdaki hususları kabul eder:

Sunulan makalenin yazar(lar)ın orijinal çalışması olduğunu ve intihal yapmadıklarını, Tüm yazarların bu çalışmaya aslı olarak katılmış olduklarını ve bu çalışma için her türlü sorumluluğu aldıklarını, Tüm yazarların sunulan makalenin son halini gördüklerini ve onayladıklarını, Makalenin başka bir yerde basılmadığını veya basılmak için sunulmadığını, Makalede bulunan metnin, şekillerin ve dokümanların diğer şahıslara ait olan Telif Haklarını ihlal etmediğini kabul ve taahhüt ederler. İSTANBUL ÜNİVERSİTESİ'nin bu fikri eseri, Creative Commons Atıf-GayrıTicari 4.0 Uluslararası (CC BY-NC 4.0) lisansı ile yayınlamasına izin verirler. Creative Commons Atıf-GayrıTicari 4.0 Uluslararası (CC BY-NC 4.0) lisansı, eserin ticari kullanım dışında her boyut ve formatta paylaşılmasına, kopyalanmasına, çoğaltılmasına ve orijinal esere uygun şekilde atıfta bulunmak kaydıyla yeniden düzenleme, dönüştürme ve eserin üzerine inşa etme dâhil adapte edilmesine izin verir. Yazar(lar)ın veya varsa yazar(lar)ın işverenin telif dâhil patent hakları, fikri mülkiyet hakları saklıdır. Ben/Biz, telif hakkı ihlali nedeniyle üçüncü şahıslarca vuku bulacak hak talebi veya açılacak davalarda İSTANBUL ÜNİVERSİTESİ ve Dergi Editörlerinin hiçbir sorumluluğunun olmadığını, tüm sorumluluğun yazarlara ait olduğunu taahhüt ederim/ederiz. Ayrıca Ben/Biz makalede hiçbir suç unsuru veya kanuna aykırı ifade bulunmadığını, araştırma yapılırken kanuna aykırı herhangi bir malzeme ve yöntem kullanılmadığını taahhüt ederim/ederiz. Bu Telif Hakkı Anlaşması Formu tüm yazarlar tarafından imzalanmalıdır/onaylanmalıdır. Form farklı kurumlarda bulunan yazarlar tarafından ayrı kopyalar halinde doldurularak sunulabilir. Ancak, tüm imzaların orijinal veya kanıtlanabilir şekilde onaylı olması gerekir.

Responsible/Corresponding Author; Sorumlu Yazar;	Signature / İmza	Date / Tarih
	/...../.....